LABEL-FREE NANOSCALE BIOSENSING USING A POROUS SILICON WAVEGUIDE

By

Guoguang Rong

Dissertation
Submitted to the Faculty of the
Graduate School of Vanderbilt University
in partial fulfillment of the requirements
for the degree of
DOCTOR OF PHILOSOPHY
in
Electrical Engineering
December, 2008
Nashville, Tennessee
Approved:
Professor Sharon M. Weiss
Professor Bharat L. Bhuva
Professor Weng Poo Kang
Professor Raymond L. Mernaugh
Professor Robert A. Weller

To my family

ACKNOWLEDGEMENTS

This work would not have been possible without the financial support of the National Science Foundation, the financial and technical support of Vanderbilt Institute of Nanoscale Science and Engineering, the opportunities to conduct part of the research at Center for Nanophase Materials Sciences of Oak Ridge National Laboratory.

I am grateful to all of those with whom I have had the pleasure to work during this project. Each member of my dissertation committee provided professional comments and guidance on this scientific research. I would especially express my gratitude to my academic advisor, Dr. Sharon M. Weiss, for her patience, encouragement, and criticism throughout my Ph.D. study. She showed me the qualities a good scientist should possess and the value of basic scientific research. I would also thank Dr. Raymond L. Mernaugh of the Department of Biochemistry for his scientific insights and pertinent suggestions on some of the experiments. He demonstrated the confidence and persistence that an experimentalist should have. I really appreciate the pleasant cooperation with Dr. John E. Sipe of the University of Toronto and his post-docs Drs. Ali Najmaie and Marco Liscidini. Without their theoretical work, the research would not be possible. I would also like to acknowledge Dr. Paul E. Laibinis of the Department of Chemical Engineering for the helpful technical discussions. I thank Mr. John Jackson of Metricon, Corp. for helping me with the prism coupler usage and maintenance.

I have had the pleasure to work with many post-docs, graduate students and undergraduate students at Vanderbilt University in the past 4 years, including Dr. Hai Huang of Chemistry, Zhou Xu of Chemical Engineering, and members of the Weiss Group: Xing Wei, Chris Kang, Jenifer L. Lawrie, Yang Jiao, and Judson Ryckman. Some of the valuable time I spent at Vanderbilt was working with undergraduate students from whom I learned a lot. They are Nicolas Bouchonville, Joe Zadrozny, and Talbot Hansum.

Last, I would like to thank my wife for her understanding, endless love and encouragement. Her support and help was in the end to make this dissertation possible. My parents receive my deepest gratitude and love for education and support ever since I was born.

TABLE OF CONTENTS

Page

DEDICATION…………………………………………………………………..….ii

ACKNOWLEDGEMENTS………………………………………………………iii

LIST OF TABLES………………………………………………………...…...…viii

LIST OF FIGURES……………………………………………………..……ix

Chapter

I. INTRODUCTION TO BIOSENSING……………………………………………1

1.1 Definition and classification of biosensors……………………………………………1
1.2 Labeled and label-free biosensors……………………………………...…….3
1.3 Evanescent wave biosensors…………………………………………………….4
1.4 Porous materials based biosensors…………………………………………………8
1.5 Objective and overview of the dissertation ……..10

II. POROUS SILICON WAVEGUIDE STRUCTURE………………………………12

2.1 Porous silicon background and characterization……………………..................12
    2.1.1 Pore formation……………………………..12
    2.1.2 Porosity characterization……………………………………………......13
    2.1.3 Etching speed characterization…………………………………………16
    2.1.4 Porous silicon biosensing…………………………………………….…17
2.2 Porous silicon waveguide design, optimization and fabrication……………………..23
2.3 Revised porous silicon waveguide with larger pores………………………………...34

III. CHEMICAL AND BIOLOGICAL SENSING WITH P-TYPE POROUS SILICON WAVEGUIDE………………………………….................................37

3.1 Sensing of liquids of variable refractive index………………………………………37
3.2 Field profile and biosensing: comparison with SPR…………………………………38
3.3 Sensing of DNA hybridization………………………………………………….……46
    3.3.1 Introduction to DNA………………………………………………………46
    3.3.2 DNA hybridization detection experiments…………………………..........48
    3.3.3 Analysis of the experimental results………………………………………56

3.4 Alternative functionalization biochemistry……………………………………..……60
    3.4.1 Functionalization with sulfo-SMCC……………………………………..60
    3.4.2 Probe DNA attachment..…………………………………………………63
3.5 Choosing the cross-linker: glutaraldehyde vs. sulfo-SMCC………………………64
    3.5.1 Glutaraldehyde (homo-bifunctional)……………………………………64
    3.5.2 Sulfo-SMCC (hetero-bifunctional)……………………………...........65

IV. POROUS SILICON FREE-STANDING MEMBRANE WAVEGUIDE……….67

4.1 Motivation and design……………………………………………………………..67
4.2 Structure and operation of the n-type porous silicon membrane waveguide……..69
4.3 Fabrication……………………………………………………………………...........70
4.4 Characterization………………………………………………………...........71
4.5 DNA sensing…………………………………………………………………………73
    4.5.1 Functionalization……………………………………………………………73
    4.5.2 24-base DNA detection……………………………………………………75
    4.5.3 40-base DNA detection……………………………………………………79

V. BIOMOLECULAR SIZE DEPENDENT SENSITIVITY………………………..80

5.1 Introduction to size dependent sensitivity……………………….……………..80
5.2 Simulation of resonance shifts for variable length of probe DNA……………......82
5.3 Experimental resonance shifts for variable length of probe DNA……………..……83
5.4 Discussion……………………………………………………………………………86

VI. CONCLUSION AND FUTURE RESEARCH……………………………………88

6.1 Conclusion and research contribution……………………………………………..88
6.2 Future research opportunities…………………………………………………89
    6.2.1 New design for porous silicon waveguide sensor……………...…………..89
        6.2.1.1 Porous silicon membrane sensor chip……………………………89
        6.2.1.2 Metal-cladded porous silicon waveguide………………………...90
        6.2.1.3 Porous silicon waveguide with grating coupler…………………90
        6.2.1.4 Porous silicon slot waveguide……………………………………92
        6.2.1.5 Porous silicon waveguide interferometer sensor………………...93
    6.2.2 Detection of a variety of biological molecules ……………………….95
    6.2.3 Sensor array………….……….………………………………...….…..…..95
6.3 Prospect of biosensor research…………….…………………………………96

Appendix……………………………………………………………………………...98

A. POROUS SILICON FABRICATION PROCEDURE.………….……….…………98

B. OPTIMAL CLADDING THICKNESS CALUCULATION CODE.………………101

C. PRISM COUPLER MEASUREMENT PROCEDURE……………………………103

D. WAVEGUIDE REFLECTANCE VS. ANGLE CALCULATION CODE…………106

E. WAVEGUIDE MODE FIELD CALUCULATION CODE…………….…………..110

F. SPR MODE FIELD CALUCULATION CODE……………………………………115

G. INCUBATION PROCEDURE…………………………………………...………118

REFERENCES………………………………………………………….........120

LIST OF TABLES

Table **Page**

2.1. Porous silicon waveguide (method 1) design parameters and fabrication conditions ……………………………………………………………………...……...……..32

2.2. Revised porous silicon waveguide (method 2) fabrication conditions……….……..35

2.3. Effective refractive index of porous silicon waveguide after KOH soaking………..35

3.1. Different fluids and their refractive indices……..…………………………..........37

3.2. Porous silicon (PSi) waveguide and SPR sensors comparison upon exposure to Biomolecules (n=1.46)…………………………………………………………....44

5.1. Fully extended DNA length for different numbers of bases………………………...83

LIST OF FIGURES

Figure **Page**

1.1. Typical structure of a biosensor, from top to bottom: target analyte binds to the probe molecules in the bioreceptor, causing a signal to be transduced. The signal is then measured quantitatively, and the information about the target (e.g. concentration, affinity, kinetic constants) can be deduced………………………..2

1.2. Classification of biosensors by type of bioreceptor or transducer………………...2

1.3. Schematic of labeled biosensor. After bioconjugation with fluorophores, target biomolecules bind to probe biomolecules (either immobilized or in solution). When excited by light of higher energy, the fluorophores emit light at a wavelength that is characteristic to the fluorophore. This fluorescence is detected, confirming the presence of the target molecules. Note that the excitation light is typically filtered out of the signal sent to the photodetector……………………4

1.4. Surface plasmon resonance (SPR) biosensor structure, sensing mechanism and typical attenuated total reflectance (ATR) spectrum. The dashed lines show the electrical field profile of the surface plasmon mode existing between the metal (gold) and the dielectric (air) layers. The resonance in the ATR spectrum corresponds to the angle at which the surface plasmon mode is excited. Biomolecular binding increases the refractive index in the vicinity of the metal surface and induces a change in the angle at which the surface plasmon mode is excited.……………………………………..………..………………6

1.5. Schematic of planar waveguide or fiber optic (with part of the top cladding stripped) biosensor. Biomolecular binding events change the refractive index in the vicinity of the waveguide core surface. This refractive index change is detected as a change in the propagating wave phase or intensity, or as a change of the angle or wavelength of light coupled into the waveguide……………………7

1.6. Porous material added on top of an SPR sensor enhances the surface area. More biomolecules can be immobilized and the sensitivity for small molecule detection is improved.………………………...…………………………………………..9

2.1. (a) Porous silicon porosity that results from the application of different current densities during electrochemical etching. (b) Bruggeman effective refractive index at different porous silicon porosities, assuming a wavelength of 1550 nm………………………………………………………………..15

2.2. Etching rate of porous silicon at different applied current densities……………17

2.3. Single layer porous silicon interferometer and its simulated reflection fringes…18

2.4. Porous silicon multilayer Bragg reflector and its simulated reflectance spectrum……………………………………………………………………….19

2.5. Porous silicon microcavity and its simulated reflectance spectrum……………..21

2.6. Porous silicon waveguide and its qualitative field profile………………………23

2.7. Porous silicon waveguide in the Kretschmann configuration, with a typical attenuated total reflectance spectrum shown in the inset………………………...24

2.8. Measured transmission through various thickness silicon substrates at 1550 nm using FTIR. The 500 μm and 300 μm samples were polished from the wafer vendor. The 200 μm and 100 μm samples were thinned by creating a sacrificial porous silicon layer that was subsequently dissolved by exposure to sodium hydroxide……………………………………………………………...27

2.9. Schematic of porous silicon waveguide biosensor in the Otto configuration, consisting of a low porosity (high refractive index) porous silicon layer, a high porosity (low refractive index) porous silicon layer, and air gap. Total internal reflection enables waveguiding in the low porosity porous silicon layer. A prism is used to couple light at a specific angle α into the waveguide mode through an evanescent wave. The attenuated total reflectance spectrum is similar to the one shown in Figure 2.7…………………………………………………………....28

2.10. Effect of adjusting coupling pressure between the prism and porous silicon waveguide on waveguide resonance quality. The greater the applied pressure, the smaller the air gap between the prism and porous silicon waveguide. The best resonance quality is obtained at 24 psi………………………………………..30

2.11. Optimization of porous silicon waveguiding layer thickness to achieve narrow waveguide resonance using (a) 633 nm and (b) 1550 nm light. The porous silicon is as-anodized………………………………………………………………….31

2.12. Cross-sectional SEM of porous silicon waveguide, showing the top low porosity layer of 300 nm and the bottom high porosity layer of 1330 nm………………..33

2.13. Experimental (a) and theoretical (b) attenuated total reflectance spectra, showing a waveguide mode near 53˚ and a substrate mode near 37˚……………………..34

2.14. Reflectance spectrum of anodized porous silicon waveguide under revised condition in Table 2.2 (solid line) and after the anodized waveguide was exposed to 1.5 mM KOH for 30 minutes (dotted line). The one sharp-and-deep resonance is the guided mode, and the shallower and wider features are the substrate modes……………………………………………………………………………36

3.1. Porous silicon waveguide resonance shift upon exposure to water, acetone, and various mixtures of acetone and Cargille Labs refractive index matching fluid. A linear fit to the data is shown……………………………………………………….38

3.2. Schematic of sensor structure. (a) Porous silicon waveguide biosensor, consisting of a low porosity (high index) layer, a high porosity (low index) layer, and air gap. Total internal reflection enables waveguiding in the low porosity porous silicon layer. A prism is used to couple light into the waveguide mode through an evanescent wave. Biomolecules are infiltrated into the pores of the waveguide. (b) SPR biosensor consisting of a thin gold film on top of a prism. A surface plasmon is launched through an evanescent wave. Biomolecules are immobilized on top of the gold film……………………………………………………………………...39

3.3. (a) E-field distribution for porous silicon waveguide. The waveguide region is between x = -300 nm and x = 0 nm as delimited by the two vertical bars. Above x = 0 is air; below x = -300 nm is the high porosity cladding layer. The shaded area is the power confined in the waveguiding layer where biomolecules are immobilized. (b) E-field distribution for SPR sensor. The gold film is between x = -40 nm and x = 0. Above x = 0 is air; below x = -40 nm is the prism. The vertical bars delimit the region where a 4 nm layer of biomolecules is immobilized. The shaded area is the power interacting with the biomolecules on the gold. Note that 1 watt of total power is assumed for both (a) and (b), and the x-axis scale for (a) is 4x larger than for (b)……………………………………..41

3.4. Resonance shift for (a) porous silicon waveguide and (b) SPR sensor at 1550 nm when exposed to biomolecules (n = 1.46) of different lengths and packing densities. Larger biomolecules that are packed tighter together will induce the largest refractive index change and largest resonance shift. Also shown is the performance enhancement (Shift/FWHM ratio) for the porous silicon waveguide sensor over the SPR sensor considering either (c) all of the porous silicon waveguide surface area is utilized or (d) the same amount of biomolecules are infiltrated into both the porous silicon waveguide and SPR sensors……………45

3.5. (a) Double stranded DNA formed by specific binding. (b) Two non-complementary DNA single strands will not bind together……………………...47

3.6. Step-by-step reaction of cross-linking probe DNA to porous silicon by glutaraldehyde. The oxidized porous silicon sample was first silanized with 3-APTES. The amine derivatized sample was then cross-linked to amine modified probe DNA with glutaraldehyde, generating unstable intermediate Schiff base (C=N). The Schiff base can be stabilized by sodium cyanoborohydride………..49

3.7. Porous silicon waveguide (method 1) resonance shift due to exposure to 100 μL of different concentrations of 3-APTES coating the oxidized pore walls. Near 4% APTES, the shift saturates, suggesting monolayer coating……………………...51

3.8. Porous silicon waveguide resonance after each functionalization step: after oxidation (Oxidized), after 3-APTES (Silanized), and after glutaraldehyde+probe DNA+ethanolamine (GA+Probe+EA)……………………………………………..54

3.9. Porous silicon waveguide resonance shift for complementary DNA (Anti-sense), demonstrating the recognition of DNA binding inside the porous silicon waveguide……………………………………………………………………..54

3.10. Negligible porous silicon waveguide resonance shift for non-complementary DNA (Mismatch), demonstrating that the porous silicon waveguide can distinguish complementary and non-complementary DNA sequences…………55

3.11. No resonance shift observed upon exposure of the porous silicon waveguide to buffer solution, demonstrating the stability of the sensor against false positives……………………………………………………………………………55

3.12. Simulated resonance shift for different coverages on pore walls by 24-base target DNA, with the top x-axis showing the corresponding target DNA concentration in μM. The inset shows the zoom-in view at low DNA concentration. The point (0.002 degrees, 50 nM or 5 pg/mm^2) corresponds to the detection limit………..57

3.13. Simulated porous silicon waveguide resonance shift as a function of probe DNA hybridization percentage (bottom *x*-axis) and corresponding complementary DNA concentration (top *x*-axis), given for different probe DNA coverage on the pore walls. Larger resonance shifts occur for larger probe coverage and when a greater fraction of the probe molecules are hybridized. The inset shows the detection limit at different probe DNA coverage. At the optimal probe coverage of 50% (i.e., leaving just enough space for complementary DNA attachment), the detection limit is 50 nM………………………………………………………………………58

3.14. Revised porous silicon waveguide (method 2) resonance shift due to 100 μL of different concentrations of 3-APTES coating the oxidized pore walls…………..61

3.15. Resonance spectra of porous silicon waveguide (method 2) after oxidation, silanization, and sulfo-SMCC derivatization……………………………………62

3.16. Step-by-step reaction of cross-linking probe DNA to porous silicon by sulfo-SMCC. The oxidized porous silicon sample was first silanized with 3-APTES. The amine derivatized sample was then cross-linked to thiol-modified probe DNA with sulfo-SMCC………………………………………………………………...62

4.1. Cross-sectional SEM image of an n-type porous silicon layer…………………..68

4.2. Schematic diagram of the n-type porous silicon membrane waveguide biosensor……………………………………………………………………………69

4.3. Top view SEM of the porous silicon membrane waveguide, showing the slightly widened pores at the bottom of fabricated porous silicon layer after the electropolishing procedure separated the porous silicon layer from the silicon substrate……………………………………………………………………………71

4.4. Cross-sectional SEM image of the porous silicon membrane waveguide………72

4.5. Experimental (solid line) and theoretical (dotted line) angle-resolved attenuated total reflectance spectrum of porous silicon membrane waveguide showing the guided mode (50.5°) and substrate mode (37.9°)………………………………..73

4.6. Attenuated total reflectance spectra of n-type porous silicon membrane waveguide upon oxidation (black line), silanization (red line), and sulfo-SMCC derivatization (blue line)…………………………………………………………………74

4.7. Resonance shift of 1˚ for the n-type porous silicon membrane waveguide upon attachment of 100 μM 24-base probe DNA……………………………………...76

4.8. Control experiments where exposure to 3 M NaCl and 100 μM TCEP gives no shift for the sulfo-SMCC functionalized porous silicon waveguide……………..76

4.9. Measured angular shift of guided mode after exposure to various concentrations of 24-base pair DNA oligonucleotides. A linear fit of the data points suggests a sensitivity of 0.048˚/μM and a detection limit of 42 nM………………………...78

4.10. Control experiments showing no resonance shift for the mismatch (non-complementary) DNA………………………………………………………………78

5.1. Different biomolecular sizes relative to the same pore size, resulting in different sensitivity of detection for the porous materials based biosensors……………....81

5.2. Simulated resonance shift for different lengths of DNA at different pore wall coverages, where 8×10^{13} probes/cm^2 corresponds to 100% coverage. The slope of the linear curve is the sensitivity of detection. The 24-base DNA molecules can be detected most sensitively because their infiltration into the porous silicon waveguide causes the largest refractive index change. The simulation ignores practical infiltration challenges and assumes that the DNA molecules can infiltrate into all pores with diameters larger than the DNA length………………………83

5.3. Plan-view SEM image of a mesoporous silicon waveguide after 30 minutes of KOH soaking to open up the pores. The average pore diameter is approximately 30 nm……………………………………………………………………………84

5.4. Experimental results showing the resonance shift of porous silicon waveguides at different concentrations (25-100 μM) and different lengths (8-24 bases) of DNA. The slopes of the linearly fitted curves are the sensitivities of detection. Each data point includes an error bar, and the detection sensitivity with associated error range for each DNA length is also shown……………………………………..86

5.5. Resonance shifts for the p-type and n-type porous silicon waveguide for different length of DNA at the same 100 μM concentration………………………………87

6.1. Sensor chip setup of the porous silicon membrane waveguide biosensor……….89

6.2. Grating coupled porous silicon waveguide………………………………………91

6.3. A grating coupled porous silicon waveguide incorporating microfluidic flow cells. The grating is fabricated on flow cell cover and can be re-used. The entire area of the porous silicon waveguide is available for sensing…………………………...92

6.4. The SEM of a fabricated p-type porous silicon slot waveguide…………………93

6.5. Porous silicon waveguide interferometer sensor………………………………...94

6.6. Sensor array for high throughput sensing. The actual density of sensing elements will be higher……………………………………………………………………96

CHAPTER I

INTRODUCTION TO BIOSENSING

1.1 Definition and classification of biosensors

The detection of biomolecular interactions for different concentrations of probe and target molecules is important for medical diagnostics, drug discovery, gene expression research, environmental protection and monitoring, food safety, and anti-bioterrorism. Biosensors, which are capable of detecting such interactions, typically consist of two parts: bioreceptor and transducer. Figure 1.1 shows the typical structure of a biosensor. Probe molecules are immobilized on the bioreceptor and capture the analyte of interest, called the target. The transducer transforms this binding event into a measurable signal. Then a quantitative measurement is taken, from which information about the target can be deduced, including concentration, affinity and kinetic constants [1]. Biosensors can be classified based on either the type of bioreceptor or transducer (Figure 1.2). In terms of the bioreceptor, biosensors can be classified as being based on the interactions of antibody/antigen, nucleic acids, enzymes, proteins, and synthetic biomaterials [2-5]. In terms of the transducer, biosensors can be categorized as electrical, optical, electrochemical, mechanical, colorimetric, or any combination of the above [3, 6]. Over the past several years, the merging of the fields of nanotechnology and biosensing has led to the development of novel sensing devices [7, 8], including cantilevers [9], silicon nanowires [10], carbon nanotubes [11], and nanoparticles [12], that have the potential for ultra-sensitive biomolecular detection. For this thesis, the main focus is on nanoscale optical biosensors.

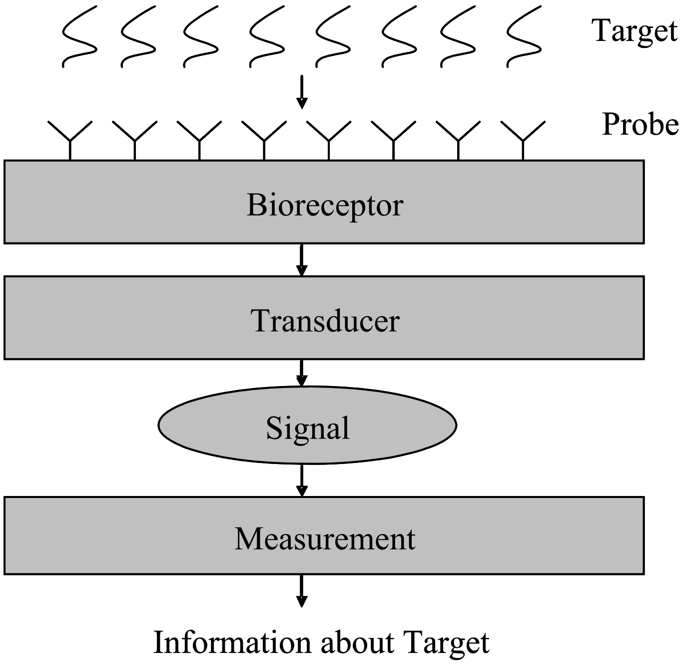

Figure 1.1. Typical structure of a biosensor, from top to bottom: target analyte binds to the probe molecules in the bioreceptor, causing a signal to be transduced. The signal is then measured quantitatively, and the information about the target (e.g. concentration, affinity, kinetic constants) can be deduced.

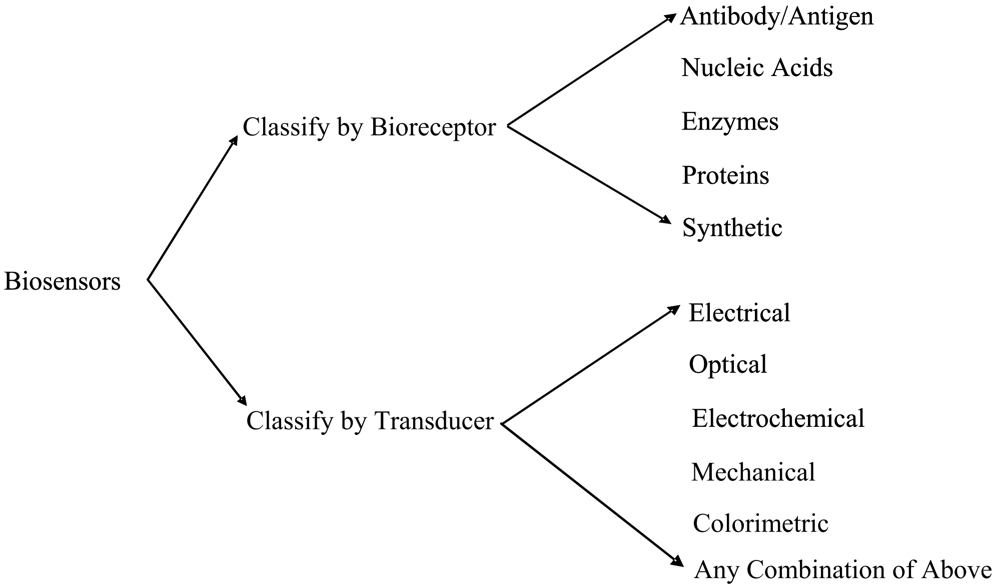

Figure 1.2. Classification of biosensors by type of bioreceptor or transducer.

1.2 Labeled and label-free biosensors

Optical biosensing traditionally relies on labeling biomolecules with fluorescent probes or radioactive isotopes [6, 13, 14] and detecting the presence of these labeled molecules by monitoring their fluorescence signal. As shown in Figure 1.3, target molecules are first bioconjugated with fluorophores before being exposed to probe molecules. A light source is then used to excite the fluorophores attached to the sensor; the fluorophores absorb photons of the excitation light, which cause the fluorophors to emit light at a longer wavelength (e.g., fluorescent light is lower energy compared to incident light). The fluorescence is detected by a photodetector, which identifies the presence of the labeled target molecules. It is important to note that a rinsing step is employed to remove unbound target molecules, ensuring that the fluorescence signal is coming only from specifically attached target molecules. Differences in the measured fluorescence intensity correlate to the number of bound target molecules. Labeled sensors can have high sensitivity, with detection limits reported as low as fM levels [6]. However, there are several disadvantages of using labeled sensors. The technique of bioconjugating fluorophores onto biomolecules is time-consuming and low yield often results. Moreover, the fluorophore modification process can inhibit the biomolecular binding efficiency, adversely affecting the sensor performance. In addition, since the fluorescence intensity is typically weak and the lifetime is short, optical detection instruments often must be of high quality [6].

Label-free biosensors that do not require the use of fluorescent molecules for biomolecule detection have the advantage of eliminating complex sample preparation techniques and improving reliability. Optical label-free biosensors often operate based on a change in refractive index due to affinity binding events of biomolecules, such as DNA hybridization or antigen-antibody binding. The refractive index change is detected, for example, by measuring a change in reflection or transmission spectra. Label-free biosensors may also utilize absorption fingerprints of molecules in the infrared [15] or terahertz regions [16].

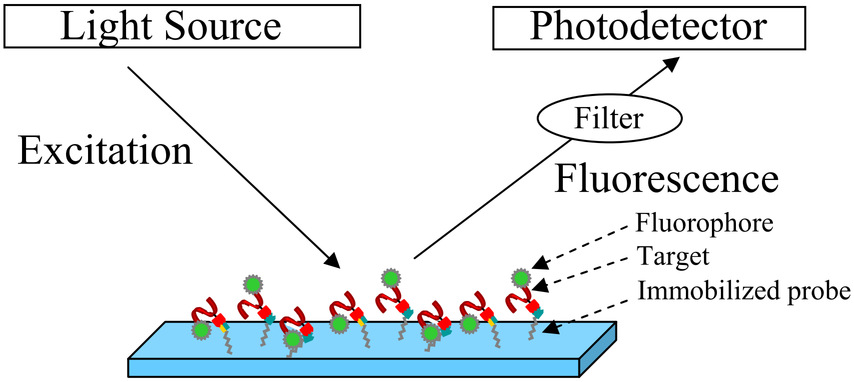

Figure 1.3. Schematic of labeled biosensor. After bioconjugation with fluorophores, target biomolecules bind to probe biomolecules (either immobilized or in solution). When excited by light of higher energy, the fluorophores emit light at a wavelength that is characteristic to the fluorophore. This fluorescence is detected, confirming the presence of the target molecules. Note that the excitation light is typically filtered out of the signal sent to the photodetector.

1.3 Evanescent wave biosensors

Many label-free optical biosensors are based on refractive index changes that results from interactions of biomolecules with evanescent waves. An evanescent wave is one that exponentially decays as it propagates. For example, the widely used, state-of-the-art surface plasmon resonance (SPR) sensor uses the evanescent wave of a surface plasmon mode, which is a collective electron oscillation wave existing at the interface between metal and dielectric materials [17, 18]. The wavevector of the SPR mode is given by [19]

$$k_{SPR} = \frac{2\pi}{\lambda}\sqrt{\frac{\varepsilon_{metal}\varepsilon_{dielectric}}{\varepsilon_{metal} + \varepsilon_{dielectric}}} \tag{1.1}$$

where λ is the wavelength in vacuum, ε_{metal} is the complex dielectric constant of the metal, and $\varepsilon_{dielectric}$ is the dielectric constant of the dielectric material. Gold and silver are the most commonly used metals to support plasmonic activity. In order to couple light into an SPR mode, the component of the incident light wavevector parallel to the metal-dielectric interface must match that of the SPR mode, which requires the use of a prism or grating. The SPR mode is very sensitive to small changes in refractive index near the metal-dielectric interface, due to the evanescent field of the SPR mode. Figure 1.4 illustrates the concept of SPR biosensing. Probe biomolecules are immobilized on the metal surface of the SPR sensor. In this illustration, a prism in the Kretschmann configuration is used. Light incident from the prism at the proper angle allows coupling to an SPR mode. At this angle, a resonance dip is measured in the attenuated total reflectance spectrum. When target biomolecules bind to the probe biomolecules, they induce a refractive index change in the vicinity of the metal surface. This refractive index change causes a perturbation of the SPR mode and its wavevector, which in turn changes the resonance angle θ of the surface plasmon mode. By monitoring the resonance angle, biomolecular binding events can be detected. The magnitude of the angular resonance shift quantifies the number of target molecules attached to the sensor. One of the main limitations of SPR sensing is that the interaction between biomolecules and the electrical field is not optimal. Stronger field-matter interactions between the electric field and biomolecules lead to more sensitive detection capabilities. The field evanescently decaying away from the metal-air interface (typically dying out in a few hundred nanometers) and losses in the metal film that inhibit the propagation of surface plasmons along the interface limit the interaction volume of the sensor. Moreover, the relatively small available surface area for biomolecular immobilization further limits the capabilities of SPR sensors for small molecule detection [17, 19].

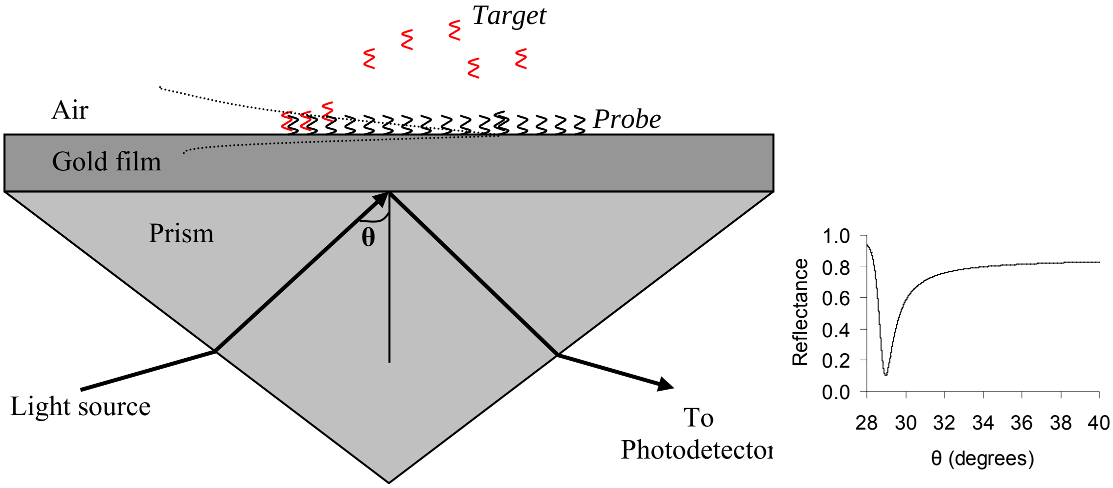

Figure 1.4. Surface plasmon resonance (SPR) biosensor structure, sensing mechanism and typical attenuated total reflectance (ATR) spectrum. The dashed lines show the electrical field profile of the surface plasmon mode existing between the metal (gold) and the dielectric (air) layers. The resonance in the ATR spectrum corresponds to the angle at which the surface plasmon mode is excited. Biomolecular binding increases the refractive index in the vicinity of the metal surface and induces a change in the angle at which the surface plasmon mode is excited.

Several other types of evanescent wave biosensors have been demonstrated on silicon or silica platforms, including fiber optic sensors [20, 21], planar waveguide sensors [22], and, more recently, ring resonator, disk resonator and silicon wire waveguide sensors [23-25]. The ring and disk resonators achieve high sensitivity detection through the design of very high quality factor resonant structures that allow the evanescent field to interact with biomolecules over multiples cycles of the confined wave. The silicon wire waveguide design enables improved detection sensitivity over traditional slab waveguide sensors by utilizing a thinner waveguide core that allows a greater fraction of the electric field to leak out into the cladding and interact with biomolecules immobilized on the core surface. Arranged in a Mach-Zehnder configuration, silicon wire waveguides also benefit from longer field-molecule interaction lengths [25]. Figure 1.5 illustrates a traditional slab waveguide evanescent-wave sensor for which biomolecules are immobilized on the planar surface of the waveguide. Note that the geometry would be similar for fiber optic, ring resonator, and disk resonator sensors. The operation of the evanescent-wave waveguide sensor is analogous to the evanescent-wave SPR sensor except that biomolecules interact with the evanescent wave of guided modes rather than surface plasmon modes. As shown in Figure 1.5, the field profile of a waveguide mode is such that it is sinusoidal in the waveguide core and evanescent outside of the waveguide [26]. The refractive index change in the vicinity region of the waveguide surface resulting from probe-target binding can be measured by either a change in transmitted wave phase or intensity, or a change in the wavelength or angle of the light that is coupled into the waveguide. The limitations of the waveguide sensor are the same as those of SPR sensors: relatively weak interactions between biomolecules and electrical field, and limited available surface area.

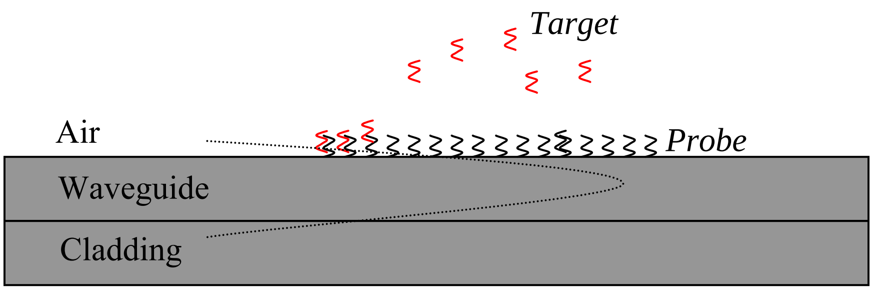

Figure 1.5. Schematic of planar waveguide or fiber optic (with part of the top cladding stripped) biosensor. Biomolecular binding events change the refractive index in the vicinity of the waveguide core surface. This refractive index change is detected as a change in the propagating wave phase or intensity, or as a change of the angle or wavelength of light coupled into the waveguide.

1.4 Porous materials based biosensors

In order to overcome the limitations of evanescent wave-based sensors and achieve high sensitivity, label-free detection of small molecules, the surface area available for molecular binding must be increased and propagating waves instead of evanescent waves should be used to interact with biomolecules. Porous materials have been proposed as an extension to existing evanescent wave-based sensor technology to increase the active sensing area. For example, as illustrated in Figure 1.6, a thin layer of porous material can be placed on top of an SPR sensor to enable more biomolecules to be immobilized and more molecules to interact with the evanescent field. In this way, the probability of capturing and detecting target biomolecules is enhanced. Research utilizing this technique includes side coating of porous sol-gel on fiber or optical waveguide sensors [27, 28], adding a mesoporous silica film on top of the gold film of an SPR sensor [29] and the addition of a porous Al_2O_3 film on top of SPR sensors to enhance the SPR signal amplitude [30] and SPR-excited fluorescence [31].

Since metals typically have the real part of their refractive index below 1, a variation of the porous material enhanced SPR is a waveguide structure for which the porous material acts as the waveguide core and the metal layer acts as the cladding. Waveguide modes instead of SPR modes are interrogated for biosensing. The main advantage is that waveguide modes have the propagating field confined in the waveguide core and biomolecules interact with the confined propagating wave instead of an evanescent wave. The increased percentage of light-matter interaction between the optical field and the biomolecules to be detected improves the detection sensitivity. Waveguide modes also typically have narrower resonances than surface plasmon modes due to lower losses, which improves the resolution of sensing. Examples of metal-cladded waveguides include a porous TiO_2 waveguide with gold cladding [32] and a perforated SiO_2 waveguide with gold cladding [33]. The primary disadvantage of these "porous core and metal cladding" waveguides is that they are lossy due to the metal cladding that is absorptive (large value for imaginary part of refractive index). In addition, there are challenges involved with achieving high pore densities and developing reliable functionalization procedures for some porous materials.

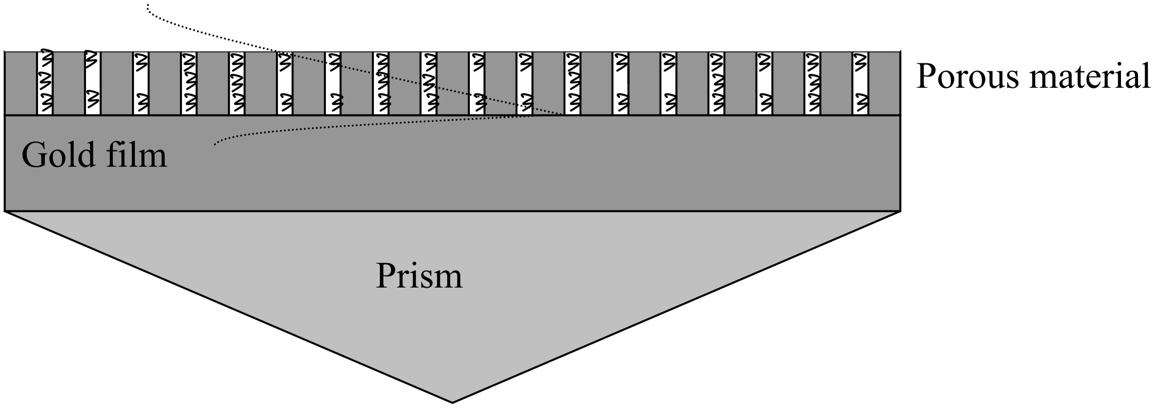

Figure 1.6. Porous material added on top of an SPR sensor enhances the surface area. More biomolecules can be immobilized and the sensitivity for small molecule detection is improved.

Biosensors based entirely on porous materials, such as porous silicon [34-40], porous aluminum [41], porous zeolite [42] and porous glass [43] have also been investigated. Porous silicon is a particularly attractive material for biosensing applications. Like other porous materials, it has a high surface area to volume ratio, offering the possibility of immobilizing a large number of biomolecules, which significantly increases the probability of capturing target species. The pore density can be as high as 10^9-10^{10} pores cm^{-2} [44, 45]. Biofunctionalization of porous silicon has been well studied and many routine procedures for biomolecular attachment have been reported [38]. In addition, porous silicon has the advantages of being compatible with standard semiconductor processing and having a widely tunable pore size (a few nanometers to several microns), which allows infiltration of target biomolecules of the appropriate size while excluding larger-sized non-specific species [36, 46]. There are many types of porous silicon optical devices that are used for sensing, including the porous silicon single layer interferometer, multilayer Bragg reflector, rugate filter, and resonant microcavity. In Chapter 2, a detailed review of the various porous silicon optical biosensors will be given, and the advantages of our proposed porous silicon waveguide biosensor will be discussed.

1.5 Objective and overview of the dissertation

The objective of this dissertation is to design and optimize a porous silicon waveguide biosensor, robustly and reproducibly functionalize the sensor for DNA hybridization detection, theoretically and experimentally characterize the sensor's performance, and identify future research areas to improve the sensor performance. An "ideal" biosensor should have (1) high sensitivity and a low detection limit; (2) high selectivity and specificity; (3) excellent repeatability and reproducibility; (4) stability over time and under different physical and chemical conditions; (5) large dynamic range; (6) low cost; (7) portability; (8) fast response; (9) integrated design; (10) high through-put; and (11) reusability. Throughout this work, many of the above factors will be considered.

Chapter 2 will cover p-type porous silicon background and characterization, and the fabrication of p-type porous silicon waveguides. Chapter 3 will discuss the sensing operation of the p-type porous silicon waveguide biosensor, including the sensing of liquids and the detection of DNA hybridization. A theoretical comparison of the porous silicon waveguide biosensor with the SPR biosensor for small molecule detection will also be presented. Chapter 4 presents the design and fabrication of an n-type porous silicon membrane waveguide and the demonstration of its sensing operation by DNA hybridization detection. Experimental nM detection is demonstrated. Chapter 5 will discuss the effects of biomolecular size on the sensitivity of porous materials-based biosensors. A comparison between the p-type, smaller pore porous silicon waveguide and the n-type, larger pore porous silicon waveguide will also be given. In Chapter 6, further research to improve and expand the sensor performance will be suggested, and general prospects for biosensor research will be discussed.

CHAPTER II

POROUS SILICON WAVEGUIDE STRUCTURE

2.1 Porous silicon background and characterization

Porous silicon is a nanostructured material consisting of air pores in a silicon matrix. By controlling the pore size and density, the optical properties of porous silicon can be modified. In this section, the formation and characterization of porous silicon is presented. A number of porous silicon optical structures are also discussed.

2.1.1 Pore formation

Porous silicon is typically fabricated in a straightforward manner by electrochemical etching of a silicon wafer in hydrofluoric acid electrolyte [44, 45], although stain etching [47] and laser ablation [48] have also been used to create porous silicon. During electrochemical etching, the charge carriers in the silicon wafer and fluorine ions in the electrolyte meet at the silicon surface. Assisted by charged carriers in the silicon wafer, dissolution of silicon atoms begins when one fluorine ion replaces one hydrogen atom bound to the silicon atom. Fluorine ions continue to bind to silicon atoms, and hydrogen gas is generated. After all four bonds of a silicon atom are broken, the silicon atom becomes soluble in solution as SiF_6^{2-}, leaving behind an atomic vacancy. Pore propagation preferentially takes place at the pore tips where the electric field is concentrated and charge carriers are available. Detailed descriptions of pore formation mechanisms can be found elsewhere [45, 49-51].

Porous silicon can have pore sizes ranging from a few nanometers to several microns. The IUPAC (International Union of Pure and Applied Chemistry) guidelines define ranges of pore size as micropore (≤2 nm), mesopore (2-50 nm), and macropore (>50 nm) [44]. The pore size along with other porous silicon characteristics, such as porosity, etching rate, and pore morphology, depend on the silicon wafer doping, electrolyte composition, and etching conditions (i.e., applied current density, temperature, and illumination) [45]. In this work, both mesoporous and macroporous silicon are used due to their appropriate size range for DNA detection. In this chapter and in Chapter 3, we focus on mesoporous silicon with its fabrication conditions given in the following discussion. Descriptions of macroporous silicon and its fabrications condition are given in Chapter 4.

2.1.2 Porosity characterization

In this work, mesoporous silicon is formed by electrochemical etching of boron doped p^+ silicon with a resistivity of 0.01Ω·cm and <100> growth direction. The electrolyte is 15% hydrofluoric (HF) acid, which is composed of 175 mL 99% ethanol and 75 mL 50% aqueous HF. The porous silicon fabrication procedure is given in Appendix A. Given these specifications for the silicon wafer and HF electrolyte, characterization of the porosity and etching rate of porous silicon at different current densities was carried out.

The porosity of porous silicon single layer samples etched at different current densities was determined by gravimetric analysis. While the characterization experiments were performed on single layer porous silicon samples, it is important to note that multilayer porous silicon samples can be fabricated by simply changing the applied current density. The formation of a new porous silicon layer beneath an existing porous silicon layer does not affect the properties of the previously etched layer. This is due to the depletion of free carriers in the nanostructured silicon matrix of the previously formed layer, which inhibits further etching in that layer, and the electric field concentration at the curved pore tips, which promotes etching only at the base of the pores.

As shown in Equation 2.1, porosity can be obtained from the weight of the wafer sample before etching (m_1), immediately after etching porous silicon (m_2), and after dissolving porous silicon by saturated NaOH solution (m_3).

$$\%P = \frac{m_1 - m_2}{m_1 - m_3} \times 100 \tag{2.1}$$

Figure 2.1 (a) shows the experimentally measured porosity vs. current density trend. Multiple data points are taken at several current densities, error bars are shown, and the average values are fitted with an exponential curve. The achievable porosity range is 56%-80%. Porous silicon with porosity lower than 56% is not reproducible, and porosities higher than 80% result in electro-polishing where silicon is uniformly removed.

For a given porosity, the refractive index of porous silicon can be obtained by effective medium theory. If the wavelength in question is much larger than the pore size, then the electromagnetic wave will not be able to resolve the fine features of the porous silicon, and the resulting porous silicon refractive index is the weighted average of the refractive indices of the air pores and silicon matrix. There are three primary effective medium models for linking porosity to the refractive index of porous silicon: Bruggeman, Maxwell-Garnett, and Looyenga. The Bruggeman effective medium takes into account connected networks for low porosities and isolated particles for high porosities [52]. The dielectric constant of porous silicon is given by:

$$\text{Bruggeman:} \qquad (1-P)\frac{\varepsilon_{Si}-\varepsilon_{PSi}}{\varepsilon_{Si}+2\varepsilon_{PSi}}+P\frac{\varepsilon_{void}-\varepsilon_{PSi}}{\varepsilon_{void}+2\varepsilon_{PSi}}=0 \qquad (2.2)$$

where P is the porosity, ε_{Si} is the dielectric constant of silicon, ε_{PSi} is the dielectric constant of the porous silicon, and ε_{Void} is dielectric constant of air. The refractive index of porous silicon is the square root of dielectric constant. In most of this work, the Bruggeman effective medium model is used to calculate the effective refractive index of porous silicon. Figure 2.1 (b) shows the relationship between porous silicon porosity and refractive index as given by the Bruggeman model.

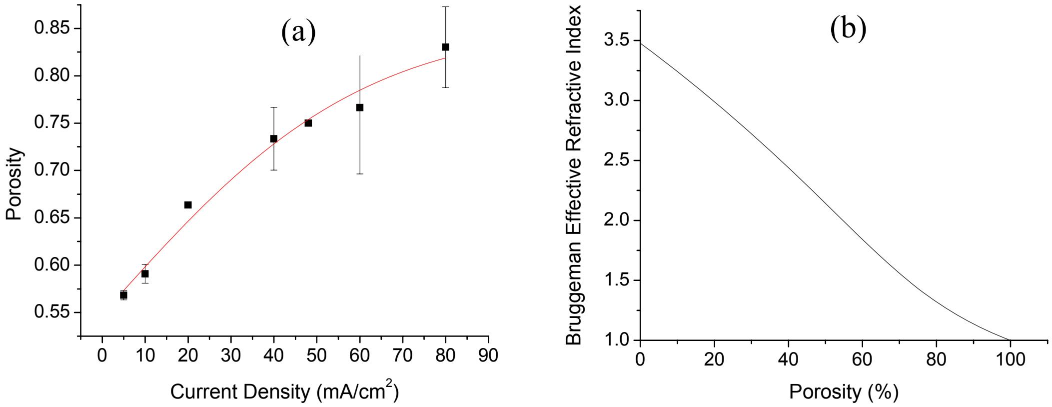

Figure 2.1. (a) Porous silicon porosity that results from the application of different current densities during electrochemical etching. (b) Bruggeman effective refractive index at different porous silicon porosities, assuming a wavelength of 1550 nm.

The Maxwell-Garnett effective medium model is appropriate for material systems with high porosities and isolated spherical particles separated by large distances [53]. The dielectric constant of porous silicon is based on the Maxwell-Garnett model is given by:

$$\text{Maxwell-Garnett:} \qquad (1-P)\frac{\varepsilon_{Si}-\varepsilon_{void}}{\varepsilon_{Si}+2\varepsilon_{void}}=\frac{\varepsilon_{PSi}-\varepsilon_{void}}{\varepsilon_{PSi}+2\varepsilon_{void}} \tag{2.3}$$

The Looyenga effective medium model is typically applied for densely packed composites and often fits high porosity porous silicon materials best due to its consideration of an interconnected network for all porosities [54]. The dielectric constant of porous silicon based on the Looyenga model is given by:

$$\text{Looyenga:} \qquad \sqrt[3]{\varepsilon_{PSi}}=\sqrt[3]{\varepsilon_{Si}}(1-P)+\sqrt[3]{\varepsilon_{void}}P \tag{2.4}$$

Modified effective medium approximations have also been developed that take into account silicon dioxide inside porous silicon [55] and birefringence of porous silicon [56]. These modified models have also been utilized in part of this work.

2.1.3 Etching speed characterization

To determine the etching speed at different current densities, single layer porous silicon samples were etched at a given current density for different durations, and their thicknesses were measured by scanning electron microscopy (SEM). Figure 2.2 shows the etching speed in nm/s at different current densities.

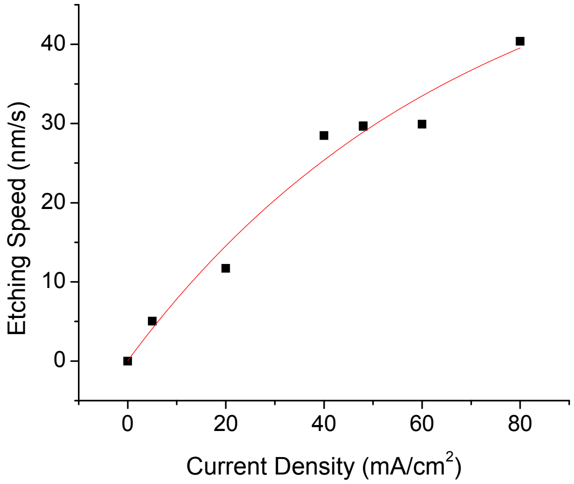

Figure 2.2. Etching rate of porous silicon at different applied current densities.

2.1.4 Porous silicon biosensing

Given the control of porous silicon refractive index and layer thickness, many thin-film optical devices based on multi-layered porous silicon films, such as mirrors, filters, waveguides, microcavities, and anti-reflection coatings [57-61], have been formed by appropriately adjusting the current density and etching time. Since the first report of label-free porous silicon biosensing in 1997 [40], many porous silicon optical devices have been used for this application. Over the last decade, there has been significant research progress on the chemical and biological functionalization of porous silicon [39, 62, 63], and the application of porous silicon in chemical and biological sensing [6, 38, 63-65]. A brief discussion of several of the researched porous silicon optical sensing devices is provided.

The simplest porous silicon optical sensing device is a single layer interferometer. As show in Figure 2.3 (a), incident light waves are reflected at the top and bottom interfaces of the single porous silicon layer, and interfere with each other in air. Due to constructive or destructive interference at various incident wavelengths, an interference fringe pattern, such as the one shown in Figure 2.3 (b), results. Biomolecular binding events inside the porous silicon increase the effective refractive index of the porous silicon layer and shift the interference pattern towards longer wavelength. There have been reports of porous silicon interferometers for detection of DNA [40], proteins [66-68], E-coli [69], DNA damaging chemicals [70, 71], hydrogen [72], organic vapors [73, 74], chemical warfare agents [75], and a double porous silicon layer interferometer for detection of biomolecules of different sizes [46]. For these sensors, there is no optical wave confinement in the porous silicon layer. Rather, the porous silicon interferometer biosensor depends on the refracted optical wave to interact with the biomolecules in the porous silicon pores. Without confinement, the field-biomolecule interaction is not very strong, which limits the ultimate sensitivity of the structure for sensing applications. Nevertheless, with optimized biofunctionalization conditions and signal processing, sub-nanomolar detection sensitivity is possible.

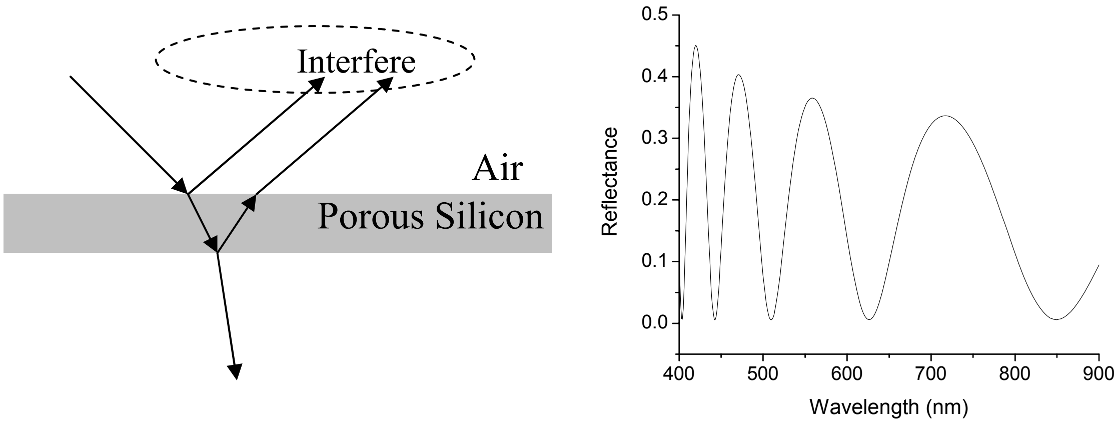

Figure 2.3. Single layer porous silicon interferometer and its simulated reflection fringes.

A porous silicon Bragg reflector is a periodic multilayer structure consisting of alternative layers of higher and lower porosity. The reflected optical waves at each interface interfere constructively to create a stopband of high reflectance, as shown in Figure 2.4. The optical thickness of each layer is designed to be one quarter of the mid-band wavelength in that layer. Consequently, higher porosity layers with lower refractive index must be thicker than lower porosity layers with higher refractive index.

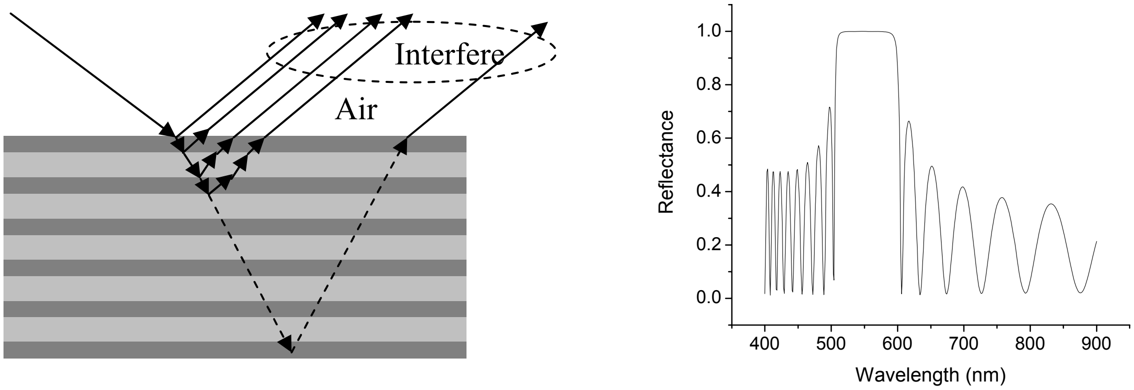

Figure 2.4. Porous silicon multilayer Bragg reflector and its simulated reflectance spectrum.

Similar to the porous silicon single layer, the reflection band and side interference fringes of the Bragg mirror spectrum shift to longer wavelengths upon biomolecular binding inside porous silicon due to the increase of the porous silicon effective refractive index. Porous silicon Bragg mirrors can be removed from the porous silicon substrate and broken into pieces by sonication. These optically encoded “smart dust” or “smart particles” have been used for the detection of volatile organic compounds [76, 77] by monitoring their reflectivity.

A modified Bragg mirror is the porous silicon rugate filter, for which the reflectance stopband is much narrower spectrally than that of a Bragg reflector. The optical thicknesses of the layers of the porous silicon rugate filter vary as a sinusoidal function of etching depth. Biomolecular binding inside porous silicon is detected by a shift of the reflection peak. The porous silicon rugate filter biosensor has been characterized [78] and used for detection of proteins [79] and enzymes [80]. Porous silicon rugate filter films can also be separated from the silicon substrate and made into particles by mechanical grinding or ultrasonic fracture. These are also called optically encoded “smart dusts” or “smart particles” capable of sensing. There are reports of smart dust based on a single rugate filter for detection of organic vapors [81], and smart dust based on double rugate filters that self-orient along the interface between water and organics for possible application in biosensing [82]. The limitation of Bragg mirror and rugate filter sensors is that there is no strong field confinement, which limits sensitivity. Moreover, the increased total thickness of the multilayer structures compared to a single layer leads to increased analyte volume requirements for many sensing applications.

In order to achieve strong field confinement in a porous silicon optical structure for more sensitive sensing applications, porous silicon microcavities have been fabricated. A microcavity is a multilayer structure in which there is a defect layer between two Bragg reflectors. The “defect” layer is a layer that is not of quarter wavelength optical thickness and thus breaks the periodicity of the Bragg reflectors. Optically, the defect layer causes destructive interference at a particular wavelength, leading to a resonance dip in the reflectance spectrum. Figure 2.5 shows the structure and the field profile of a multilayer porous silicon microcavity, along with its reflectance spectrum. The resonance is sharp and narrow due to strong field confinement in the central defect layer. Increasing the number of periods in the Bragg reflectors leads to better field confinement in the defect layer and a sharper resonance. There have been several reports of porous silicon microcavity biosensors for sensitive detection of organic solvents [83], explosives [84], nitrogen dioxide gas [85], DNA hybridization [34, 86], proteins [36, 87], bacteria [35] , enzymes [88], and peptide synthesis [89], and for monitoring the alcoholic strength of wine [90].

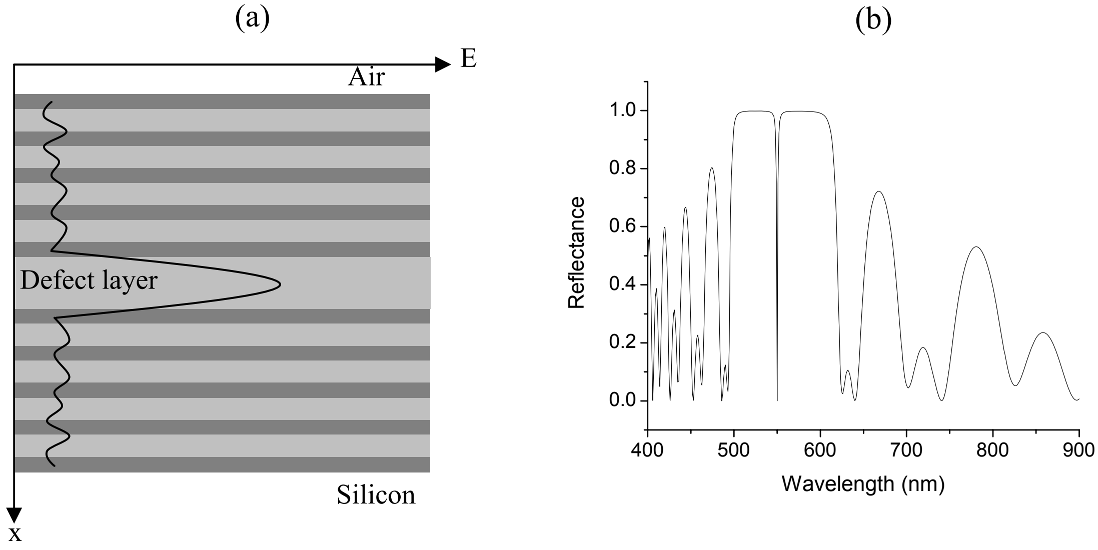

Figure 2.5. Porous silicon microcavity and its simulated reflectance spectrum.

While porous silicon microcavities theoretically have higher sensitivity than non-resonant single layer interferometers and Bragg mirrors [91], due to the thickness and field profile of the microcavity, large analyte volumes are required and response times are limited by the mass transport of molecules into the defect layer. From the field profile show in Figure 2.5 (a), it is clear that the porous silicon layers above the central microcavitydefect layer have weak field-molecule interaction. Consequently, in order to achieve the high theoretical detection sensitivity, both probe and target biomolecules must diffuse through the top layers and bind in the central cavity layer. Hence, the sensor response time and number of biomolecules required for detection are increased.

Recently, porous silicon waveguides have been proposed as thin, resonant sensing structures for which highly sensitive and fast response sensing is achievable [92, 93]. While porous silicon waveguides were previously used to detect the presence of liquids [94], newly proposed designs that are the subject of this work enable high sensitivity detection of biomolecules. Figure 2.6 shows the structure of a typical porous silicon waveguide. It is a thin optical structure that has strong field confinement in the high index porous silicon layer (as shown by the field profile). The analyte to be detected is exposed to the most sensitive layer, the high index layer, first.

This thesis reports the theoretical investigation and experimental demonstration of the porous silicon waveguide biosensor. Two waveguide structures are investigated. The first one is a p-type porous silicon waveguide with 20-30 nm pores. The second waveguide structure is an n-type porous silicon membrane waveguide with 100 nm pores that utilizes a polymer cladding layer. We will first begin with the design and fabrication of p-type porous silicon waveguides.

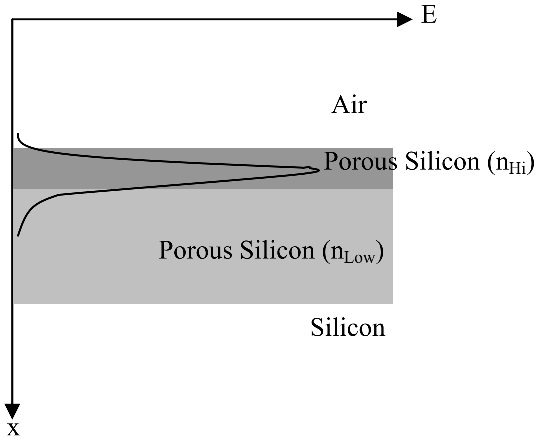

Figure 2.6 Porous silicon waveguide and its qualitative field profile.

2.2 Porous silicon waveguide design, optimization, and fabrication

Generally, an optical waveguide consists of three layers: a high refractive index layer sandwiched between two lower refractive index layers. As shown in Figure 2.6, one or both of the cladding layers can be air. Total internal reflection at the interfaces between the high and low refractive index layers enables light to be guided in the high index layer. The thickness of the high index layer determines the number of modes (i.e., electric field distributions) supported by the waveguide [26]. As shown in Figure 2.6, the porous silicon waveguide used in most of this work consists of two porous silicon layers: a low porosity (high index) layer that is the waveguiding layer, and a high porosity (low index) layer that is the cladding layer. Air above the low porosity layer provides mode confinement at the top waveguide interface. Most of the field energy is confined in the waveguiding layer. There are many ways to couple light into the waveguide, such as end-fire coupling [95], grating coupling [26], and prism coupling [26]. End-fire coupling generally is not very efficient and requires matching of the incident field profile to the waveguide mode field profile. Grating coupling tends to be more efficient but requires the fabrication of periodic, subwavelength features using specialized lithographic equipment. Prism coupling is also an efficient means of coupling light into a waveguide, and is chosen as the method used in this work.

In the original theoretical report of biosensing using a porous silicon waveguide [92], the sensor is in the Kretschmann configuration (see Figure 2.7), where light is coupled into the waveguide from the back side of the waveguide. At the interface between the high porosity porous silicon layer and the silicon substrate, an evanescent wave is generated due to total internal reflection. Coupling of the evanescent wave into the waveguide is possible if, at angle θ, the horizontal component of the wavevector of the incident beam matches that of the waveguide mode [26].

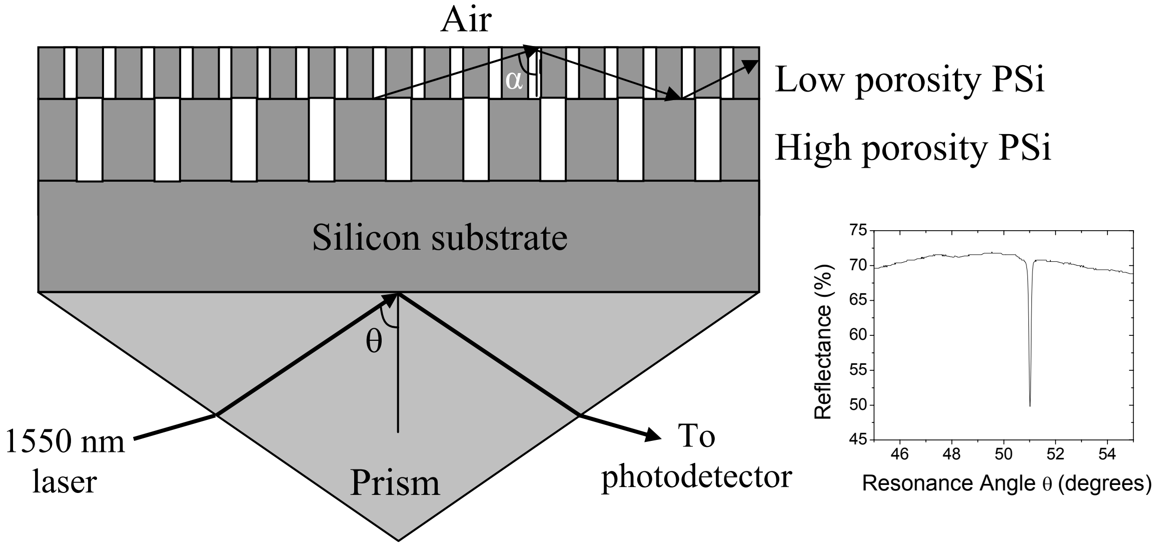

Figure 2.7. Porous silicon waveguide in the Kretschmann configuration, with a typical attenuated total reflectance spectrum shown in the inset.

The waveguide mode is determined by the waveguide structure, which includes the waveguide layer refractive index and thickness, and the cladding layer refractive indices (assuming that the cladding layers are thick enough to efficiently confine light in the waveguide layer). Equation 2.5 gives the condition for the coupling angle [26]

$$\frac{2\pi}{\lambda} n_{WG} T_{WG} \sin\alpha + \psi_{LH} + \psi_{LA} = k\pi (k = 0,1,2...) \tag{2.5}$$

where λ is the incident beam wavelength in vacuum, n_{WG} is the waveguide (i.e., the low porosity porous silicon) refractive index, T_{WG} is its thickness, α is the angle of propagation in the waveguide layer, ψ_{LH} is the phase change due to total reflection at the low porosity and high porosity layer interface, and ψ_{LA} is the phase change at the low porosity and air interface. From Snell's Law,

$$n_{WG} \sin\alpha = n_{prism} \sin\theta \tag{2.6}$$

where n_{prism} is the prism refractive index, θ is angle of incidence at the prism base which can be measured directly. At an angle θ and a corresponding α that satisfies Equation 2.5, a detector placed at the output face of the prism detects a minimum in reflectance due to the coupling of light into the waveguide. Absorption and scattering losses in the waveguide ensure that not all of the light is coupled back out through the prism. A resonance dip in the attenuated total reflectance spectrum is observed at angle θ, which corresponds to the waveguide resonance and the condition for which the field is coupled into and confined in the low porosity porous silicon layer. Here it is noted that since the wavevector of the guided mode depends on the refractive index of the waveguide, the resonance angle changes when biomolecules are infiltrated into the porous silicon waveguide core for sensing applications.

The waveguide sensor design in Figure 2.7 was intended to replace the expensive SPR sensor chip coated with gold (see Figure 1.4). By retaining the Kretschmann configuration (prism at the back of the sensor chip), direct integration of the porous silicon waveguide into existing SPR instrumentation with microfluidics for real time measurements of biomolecular interactions would be possible. Unfortunately, the sensor design was not experimentally achievable. There was inevitably an air gap between the prism and silicon substrate. The evanescent wave initiated at the prism base exponentially decays away from the prism base. In order to couple light into the waveguide, the evanescent wave must travel through several hundred microns of the silicon substrate. Moreover, the highly doped silicon wafer is not transparent due to free carrier absorption. Figure 2.8 shows the transmission of 1550 nm laser light through different thicknesses of silicon substrate, as measured by a Fourier Transform Infrared Spectrometer (FTIR, Bruker Tensor 27 equipped with PMA 50). For a typical silicon wafer of 500 μm thickness, less than 10 % of propagating light energy is transmitted through the wafer. As a result of these factors, the evanescent wave generated at the prism base cannot reach the porous silicon waveguide core.

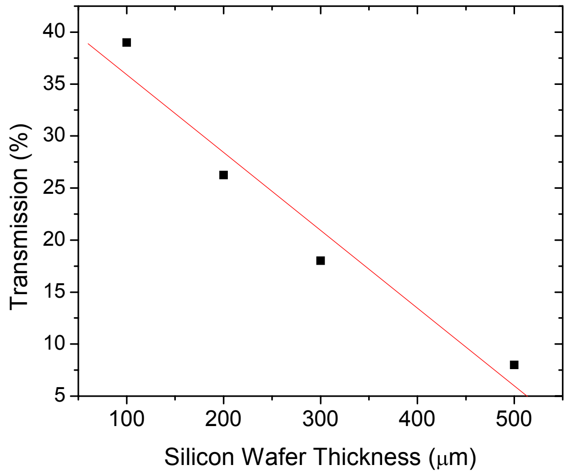

Figure 2.8. Measured transmission through various thickness silicon substrates at 1550 nm using FTIR. The 500 μm and 300 μm samples were polished from the wafer vendor. The 200 μm and 100 μm samples were thinned by creating a sacrificial porous silicon layer that was subsequently dissolved by exposure to sodium hydroxide.

In order to couple light into the porous silicon waveguide, the Otto configuration was utilized. As shown in Figure 2.9, a prism was used to evanescently couple a laser beam into the waveguide at the front side of the porous silicon waveguide. The coupling requirements are similar to those for the porous silicon waveguide in the Kretschmann configuration: coupling of the evanescent wave into the waveguide requires the horizontal component of the wavevector of the incident beam to match that of the waveguide mode [26]. The air gap between the prism and the top porous silicon layer is necessary as a cladding layer of the waveguide. The air gap can be controlled in real time by adjusting the coupling pressure that pushes the porous silicon waveguide sample toward the prism, in order to achieve the most efficient coupling of light into the waveguide. The air gap is generally several hundred nanometers thick, through which the evanescent wave can survive and couple into the porous silicon waveguide.

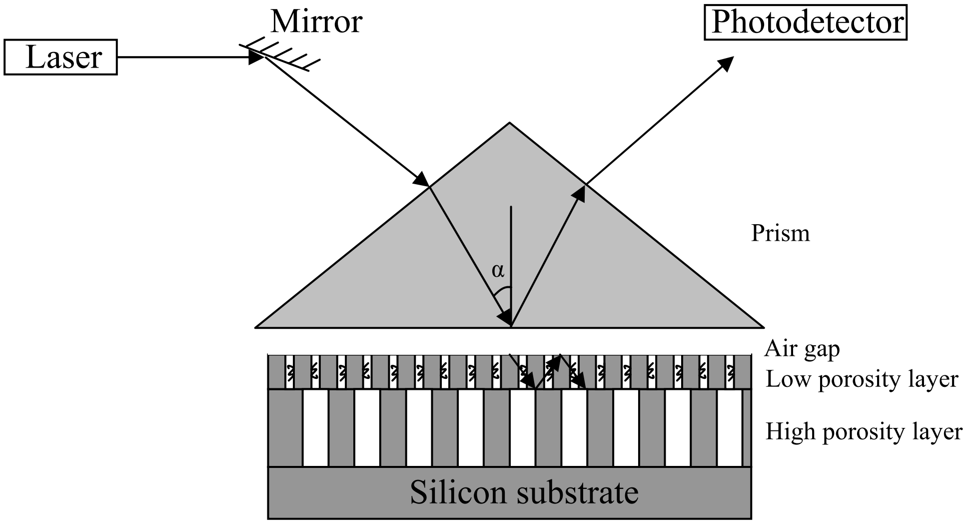

Figure 2.9. Schematic of porous silicon waveguide biosensor in the Otto configuration, consisting of a low porosity (high refractive index) porous silicon layer, a high porosity (low refractive index) porous silicon layer, and air gap. Total internal reflection enables waveguiding in the low porosity porous silicon layer. A prism is used to couple light at a specific angle α into the waveguide mode through an evanescent wave. The attenuated total reflectance spectrum is similar to the one shown in Figure 2.7.

For the sensor to be sensitive to a small refractive index change, a resonance with high quality is needed. The quality of a resonance is proportional to energy confinement and inversely proportional to energy dissipation per cycle. Hence, stronger field confinement and lower losses give higher quality waveguide resonances. Analytical equations based on a pole expansion method for obtaining the optimum parameters of the waveguide for high quality resonances have been developed [92]. The optimization procedure is to design the thicknesses of the three layers (i.e., air gap, low porosity layer, and high porosity layer) with specific requirements to enable confinement and guiding of light in the waveguide. The air gap thickness needs to be optimized because if the air gap is too thick, the coupling is not efficient and the resonance dip is shallow. A shallow resonance may disappear completely during the functionalization steps necessary for biosensor preparation that increase the effective refractive index of the waveguide. If the air gap is too thin, over-coupling may occur. In this case, the air gap is so small that some optical energy in the waveguide back-couples into the prism via an evanescent wave and reaches the detector. This effectively increases the resonance width, which is not desirable for achieving high sensitivity biosensors. During measurements, real time adjustment of the air gap size is possible by adjusting the coupling pressure between the prism and the waveguide. Figure 2.10 shows the effect of coupling pressure on resonance width of a waveguide (thermally oxidized at 900 ˚C for 10 minutes) where higher pressures indicate smaller air gap thicknesses. The air gap is typically several hundred nanometers thick with these coupling pressures. Appropriate pressure is obtained based on the tradeoff between the resonance width and resonance depth. It is important to note that varying the coupling pressure changes the resonance width and depth, as well as the absolute position of the resonance angle (see Figure 2.10). Maintaining a constant coupling pressure is essential during sensing operation.

The design requirements for the thickness of the high porosity layer require that the layer is sufficiently thick to prevent light leakage into the silicon substrate. For a waveguide in the Kretschmann configuration, theory based on a pole expansion method can be used to predict an optimal thickness [92] (see MATLAB code in Appendix B). For the Otto configuration, calculations based on the transfer matrix method suggest that layers thicker than approximately 2 μm will confine the waveguide mode in the low porosity layer without any light leakage. Experimentally, however, no further improvement in the resonance quality was observed for cladding thickness greater than approximately 1.3 μm.

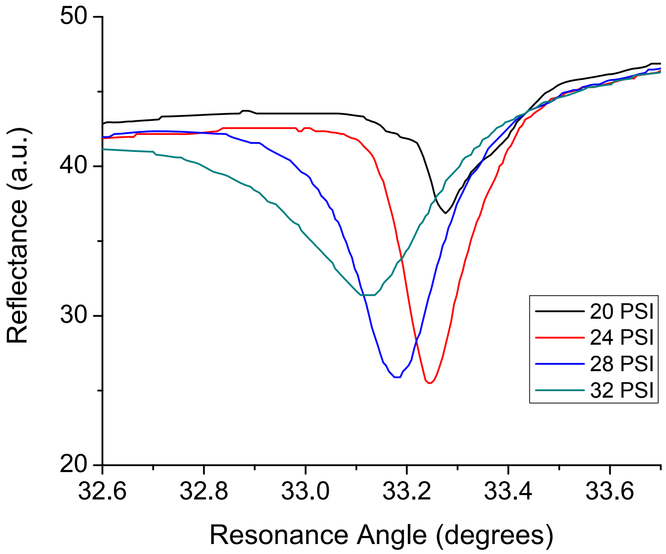

Figure 2.10. Effect of adjusting coupling pressure between the prism and porous silicon waveguide on waveguide resonance quality. The greater the applied pressure, the smaller the air gap between the prism and porous silicon waveguide. The best resonance quality is obtained at 24 psi.

The thickness of the waveguiding layer must be optimized to achieve optimal optical mode confinement. If the waveguiding layer is too thick, there is not as much spatial confinement of optical energy so the interaction between light and target materials in the porous silicon waveguide is not maximized. If the waveguiding layer is too thin, the waveguide mode will not be well-confined and will leak out of the waveguide or the waveguide mode may not exist at all. In this work, the waveguides were optimized for single mode operation. It is also possible to optimize thicker porous silicon waveguide layers for multimode operation; however, the thicker layers require larger analyte volumes for sensing applications. The optimal porous silicon waveguide thickness for single mode operation was calculated using theory based on pole expansion presented in [92] and then experimentally optimized. Porous silicon waveguides with different thicknesses were measured with a Metricon 2010 prism coupler. Figure 2.11 shows the measured waveguide resonance width (full width at half maximum) for different waveguiding layer thicknesses, using incident light at wavelengths of 633 nm (Helium-Neon laser) and 1550 nm (diode laser), respectively. Both light sources were transverse electric (TE) polarized. For these experiments, an air gap corresponding to 24 psi pressure and a high porosity porous silicon cladding layer with thickness greater than 1.5 μm were used. As observed from Figure 2.11, the waveguide resonance obtained using infrared (IR) light is about one order of magnitude narrower than the waveguide resonance obtained using visible light. This is expected due to larger absorption losses in silicon at 633 nm [96]. Therefore, waveguides designed for 1550 nm light are used throughout the remainder of this work.

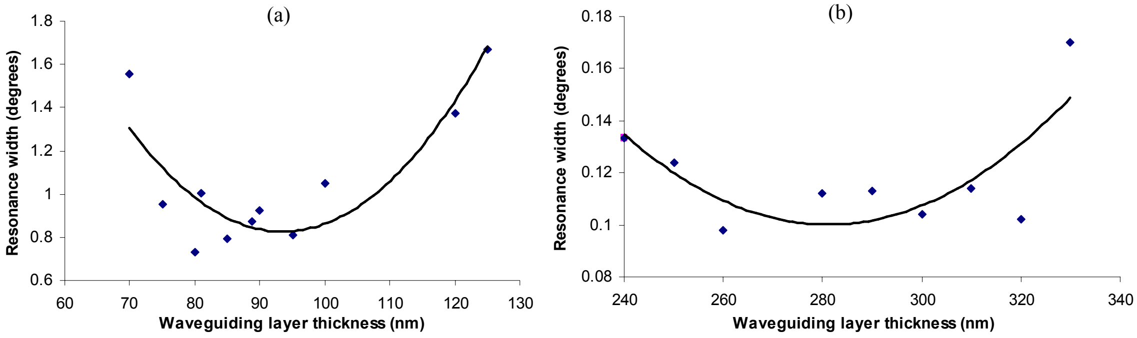

Figure 2.11. Optimization of porous silicon waveguiding layer thickness to achieve narrow waveguide resonance using (a) 633 nm and (b) 1550 nm light. The porous silicon is as-anodized.

The experimental conditions used to fabricate the optimized waveguide for 1550 nm light (e.g. narrowest resonance) are as follows. The silicon wafer was first cleaned with ethanol and DI water and then electrochemically etched. The etching conditions (current density and etching time) are given in Table 2.1. The top low porosity porous silicon layer was etched at 5 mA/cm^2 for 60 seconds and then the applied current density was changed to 48 mA/cm^2 for 53 seconds to form the bottom, high porosity porous silicon layer. A short regeneration period was introduced between the two currents in order to allow the HF concentration in the electrolyte to equilibrate throughout the pores, which inhibits the formation of porosity gradients at the interfaces [97]. After anodization, the sample was rinsed with ethanol and dried with nitrogen gas. We will refer to this p-type waveguide fabrication method as "method 1." Based on the porosity characterization curve given in Figure 2.1, the estimated porosities of the two porous silicon layers are 52% and 76%. Using the Bruggeman effective medium approximation, the layer indices are 2.08 and 1.41, respectively. A scanning electron microscopy (SEM) image of the fabricated, optimized waveguide is shown in Figure 2.12. The experimentally measured attenuated total reflectance spectrum (Metricon 2010 prism coupler, procedure given in Appendix C) of the porous silicon waveguide is shown in Figure 2.13 (a). The as-anodized porous silicon waveguide supports one guided mode (the sharper and deeper feature with FWHM ~0.07°) and one substrate mode (the broader feature). The envelope shape of the reflectance spectrum is due to the background reflection of the measurement system, which does not affect the resonance positions.

Table 2.1. Porous silicon waveguide (method 1) design parameters and fabrication conditions.

Layer	Current Density (mA/cm^2)	Porosity (%)	Bruggeman Refractive Index	Etching Time (seconds)	Thickness (nm)
Waveguiding Layer	5	52%	2.08	60	300 nm
Cladding Layer	48	76%	1.41	53	1330 nm

Given the nominal waveguide parameters shown in Table 2.1, the transfer matrix method (MATLAB code given in Appendix D) was used to simulate the attenuated total reflectance spectrum of the waveguide as shown in Figure 2.13 (b). Absorption and scattering losses of the porous silicon layers were neglected in the simulations. A resonance dip is observed because the high porosity cladding layer is not theoretically thick enough to prevent light leakage (experimental parameter of 1.3 μm is smaller than the theoretical minimum thickness of 2 μm required to prevent light leakage according to transfer matrix simulations); thus, all of the guided light is not coupled back out through the prism. Similar to the experimental measurement, there is one waveguide mode, the sharp and deep feature near 53˚; and one substrate mode (where light leaks into the cladding layer and the silicon substrate), the shallow and wide feature near 37˚. The application of this waveguide for sensing is given in Chapter 3.

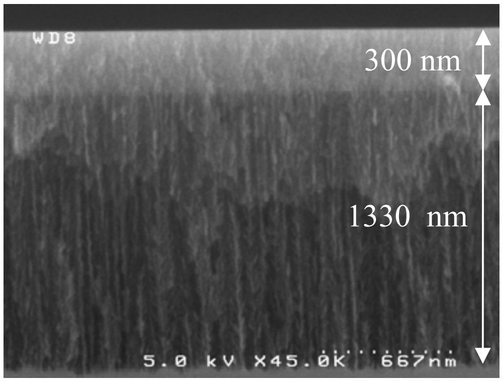

Figure 2.12. Cross-sectional SEM of porous silicon waveguide, showing the top low porosity layer of 300 nm and the bottom high porosity layer of 1330 nm.

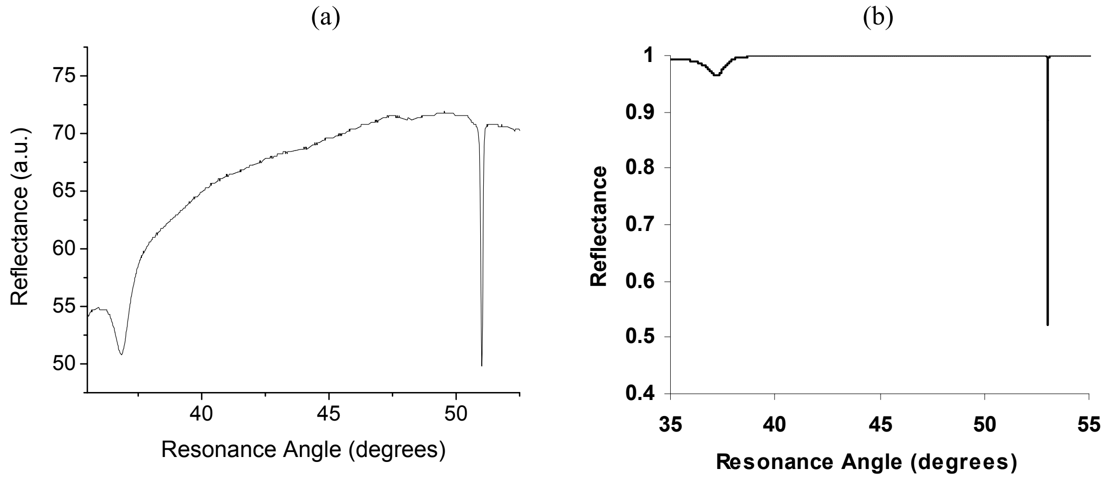

Figure 2.13. Experimental (a) and theoretical (b) attenuated total reflectance spectra, showing a waveguide mode near 53° and a substrate mode near 37°.

2.3 Revised porous silicon waveguide with larger pores

For some applications, it is helpful to widen the pores in order to allow easier infiltration of larger molecules. The following procedure describes a modified pre-anodization cleaning of the silicon wafer and a post-anodization chemical widening of the pores. This p-type waveguide fabrication method will be subsequently referred to as "method 2." Before anodization, the silicon wafer samples were first cleaned by rinsing with 15% HF solution. The samples were then oxidized at 800°C in ambient air (20% oxygen) for 30 minutes in an oven. The oxide formed was then removed by soaking the wafer in 15% HF for 1 minute, followed by ethanol rinsing. The waveguide structure was then etched, using the conditions specified in Table 2.2. Comparison with Table 2.1 shows that the top porous silicon layer had a higher porosity when the pre-anodization cleaning procedure was utilized. This higher porosity facilitates the pore initiation process. For the new porosity (and refractive index) of the top porous silicon layer, the waveguide thickness had to be optimized again. It was found that 240 nm was the optimum thickness for high quality waveguide resonances. After etching the waveguides, the samples were soaked in 1.5 mM KOH solution (1:5 of 9 mM aqueous KOH and ethanol) for 30 minutes to open up pores by 15-20 % [87] in order to ease the infiltration of molecules. Table 2.3 gives the porosity and Bruggeman effective refractive index for the two porous silicon layers after KOH soaking. As expected, the porosity increases and refractive index decreases for each layer. The measured attenuated total reflectance spectra after anodization and after KOH soaking are shown in Figure 2.14. The shift of the modes to smaller angles confirms the increased porosity of the layers, which results from the pore widening.

Table 2.2. Revised porous silicon waveguide (method 2) fabrication conditions.

Layer	Current Density (mA/cm^2)	Porosity (%)	Bruggeman Refractive Index	Etching Time (seconds)	Thicknes s (nm)
Waveguide Layer	5	55%	1.98	42	240 nm
Cladding Layer	48	76%	1.41	60	1500 nm

Table 2.3. Effective refractive index of porous silicon waveguide after KOH soaking.

Layer	Porosity (%)	Bruggeman Refractive Index	Thickness (nm)
Waveguiding Layer	62.4%	1.77	240 nm
Cladding Layer	80%	1.32	1500 nm

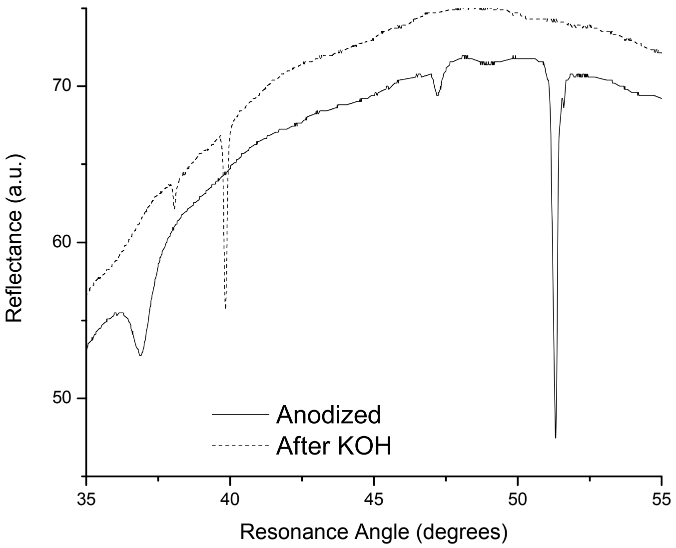

Figure 2.14. Reflectance spectrum of anodized porous silicon waveguide under revised condition in Table 2.2 (solid line) and after the anodized waveguide was exposed to 1.5 mM KOH for 30 minutes (dotted line). The one sharp-and-deep resonance is the guided mode, and the shallower and wider features are the substrate modes.

CHAPTER III

CHEMICAL AND BIOLOGICAL SENSING WITH P-TYPE POROUS SILICON WAVEGUIDE

3.1 Sensing of liquids of variable refractive index

Due to the small pore size of mesoporous silicon, typically 20-30 nm, much of the early research on porous silicon sensing was on chemical vapors and liquids. To check the capability of our p-type porous silicon waveguide sensor, we also carried out sensing of liquids of different refractive indices. The different liquids and their refractive indices are shown in Table 3.1. The index matching fluid is from Cargille Labs. Two of the liquids used are mixtures by different ratio of the index matching fluid with acetone.

Table 3.1. Different fluids and their refractive indices.

Liquids	Water	Acetone	1:3 by volume of index matching fluid and acetone	3:1 by volume of index matching fluid and acetone	Index matching fluid
Refractive index at 1550 nm	1.3150	1.3450	1.3975	1.5025	1.5550

Figure 3.1 shows the resonance shifts corresponding to the different liquids filling the pores of the porous silicon waveguide. The resonance shift has an approximately linear relationship with index change that occurs in the air gap, the low porosity porous silicon layer, and the high porosity porous silicon layer. The sensitivity of detection, which is the slope of the curve, is 19˚/RIU. Given that the Metricon prism coupler has an angular

resolution of 0.002°, this corresponds to a detection limit of 10^{-4} RIU, which is on the same scale as other work [88, 91].

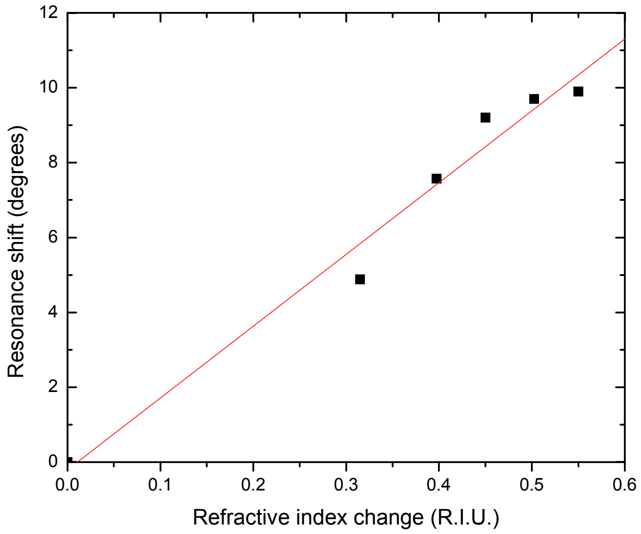

Figure 3.1. Porous silicon waveguide resonance shift upon exposure to water, acetone, and various mixtures of acetone and Cargille Labs refractive index matching fluid. A linear fit to the data is shown.

3.2 Field profile and biosensing: comparison with SPR

In this section, we describe the field profile of the waveguide mode to present a thorough discussion of the porous silicon waveguide sensing mechanism and its advantage over using a state-of-the-art SPR sensor for biomolecule detection. We first calculate the electric field distribution, confinement factor of the electric field interacting with biomolecules, and resonance width of both waveguide and SPR resonances. For convenience, we re-draw the porous silicon waveguide sensor together with SPR sensor. As shown in Figure 3.2 (a), the porous silicon waveguide consists of a low porosity layer

(52% porosity, n = 2.08, x = (-300 nm, 0 nm)), a high porosity layer (76% porosity, n = 1.41, x = (-1633 nm, -300 nm)), and an air gap (n = 1, x > 0 nm). As shown in Figure 3.2 (b), the SPR sensor consists of a gold film (x = (-40 nm, 0)) deposited onto a prism (x < -40 nm). Note that the mechanism of operation for the porous silicon waveguide and SPR sensors was discussed previously in Chapters 2 and 1, respectively.

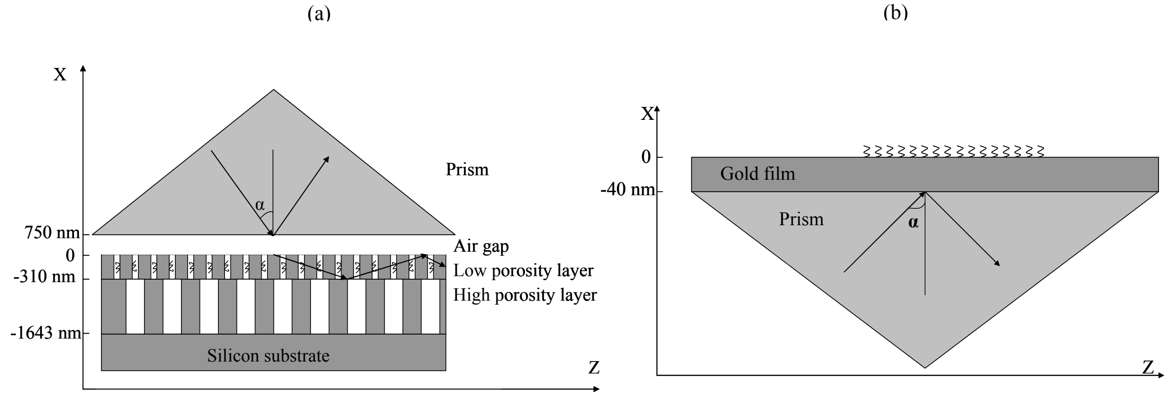

Figure 3.2. Schematic of sensor structure. (a) Porous silicon waveguide biosensor, consisting of a low porosity (high index) layer, a high porosity (low index) layer, and air gap. Total internal reflection enables waveguiding in the low porosity porous silicon layer. A prism is used to couple light into the waveguide mode through an evanescent wave. Biomolecules are infiltrated into the pores of the waveguide. (b) SPR biosensor consisting of a thin gold film on top of a prism. A surface plasmon is launched through an evanescent wave. Biomolecules are immobilized on top of the gold film.

For a quantitative comparison of the interaction strength between biomolecules and the electric field in the porous silicon waveguide and SPR sensor, we assume 1 watt of total power flows in the z-direction for both the waveguide mode and surface plasmon mode. For the SPR sensor, two wavelengths are considered: 633 nm and 1550 nm. For the porous silicon waveguide, only 1550 nm light is considered since silicon has significantly lower absorption losses in the infrared region. The field profile of the modes can be obtained by solving eigenmode equations for the TE waveguide mode (Appendix E) [26] and TM SPR mode (Appendix F) [98]. Figure 3.3 (a) shows the electric field profile of the porous silicon waveguide mode. The field amplitude is sinusoidal as a function of distance in the waveguiding layer and reaches its peak inside the layer. The field decays exponentially in the cladding layers. The two vertical lines delimit the waveguiding layer where we assume the biomolecules reside; the shaded area represents the primary region in which the electric field interacts with the immobilized biomolecules. Any biomolecules infiltrated into the lower cladding layer would further increase the interaction area. Figure 3.3 (b) shows the electric field profile for the surface plasmon mode. The field has its peak amplitude at the interface between the gold film and dielectric region (i.e., air or biomolecules) and decays exponentially away from the interface. The peak electric field amplitude is larger and the decay in the dielectric region is faster for 633 nm incident light compared to 1550 nm due to higher absorption losses in the infrared region. The two vertical lines in Figure 3.3 (b) delimit the region 4 nm above the gold surface, which is the region assumed to be occupied by biomolecules. The shaded area again represents the region in which the electric field interacts with the immobilized biomolecules. Due to the significantly larger surface area of the porous silicon waveguide and superior electric field confinement, the percent of modal power interacting with biomolecules in the waveguide is significantly larger than for the SPR sensor at either wavelength. A quantitative comparison is given next, through an example of small molecule detection.

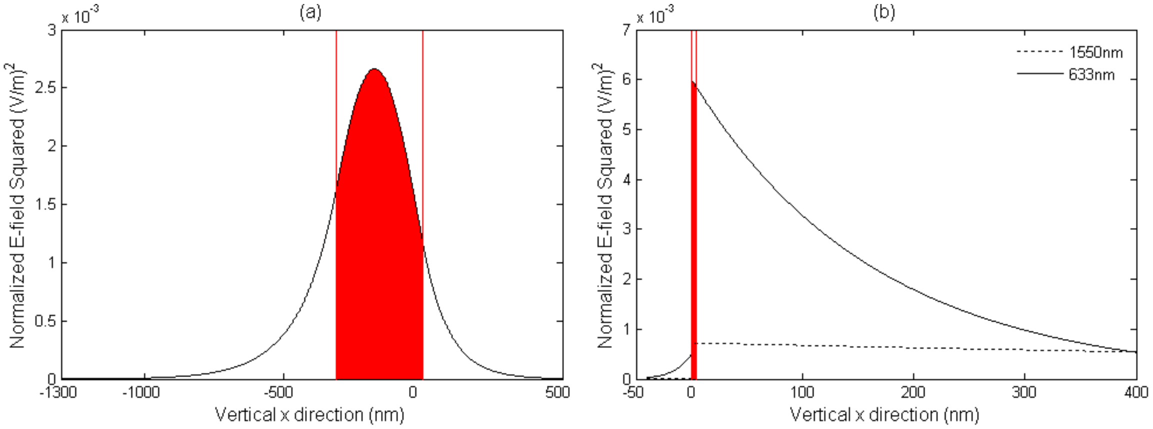

Figure 3.3. (a) E-field distribution for porous silicon waveguide. The waveguide region is between x = -300 nm and x = 0 nm as delimited by the two vertical bars. Above x = 0 is air; below x = -300 nm is the high porosity cladding layer. The shaded area is the power confined in the waveguiding layer where biomolecules are immobilized. (b) E-field distribution for SPR sensor. The gold film is between x = -40 nm and x = 0. Above x = 0 is air; below x = -40 nm is the prism. The vertical bars delimit the region where a 4 nm layer of biomolecules is immobilized. The shaded area is the power interacting with the biomolecules on the gold. Note that 1 watt of total power is assumed for both (a) and (b), and the x-axis scale for (a) is 4x larger than for (b).

The metric for sensitivity comparison between sensor platforms is given by the ratio of resonance shift to resonance width. With this performance metric, we compare the following: SPR sensor at 633 nm with a 4 nm biomolecule coating on the gold film, SPR sensor at 1550 nm with a 4 nm biomolecule coating on the gold film, porous silicon waveguide sensor at 1550 nm with a 4 nm biomolecule coating on the pore walls, and porous silicon waveguide sensor at 1550 nm exposed to the same number of biomolecules that coat the SPR sensor surface. For mathematical simplicity, the general case of a 4 nm coating of biomolecules is considered instead of assuming binding of a particular type of biomolecule, such as DNA or toxins, because the biomolecule spacing, which determines the number of immobilized molecules and, therefore, refractive index change, depends on the molecule size and shape [99], as well as the surface morphology

[100]. The resonance shifts for the porous silicon waveguide and SPR sensor are estimated from perturbation theory valid for a “small” perturbation, following reference [101]. A small perturbation is defined as a small dielectric change, for example due to the addition of a thin layer of biomolecules. If the effective index of the original mode is $N = \beta/(\omega/c)$ with β being the propagation constant of the mode, ω the angular frequency and c the speed of light in vacuum, then the new effective index is given by the following equation, after reference [101]:

$$N_{new} = N + \Delta N \cong N + \Delta(N^2)/(2N) \tag{3.1}$$

where

$$\Delta(N^2) = \begin{cases} \int_{-\infty}^{+\infty} \Delta\varepsilon(x) E_y^2 dx \Big/ \int_{-\infty}^{+\infty} E_y^2 dx, & \text{Waveguide} \\ \dfrac{(\frac{\omega}{c})^2 \int_{-\infty}^{+\infty} \Delta\varepsilon(x) \left\{ [\varepsilon(x)]^{-1} \dfrac{dH_y}{dx} \right\}^2 dx - N^2 \int_{-\infty}^{+\infty} \Delta\{[\varepsilon(x)]^{-1}\} H_y^2 dx}{\int_{-\infty}^{+\infty} [\varepsilon(x)]^{-1} H_y^2 dx}, & \text{SPR} \end{cases} \tag{3.2}$$

with $\varepsilon(x)$ being the dielectric constant as a function of x, E_y the transverse electric field of the TE waveguide mode, and H_y the transverse magnetic field of the TM SPR mode. Then the resonance shift can be found by matching the parallel component of the wave vector in different media:

$$\Delta\theta = \theta_{new} - \theta = \arcsin(N_{new}/n_{prism}) - \arcsin(N/n_{prism}) \tag{3.3}$$

where n_{prism} is the refractive index of the prism at the wavelength used. We assume a rutile prism with refractive index of 2.1252. Equations 3.1 to 3.3 indicate that the magnitude of the resonance shift is directly related to the interaction strength between the field and biomolecules. Therefore, as shown in Table 3.2, the porous silicon waveguide sensor with the 4 nm biomolecule coating experiences the largest resonance shift as the large internal surface area of the pores allows more biomolecules to interact with the electric field. When exposed to the same number of target biomolecules, the resonance shift for the SPR sensor at 633 nm is larger than that of the porous silicon waveguide. However, the sensitivity of the porous silicon waveguide sensor is superior to that of the SPR sensor due to the narrower resonance width of the waveguide mode, calculated from reference [92]. The losses for the SPR mode at 633 nm are substantially larger than for the SPR at 1550 nm or porous silicon waveguide at 1550 nm, leading to a wider resonance and compromised sensitivity. Consequently, for a given number of biomolecules, at least a 60-fold enhancement in sensitivity is expected for porous silicon waveguide sensors compared to SPR sensors. Moreover, when the entire surface area of the porous silicon waveguide sensors are utilized, there is an enormous increase in the electric field-biomolecule interaction strength, and hence resonance shift, due to the increased number of biomolecules present in the sensor. The surface area of the porous silicon waveguiding layer is more than 30 times that of SPR surface area, assuming 20 nm diameter pores. The resultant sensitivity enhancement, in this case, is more than 2000.

Table 3.2. Porous silicon (PSi) waveguide and SPR sensors comparison upon exposure to biomolecules (n = 1.46).

Simulation Description	SPR with 4 nm layer of biomolecules (λ = 633 nm)	SPR with 4 nm layer of biomolecules (λ = 1550 nm)	PSi WG with 4 nm layer of biomolecules on pore walls (λ = 1550 nm)	PSi WG with equal amount of biomolecules as coats SPR sensor (λ = 1550 nm)
% power interacting with biomolecules	1.18%	0.15%	11.32%	0.35%
Resonance shift	0.0971°	0.009°	1.67°	0.051°
Resonance FWHM	0.8°	0.05°	0.004°	0.004°
Shift/FWHM	0.1214	0.18	417.5	12.75

In order to compare the sensitivity of porous silicon waveguide sensors and SPR sensors at 1550 nm for arbitrary biomolecule size and spacing, calculations were performed for biomolecules of length 1-8 nm and with packing densities of 0-100%, where 100% packing means the spacing between adjacent biomolecules is just enough to accommodate its complementary species. The packing density thus determines the biomolecule spacing. As shown in Figure 3.4 (a, b), the longer the biomolecule and the tighter the packing, the larger the resonance shift, due to larger refractive index changes. The resonance shifts are calculated based on the method described previously and given by Equations 3.1-3.3. Figure 3.4 (c, d) shows the resulting porous silicon waveguide sensor enhancement compared to SPR sensors based on the ratio of the resonance shift to resonance width. Two cases are considered. First, in Figure 3.4 (c), it is assumed that biomolecules are immobilized throughout the porous silicon waveguide, taking advantage of the entire internal surface area. More than three orders of magnitude sensitivity enhancement is observed for the porous silicon waveguide sensor. In Figure 3.4 (d), it is assumed that an equivalent amount of biomolecules is exposed to both the porous silicon and SPR sensors. In this case, the sensitivity enhancement of the porous silicon waveguide is significantly more than an order of magnitude. It is also noted that porous silicon has the strongest advantage for small molecule detection. Smaller molecules give the porous silicon waveguide biosensor more performance enhancement over SPR sensors. It is well known that SPR sensors struggle to achieve low detection limits for small molecules [17, 18].

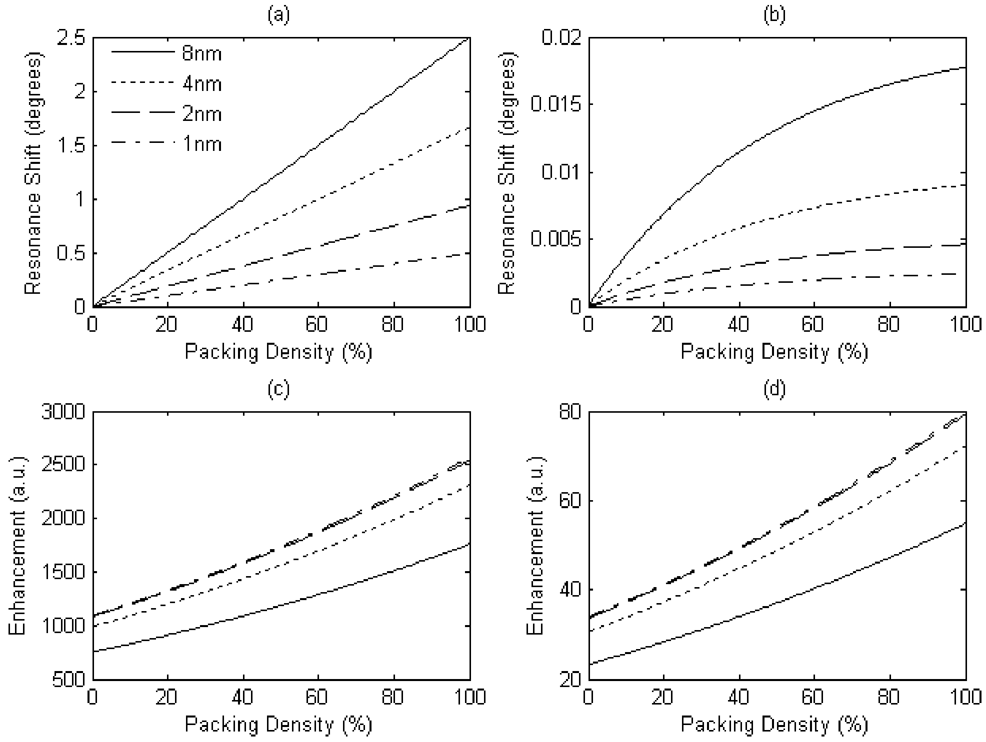

Figure 3.4. Resonance shift for (a) porous silicon waveguide and (b) SPR sensor at 1550 nm when exposed to biomolecules (n = 1.46) of different lengths and packing densities. Larger biomolecules that are packed tighter together will induce the largest refractive index change and largest resonance shift. Also shown is the performance enhancement (Shift/FWHM ratio) for the porous silicon waveguide sensor over the SPR sensor considering either (c) all of the porous silicon waveguide surface area is utilized or (d) the same amount of biomolecules are infiltrated into both the porous silicon waveguide and SPR sensors.

3.3 Sensing of DNA hybridization

3.3.1 Introduction to DNA

DNA oligonucleotides were used as the probe-target system to test the performance of the porous silicon waveguide biosensor. DNA (deoxyribonucleic acid) is made up of four nucleotide bases: A (Adenine), T (Thymine), C (Cytosine), and G (Guanine). The sequence of the bases carries the genome information of an organism. DNA can be single or double stranded. Double stranded DNA is formed when two complementary single stranded DNA bind with each other, or hybridize, to form a double-helix structure [102]. The binding is very specific. As shown in Figure 3.5 (a), A always associates with its complement T by two hydrogen bonds, and G always associates with its complement C by three hydrogen bonds. Figure 3.5 (b) shows two single stranded DNA that are not complementary to each other and thus cannot bind together. The backbone of the DNA strand is negatively charged which can be a problem for porous silicon biosensors. It has been reported that the binding of negatively charged molecules can accelerate corrosion of porous silicon and a proposed chemical reaction of the corrosion process has been described [103]. In sections 3.3.3 and 4.5.2, we will discuss our observation of the corrosion problem and our attempts to solve it.

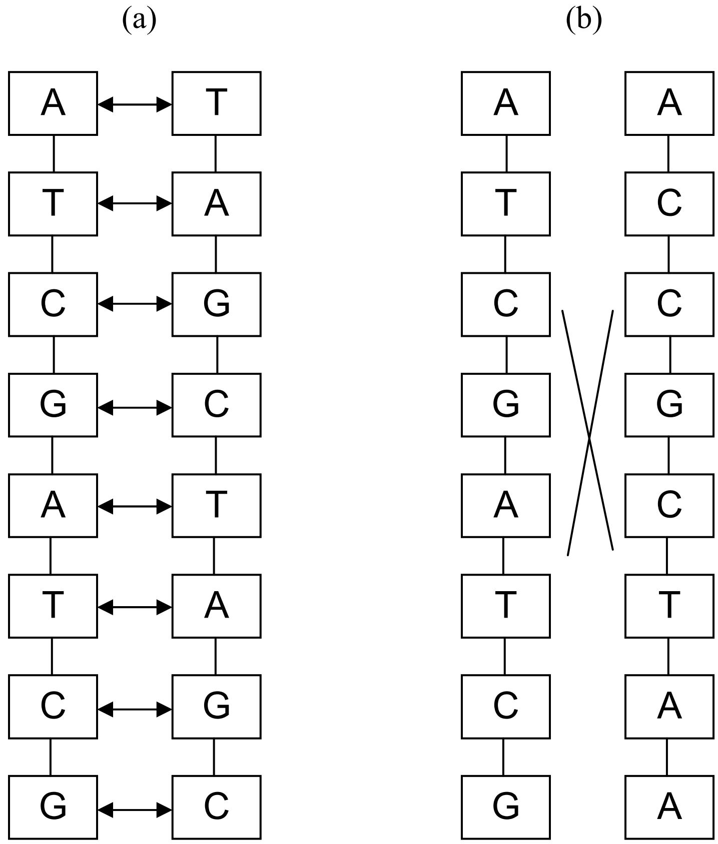

Figure 3.5. (a) Double stranded DNA formed by specific binding. (b) Two non-complementary DNA single strands will not bind together.

The hybridization, or binding of two single stranded DNA depends on factors such as ionic strength, temperature, GC content (percentage of G and C bases), and DNA length. Higher ionic strength of the solution will screen the negative charges of the DNA backbone and help the complementary DNA strands approach each other. The melting temperature of double stranded DNA is the temperature at which approximately 50% of the double strands separate into single strands. DNA hybridization experiments therefore take place below this temperature. The lower the hybridization temperature compared to the melting temperature, the more likely hybridization will take place. The melting temperature of double stranded DNA depends on DNA length and GC content. Longer

DNA has stronger binding energy and thus a higher melting temperature. Since G↔C has three hydrogen bonds, as opposed to A↔T with two hydrogen bonds, higher GC content leads to a higher melting temperature. In our experiments, DNA hybridization was carried out at room temperature.

To detect DNA, the porous silicon waveguide must be functionalized, that is, to have probe DNA attached to the porous silicon first, which can then capture the target DNA to be detected. This functionalization process involves multiple steps of chemically linking biomolecules. Two kinds of cross-linkers will be described: glutaraldehyde and sulfo-SMCC (Sulfosuccinimidyl 4-[N-maleimidomethyl]cyclohexane-1-carboxylate). In the following section, we start with glutaraldehyde for DNA cross-linking. In section 3.5, a detailed comparison of the two cross-liners is provided.

3.3.2 DNA hybridization detection experiments

In this section, the use of standard silane and glutaraldehyde chemistry is discussed for the attachment of probe DNA to porous silicon [104]. Glutaraldehyde is homo-bifunctional cross-linker, meaning that it can react with the same chemical groups at both ends, in this case amine groups. The step-by-step reaction scheme is shown in Figure 3.6.

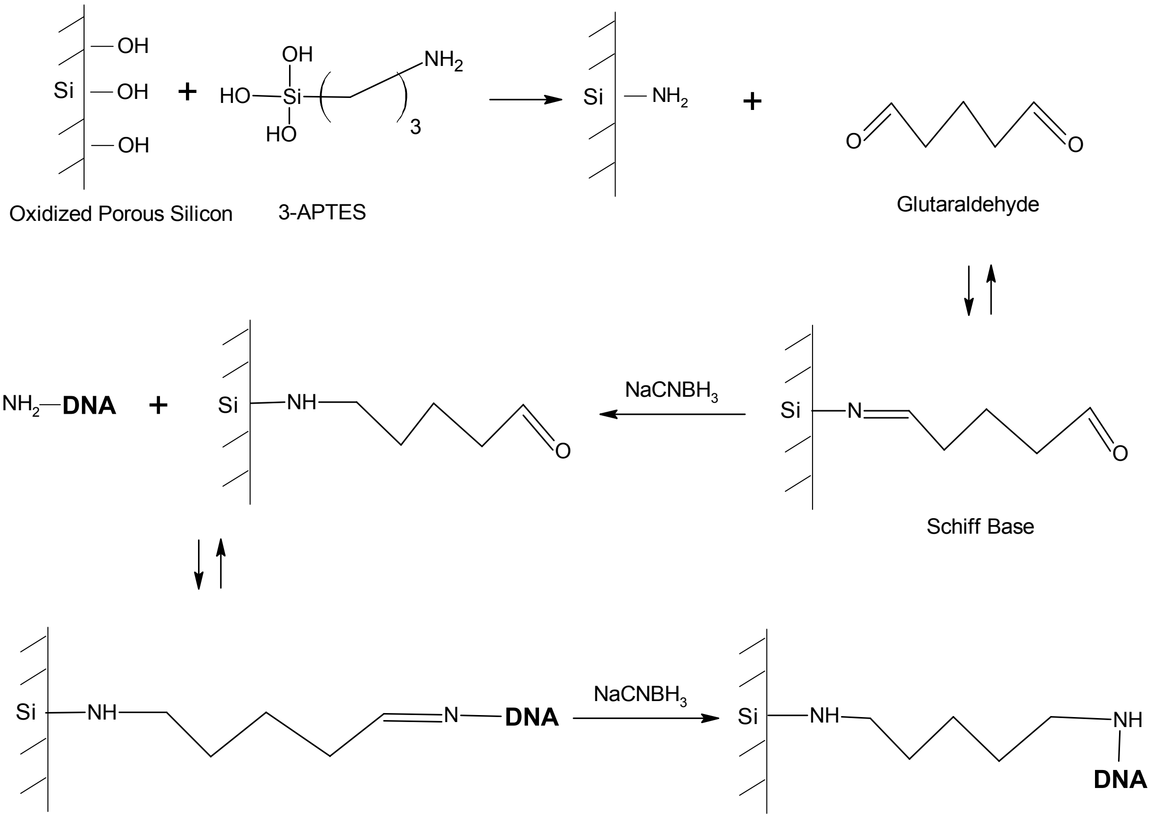

Figure 3.6. Step-by-step reaction of cross-linking probe DNA to porous silicon by glutaraldehyde. The oxidized porous silicon sample was first silanized with 3-APTES. The amine derivatized sample was then cross-linked to amine modified probe DNA with glutaraldehyde, generating unstable intermediate Schiff base (C=N). The Schiff base can be stabilized by sodium cyanoborohydride.

After anodization under the conditions given in Table 2.1 (method 1), the porous silicon waveguide was oxidized at 900˚C for 10 minutes in order to lower the waveguide loss [105] and to prepare the surface for subsequent chemical functionalization. A 3-zone tube furnace (Lindberg Blue tube with Eurotherm controller) was first heated from room temperature to 900˚C in argon atmosphere. It was then switched to oxygen with a flow rate of 1 liter per minute. The waveguide samples were delivered to the central zone by a quartz boat in a process of 1 minute. The samples remained there for 8 minutes before being pulled out in another process of 1 minute.

The first step in the chemical functionalization is the addition of 3-aminopropyltriethoxysilane (3-APTES) to derivatize the oxidized porous silicon with amine groups. In order to determine the optimal 3-APTES concentration, 100 μL of different concentrations of 3-APTES were spotted onto oxidized porous silicon waveguide samples. The resulting angular resonance shifts are shown in Figure 3.7. As seen from the figure, the porous silicon waveguide sensor distinguishes between the different concentrations. Saturation occurs at 4% 3-APTES concentration, which suggests a monolayer coating of 3-APTES is formed on the pore walls. This is consistent with previous reports on biosensing using porous silicon microcavities [37]. Hence, 4% 3-APTES solution is used as the first step of functionalization in all of the following experiments.

The recipe for the silanization is as follows: 40 μL of 3-aminopropyltriethoxysilane (99% 3-APTES, Aldrich) was mixed with 500 μL of DI water and 480 μL of methanol. Then, 100 μL of the resulting 4% silane solution was spotted onto the porous silicon waveguide to completely cover the surface area of porous silicon ($\pi \times (0.8\ \text{cm})^2 = 2\ \text{cm}^2$), and incubated in a humid environment for 20 minutes (procedure given in Appendix G). The samples were then rinsed vigorously with DI water, dried with nitrogen gas, and baked at 100˚C for 10 minutes.

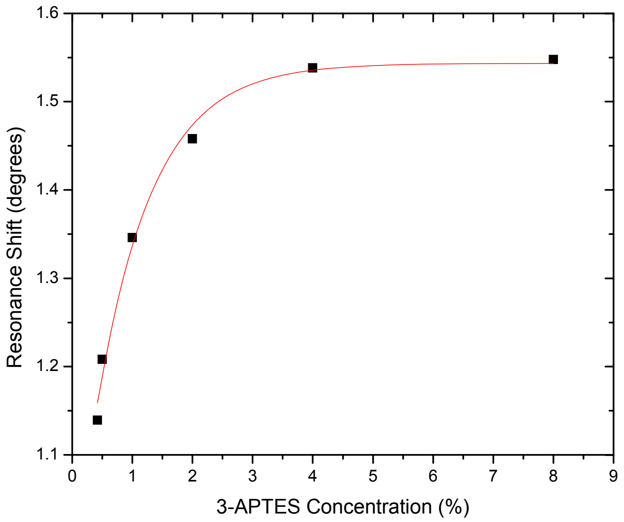

Figure 3.7. Porous silicon waveguide (method 1) resonance shift due to exposure to 100 μL of different concentrations of 3-APTES coating the oxidized pore walls. Near 4% APTES, the shift saturates, suggesting monolayer coating.

The next step of the functionalization procedure was the addition of the cross-linker glutaraldehyde, with the following procedure: 50 μL of 50% photographic grade glutaraldehyde (Sigma) was mixed with 950 μL of HEPES buffer (20 mM HEPES, 150 mM NaCl, 5 mM EDTA, pH=7.4). Then, 100 μL of the resulting 2.5% glutaraldehyde solution was dropped onto the porous silicon waveguide. In order to stabilize the Schiff base (C=N) formed during reaction of the aldehyde group with the amine group, 1 μL of sodium cyanoborohydride solution (5M cyanoborohydride, 1M NaOH, Aldrich) was added to the porous silicon. After 2 hours of incubation, the porous silicon waveguide was rinsed with buffer and then soaked in buffer for 1 hour, followed by an additional buffer rinse to remove unreacted glutaraldehyde from the pores. Then the sample was dried with N_2. The later four steps, namely, rinsing with buffer, soaking in buffer, additional rinsing with buffer, and drying with N_2 will be collectively noted as "post-process cleaning."

DNA cross-linking was initiated within 30 minutes of drying because the functionality of glutaraldehyde degrades upon long-time exposure to air. The DNA oligos used in the hybridization experiments were purchased from MWG Biotech, with HPLC purification. The 24-base sequences (melting temperature of 62.7°) are given below:

probe DNA, 5'-TAGC TATG GAAT TCCT CGTA GGCC-3';

complementary anti-sense, 5'-GGCC TACG AGGA ATTC CATA GCTA-3';

non-complementary mismatch, 5'-AGCT AGCT AGCT CATG ATGC TGTC-3'.

A 100 μM concentration of amino-modified probe DNA oligos in buffer was applied to the porous silicon waveguide and incubated for 2 hours (Schiff base stabilized by adding 1 μL of 5 M sodium cyanoborohydride per 100 μL of DNA solution), followed by post-process cleaning.

To close any unreacted aldehyde groups for minimizing non-specific binding, 3M ethanolamine (>99% ethanolamine hydrochloride, Aldrich) in buffer, with pH adjusted to 9.0, was dropped onto the porous silicon waveguide and soaked for 2 hours (sodium cyanoborohydride again used for Schiff base stabilization), followed by post-process cleaning.

After immobilizing probe DNA onto porous silicon, the porous silicon waveguide sensor is fully functionalized and ready for testing. Complementary DNA solutions in buffer at different concentrations, non-complementary DNA in buffer, as well as buffer solution alone, were spotted separately onto porous silicon waveguide samples and incubated at room temperature in a humid environment for 1 hour. Afterwards, all samples were rinsed with buffer, soaked in buffer for 20 minutes, rinsed again vigorously with buffer to remove any remaining non-bounded species from the pores, and dried with N_2. It is noted that the porous silicon waveguides exposed to non-complementary DNA and buffer solution alone were prepared for control experiments to demonstrate sensor selectivity.

Figure 3.8 shows the waveguide resonance after each functionalization step, from left to right: after oxidation, after silanization, and after glutaraldehyde+probe DNA+ethanolamine. The later 3 steps are combined together because of the instability of glutaraldehyde in air. The amplitude change is attributed to different gain values of the prism coupler detector used for each measurement and has no effect on the absolute position of the resonance angle. The resonance shifts suggest that the functionalization was carried out successfully, and this was confirmed when complementary DNA binding was observed. Figure 3.9 demonstrates the detection of DNA in the porous silicon waveguide. The waveguide resonance shifts about 0.046° after the porous silicon waveguide was exposed to 50 μM of complementary DNA. Figures 3.10 and 3.11 show the resonance after exposure to 50 μM non-complementary DNA and after exposure to buffer solution, respectively, with negligible shift. Hence, the porous silicon waveguide sensor is able to discriminate between complementary DNA and non-complementary DNA.

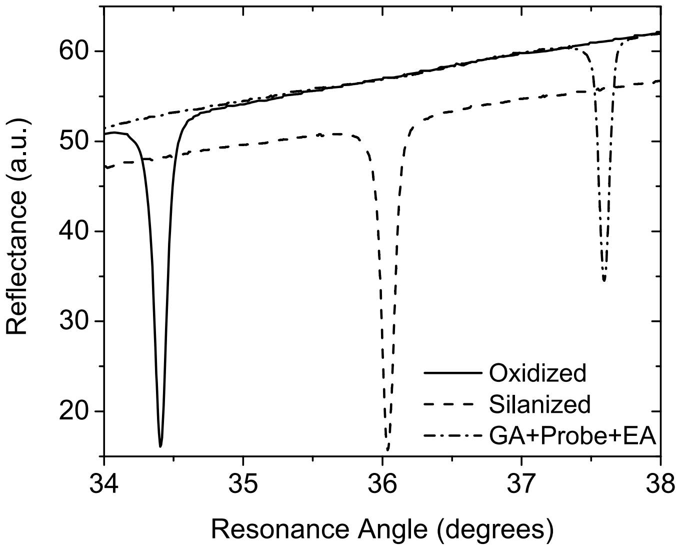

Figure 3.8. Porous silicon waveguide resonance after each functionalization step: after oxidation (Oxidized), after 3-APTES (Silanized), and after glutaraldehyde+probe DNA+ethanolamine (GA+Probe+EA).

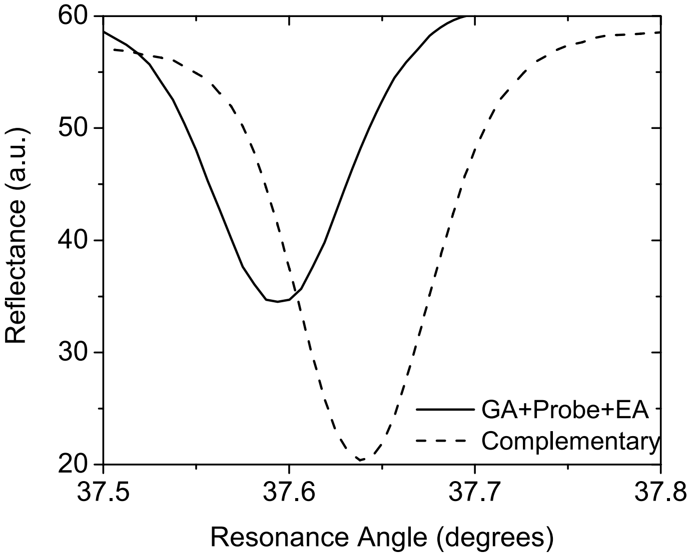

Figure 3.9. Porous silicon waveguide resonance shift for complementary DNA (Anti-sense), demonstrating the recognition of DNA binding inside the porous silicon waveguide.

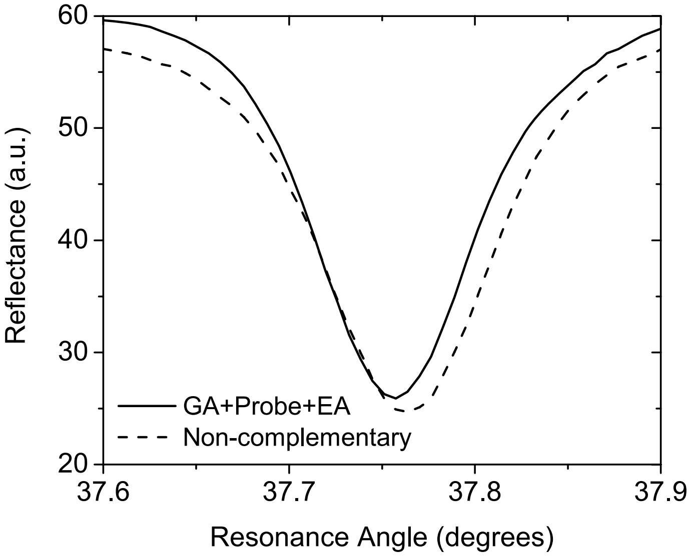

Figure 3.10. Negligible porous silicon waveguide resonance shift for non-complementary DNA (Mismatch), demonstrating that the porous silicon waveguide can distinguish complementary and non-complementary DNA sequences.

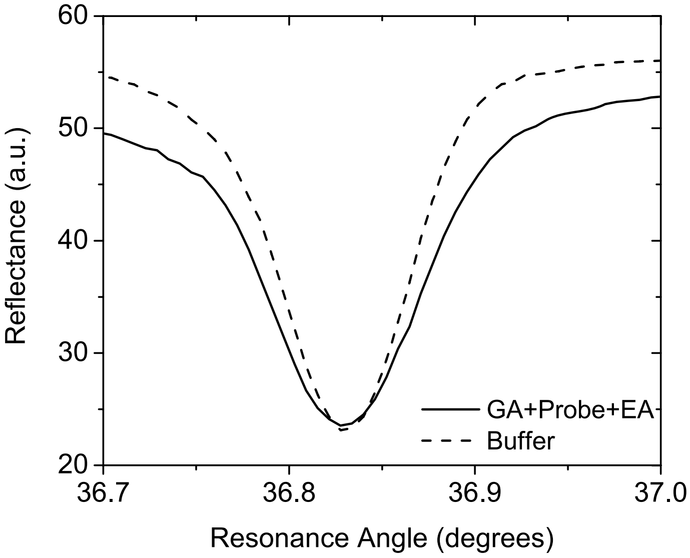

Figure 3.11. No resonance shift observed upon exposure of the porous silicon waveguide to buffer solution, demonstrating the stability of the sensor against false positives.

3.3.3 Analysis of the experimental results

The magnitude of the resonance shift quantifies the complementary DNA concentration with larger shifts indicating higher DNA concentrations. Since the angular resolution of the prism coupler is 0.002° and the FWHM of the porous silicon waveguide resonance is 0.07°, we expect the ultimate detection limit is much smaller than 50 μM. In order to estimate the detection limit of the porous silicon waveguide for 24-base DNA using silane-glutaraldehyde chemistry, the following calculation was performed. Using the Bruggeman effective medium theory and assuming the pore refractive index is a linearly weighted average of air and DNA by volume, the refractive index of the top 300 nm porous silicon layer with 20 nm pores and 52% porosity can be calculated for arbitrary DNA molecular coverage on the pore walls. We assume a DNA refractive index of 1.5 [106] and length of 2.2 Å per base [107]. With the refractive index of the porous silicon with DNA inside calculated, the wavevector of the waveguide mode can be obtained, and the angle at which light is coupled into the waveguide can be deduced [26], as described in section 2.2. Figure 3.12 shows the simulated resonance shift for 24-base DNA detection at different complementary DNA coverage, where 100% coverage corresponds to double strand DNA density of $4\times10^{13}/\mathrm{cm}^2$ (the probe DNA density is fixed at $4\times10^{13}/\mathrm{cm}^2$, resulting in a probe-to-probe distance just large enough to accommodate the binding of the complementary DNA strand) [99]. The corresponding concentration in μM can be calculated, given that 100 μL volume of solution was used to completely cover the porous silicon waveguide (surface area of pores 64 cm^2), and is shown as another x-axis on the top. The detection limit is found by checking the coverage corresponding to a resonance shift of 0.002° (the angular resolution of the prism coupler), which is 0.08% or

50 nM. Given the 7k Dalton molecular weight for DNA, the detection limit is equivalent to 5 pg/mm^2. For non-complementary DNA (Mismatch), experiments have shown that the magnitude of the resonance shift also corresponds to the DNA concentration. While in Figure 3.10 the shift for 50 μM mismatch DNA is about 0.004°, at 50 nM mismatch concentration, the shift will be much smaller and hence selective detection at these low concentrations is possible.

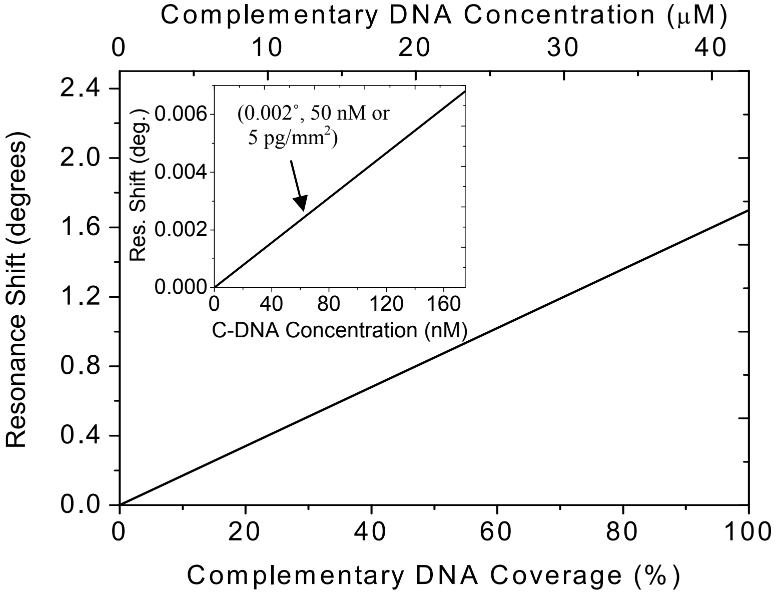

Figure 3.12. Simulated resonance shift for different coverages on pore walls by 24-base target DNA, with the top x-axis showing the corresponding target DNA concentration in μM. The inset shows the zoom-in view at low DNA concentration. The point (0.002 degrees, 50 nM or 5 pg/mm^2) corresponds to the detection limit.

Figure 3.13 shows the simulated resonance shift for 24-base complementary DNA at different probe and complementary DNA coverages. The bottom *x*-axis indicates the percent of probe DNA hybridized by complimentary DNA and the top *x*-axis gives the complimentary DNA concentration needed for each corresponding percent probe hybridization, given that 100 μL of solution was used to completely cover the 2 cm^2 porous silicon waveguide active area. As expected, the resonance shift after exposing the porous silicon waveguide to a given concentration of complementary DNA increases in accordance with the probe coverage in the waveguide. The effective index of the waveguide mode, and hence the confinement of the electric field inside the waveguide, increases for larger probe coverage; the stronger field makes the waveguide more sensitive to small changes in refractive index from DNA hybridization. The inset of Figure 3.13 shows the detection limit of the porous silicon waveguide biosensor for different probe DNA coverage. As the probe coverage increases, the detection limit decreases due to the lesser available binding sites for complementary DNA.

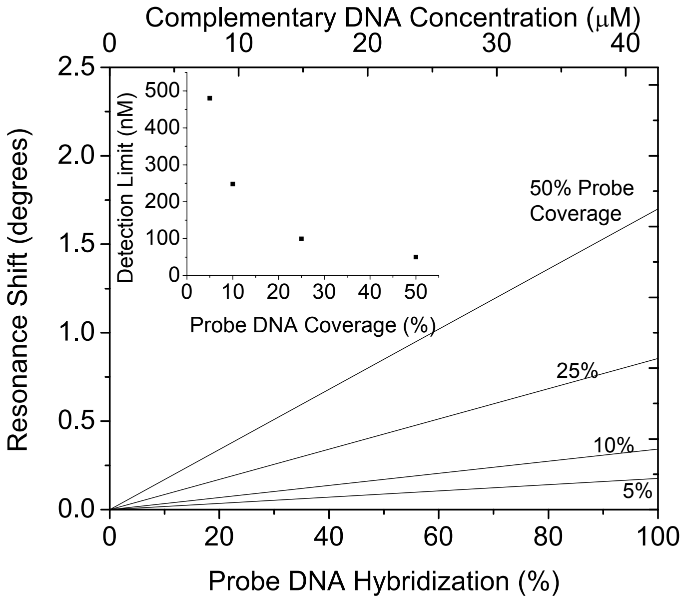

Figure 3.13. Simulated porous silicon waveguide resonance shift as a function of probe DNA hybridization percentage (bottom *x*-axis) and corresponding complementary DNA concentration (top *x*-axis), given for different probe DNA coverage on the pore walls. Larger resonance shifts occur for larger probe coverage and when a greater fraction of the probe molecules are hybridized. The inset shows the detection limit at different probe DNA coverage. At the optimal probe coverage of 50% (i.e., leaving just enough space for complementary DNA attachment), the detection limit is 50 nM.

Based on the comparison of our experimental results with the simulations, it appears that there is low probe DNA coverage and hybridization efficiency inside the porous silicon. However, we can definitively state that hybridization is taking place inside the pores, and not simply on the surface of the porous silicon waveguide. Even if we assume an optimal 50% probe coverage on the surface and 100% hybridization efficiency (which is not realistic), the weak evanescent field of the waveguide mode interacting with DNA on the surface would lead to a 0.04° resonance shift, which is smaller than our experimentally measured value. In the experiments, several factors likely contribute to the lower than expected probe coverage and hybridization efficiency. First, some DNA molecules may infiltrate into the lower porous silicon layer, whereas in simulation, it is assumed that all DNA molecules infiltrate only into the low porosity, or waveguiding layer. Since the electromagnetic field magnitude in the high porosity or the lower cladding layer is very small compared to the top, low porosity porous silicon layer, DNA attachment in the high porosity layer does not induce as large an effective refractive index change as DNA attached in the low porosity waveguide layer. Second, the silane-glutaraldehyde functionalization protocol relies on an unstable Schiff base that can compromise probe immobilization, and it is likely that only partial hybridization is taking place inside the pores. Alternative cross-linking protocols that do not rely on the formation of Schiff bases [104] are described in the next section to increase probe coverage. Third, as described in detail in Chapter 5, it is likely that 24-base DNA is too large to easily infiltrate into the pores. The use of smaller DNA strands improves the DNA diffusion into the pores, which as shown in Figure 3.13 leads to improved hybridization efficiency and detection sensitivity. In addition to non-optimal probe coverage and hybridization efficiency, there are other factors that are likely compromising the porous silicon waveguide sensor sensitivity. As mentioned in section 3.3.1, DNA molecules are negatively charged and porous silicon corrosion due to interaction with DNA molecules causes a decrease in refractive index that reduces the magnitude of the resonance shift upon DNA hybridization [103]. The incorporation of Mg^{2+} into buffer solution was suggested to inhibit the corrosion process [103]. However, we have conducted experiments and could not verify this process. In Chapter 4, we report on the use of n-type porous silicon waveguides for DNA detection to solve this problem.

3.4 Alternative functionalization biochemistry

3.4.1 Functionalization with sulfo-SMCC

In order to avoid the instability problem of the Schiff base generated during functionalization with glutaraldehyde, an alternative and larger cross-linker, sulfo-SMCC (Pierce), can be used to link probe DNA to porous silicon without relying on unstable C=N double bonds. Sulfo-SMCC is a hetero-bifunctional cross-linker, meaning that it can react with two different chemical groups at its two ends. The procedure is similar to the one using the homo-bifunctional cross-linker, glutaraldehyde. The as-anodized porous silicon waveguide (method 2) samples fabricated under the etching conditions given in Table 2.2, were soaked in KOH to enlarge the pores (Table 2.3), and then oxidized at 800°C in ambient air (20% oxygen) for 30 minutes. For this waveguide structure, the waveguide resonance shifts due to 100 μL of 3-APTES with different concentrations are shown in Figure 3.14. At 4%, the shift is also saturated. The maximum shift is smaller than shown in Figure 3.7 since after KOH soaking, the pores are larger and their surface area is smaller. The silanized samples were spotted with 2 mg/ml sulfo-SMCC in HEPES buffer and incubated for 2 hours, followed by post-process cleaning. The samples were then rinsed by DI water to remove the remaining salts inside the pores. The resonance spectra after oxidation, after silanization, and after sulfo-SMCC attachment are shown in Figure 3.15. The step-by-step reactions illustrating the silane-sulfo-SMCC attachment chemistry are shown in Figure 3.16.

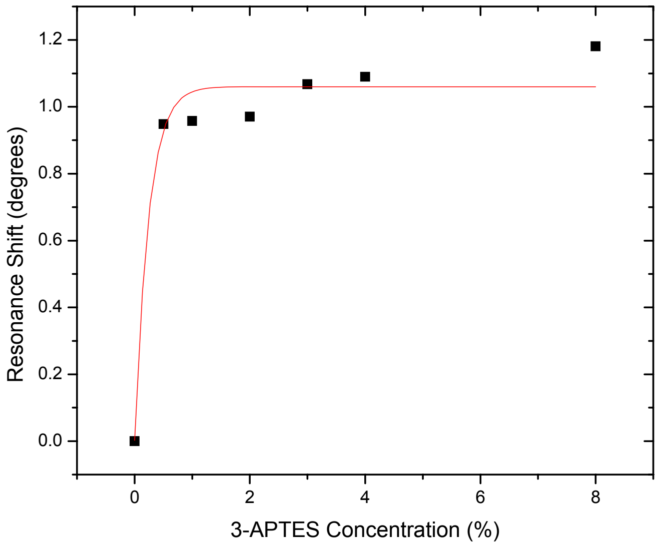

Figure 3.14. Revised porous silicon waveguide (method 2) resonance shift due to 100 μL of different concentrations of 3-APTES coating the oxidized pore walls.

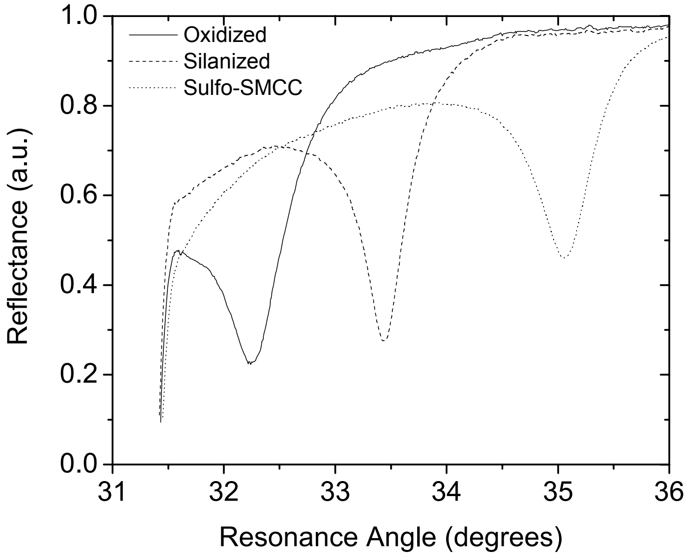

Figure 3.15. Resonance spectra of porous silicon waveguide (method 2) after oxidation, silanization, and sulfo-SMCC derivatization.

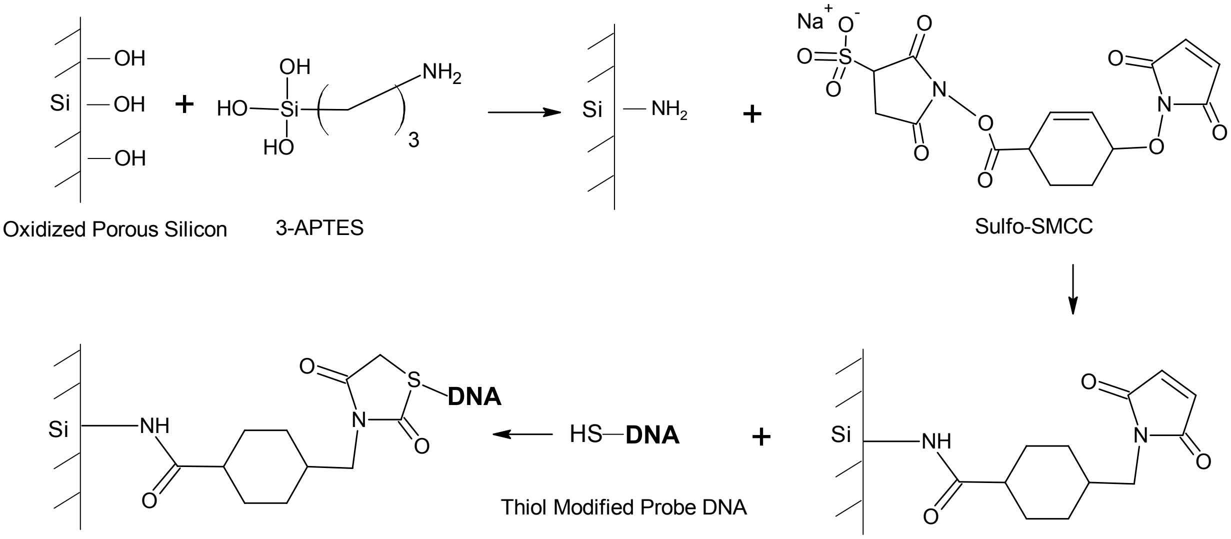

Figure 3.16. Step-by-step reaction of cross-linking probe DNA to porous silicon by sulfo-SMCC. The oxidized porous silicon sample was first silanized with 3-APTES. The amine derivatized sample was then cross-linked to thiol-modified probe DNA with sulfo-SMCC.

3.4.2 Probe DNA attachment

Figure 3.16 shows that probe DNA can be cross-linked to the maleimide activated porous silicon through the covalent bond between thiol modifiers of probe DNA and the maleimide groups of sulfo-SMCC. We note that the as-received DNA oligos were disulfide (-S-S) terminated instead of thiol terminated, due to the superior long term stability of disulfide. Immediately before cross-linking was carried out, the reducing agent tris(2-carboxy-ethyl)phosphine (TCEP) was used to change the disulfide groups to thiol groups. A 1:1 mixture by volume of 200 μM DNA in buffer and 200 μM TCEP (Pierce) in buffer was prepared and the resulting solution stayed for 30 minutes to allow full reduction of the disulfide groups. The resulting 100 μM DNA with reduced thiol modifiers was then ready for attachment to the maleimide activated porous silicon waveguide. Lower concentrations, such as 50 μM and 25 μM, were obtained by diluting the 100 μM DNA solution. In order to demonstrate the functionality of the sulfo-SMCC for DNA attachment, 100 μL of 100 μM 8-base DNA (GGGG-GGGG) was dropped onto a maleimide activated porous silicon waveguide sample and incubated for 1 hour, followed by a 20 minute soak in buffer, rinsing with DI water, and drying with nitrogen. Attachment of the 8-base probe DNA was confirmed by prism coupler measurements, which showed a resonance shift of 0.22°. Control experiments confirmed no attachment in porous silicon from TCEP alone at the concentrations used for the experiments.

3.5 Choosing the cross-linker: glutaraldehyde vs. sulfo-SMCC

Two cross-linkers, glutaraldehyde (homo-bifunctional) and sulfo-SMCC (hetero-bifunctional) have been used for probe DNA attachment to the silanized porous silicon waveguide samples. A comparison of these two cross-linkers is provided in the following sections to help determine which one to choose for functionalization of the porous silicon waveguide.

3.5.1 Glutaraldehyde (homo-bifunctional)

Advantages: (1) Glutaraldehyde is a smaller molecule (0.8 nm) than sulfo-SMCC (1.9 nm), resulting in a larger number of probe DNA molecules immobilized in the pores. Also, it forms a thinner monolayer inside pores and leaves larger space for DNA immobilization. (2) The amine ($-NH_2$) group on DNA is more stable than the thiol (-SH) group on DNA in buffer solution, so there is longer available time to resuspend (dissolve) lyophilized (dried) DNA molecules in buffer solution and mix the solution well. (3) The solution of glutaraldehyde in buffer is stable, and is usable within one day (glutaraldehyde derivatized porous silicon samples must be used within 30 minutes after drying since the aldehyde group is unstable in air). (4) The amine modifiers of probe DNA can be used after DNA resuspension directly without any reducing procedure, and it is very stable in solution.

Disadvantages: (1) Glutaraldehyde reacts with amine groups to form Schiff bases; the carbon-nitrogen double bonds are unstable and can decompose. Linkage of glutaraldehyde to silane and amine modified DNA to glutaraldehyde are both based on this reaction. If the Schiff base decomposes at any stage, the linking is broken. Schiff bases can be stabilized by sodium cyanoborohydride or borohydride. The first stabilizer is weaker. The second one is stronger but compromises the reactivity of glutaraldehyde. Porous silicon waveguides functionalized with glutaraldehyde and probe DNA show significant resonance shifts as a function of time, implying the instability of the functionalized biosensor. (2) The attachment of DNA by glutaraldehyde is less reproducible than by sulfo-SMCC; therefore, the yield of porous silicon waveguide biosensors functionalized with glutaraldehyde is less than that of sulfo-SMCC functionalized porous silicon waveguide biosensors. (4) As a homo-bifunctional cross-linker, glutaraldehyde can form bridge structures on the pore walls. In this case, both ends of the linker attach to the 3-APTES instead of one end attaching to 3-APTES and the other end binding to probe DNA.

3.5.2 Sulfo-SMCC (hetero-bifunctional)

Advantages: (1) The reactions of sulfo-SMCC with amine groups (of 3-APTES) and thiol groups (of DNA) are stable and direct, with no unstable intermediate product involved. Porous silicon waveguides functionalized with probe DNA by silane-sulfo-SMCC chemistry showed negligible shifts as a function of incubation time in buffer, demonstrating the stability of the functionalized biosensor. (2) The attachment of DNA is more reproducible, and, therefore, the yield of sulfo-SMCC functionalized porous silicon waveguide biosensor is higher than when glutaraldehyde was used. (3) As a hetero-bifunctional cross-linker, sulfo-SMCC does not form bridge structures or self-conjugate.

Disadvantages: (1) Sulfo-SMCC is twice the size of glutaraldehyde, about 1.9 nm, compared to 0.8 nm for glutaraldehyde. The resulting probe DNA density on the pore walls is smaller. Experiments show the saturated resonance shift for 16-mer probe DNA linked by glutaraldehyde to be 0.7°, and by sulfo-SMCC to be 0.38°. The larger size of SMCC also means that less space is left for DNA immobilization. (2) Sulfo-SMCC is not stable in buffer. Since the NHS-ester group of sulfo-SMCC tends to hydrolyze in water, the solution needs to be used immediately after mixing (sulfo-SMCC derivatized samples are stable and can be stored at room temperature in dry environment for days due to the stability of the maleimide group). (3) Thiol modifiers have to be reduced first before cross-linking with maleimide functionalized porous silicon, and the thiol modified DNA must be used immediately after reduction since the thiol groups are not stable in solution. (4) The solubility of sulfo-SMCC is 2.5 mg/ml. In experiments, this concentration was used; higher concentration is not possible due to the solubility limit.

Given the stability and reproducibility of the sulfo-SMCC cross-linking, sulfo-SMCC is preferred to functionalize the porous silicon waveguides for DNA detection. In Chapter 4, we use sulfo-SMCC for DNA detection with the n-type porous silicon membrane waveguide biosensor. And in Chapter 5, sulfo-SMCC is used for experiments that characterize the effect of biomolecular size on the sensitivity of detection of porous silicon waveguide biosensors.

CHAPTER IV

POROUS SILICON FREE-STANDING MEMBRANE WAVEGUIDE

4.1 Motivation and design

The p-type porous silicon waveguide discussed in Chapters 2 and 3 does not have sufficiently large pores to enable the detection of biomolecules such as proteins and viruses, which have sizes of a few tens of nanometers. It is desirable, therefore, to design a porous silicon waveguide with larger pores so that these biomaterials of interests can be detected. However, there is an upper limit to the size of the pores: if the pores are so large as to approach the wavelength of incident light, effective medium theory is no longer valid, scattering losses dominate, and a waveguide mode resonance will not be observed. N-type porous silicon with pores in the size range of 30-100 nm has been reported [36] and will be discussed in this chapter for the application of larger molecule sensing. A cross-sectional SEM image of a typical n-type porous silicon layer with 100 nm diameter pores is shown in Figure 4.1.

In addition to modification of the porous silicon pore size, modification of the sensor design is also considered here for a more robust sensing system and direct integration into existing commercial measurement instruments. As reported in chapters 2 and 3, the p-type porous silicon waveguide in the Otto configuration relies on maintaining a uniform submicron air gap, which is not amenable to microfluidics integration for real-time biomolecular interaction analysis. In the Kretschmann configuration, as used in SPR systems (see Figure 2.7), light is coupled from the back side of the device and a microfluidic cell can be integrated into the system at the top. As discussed in section 2.2, it is not possible to excite a waveguide mode through the back side of the porous silicon waveguide (i.e., silicon substrate). Therefore, in order to realize the Kretschmann configuration, the porous silicon substrate must be removed. Porous silicon free-standing thin films have been previously demonstrated [108] and there are several reported applications of the lift-off porous silicon films, including chemical and gas sensing [109, 110], solar cells [111], optical devices [112], and microchannels [113]. In this chapter, we report a label-free n-type porous silicon membrane waveguide biosensor in the Kretschmann configuration where a porous silicon free-standing membrane of pore density 5×10^9 pores cm^{-2} is the core and a deposited low loss formvar polymer layer is the cladding. Biosensing using this structure is demonstrated by specific detection of DNA hybridization.

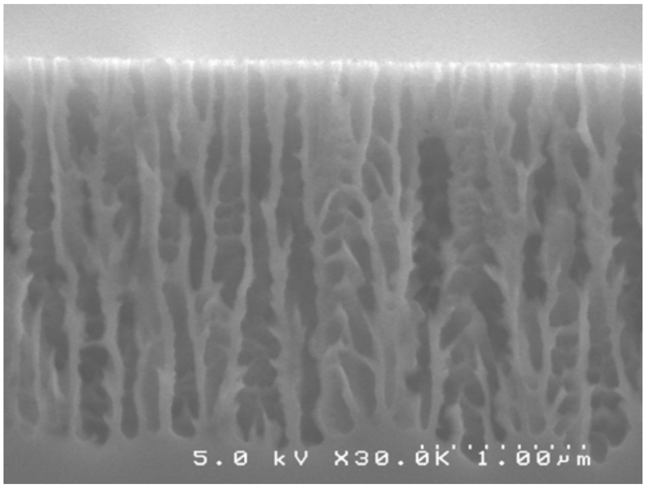

Figure 4.1. Cross-sectional SEM image of an n-type porous silicon layer.

4.2 Structure and operation of the n-type porous silicon membrane waveguide

Figure 4.2 shows the sensor structure which is an asymmetric waveguide. An n-type porous silicon film is the core layer. Air and a formvar polymer film (described in section 4.3) serve as the cladding layers. Similar to the operation of the porous silicon waveguide sensor in the Otto configuration, a TE-polarized 1550 nm laser beam is used to launch the waveguide modes. The beam is incident upon the prism-polymer interface where it undergoes total internal reflection due to the higher refractive index of the rutile prism. The polymer layer is transparent in the infrared, allowing evanescent waves to propagate though the polymer. At a particular angle of incidence θ for which the horizontal component of the incident wave vector in the prism matches that of a waveguide mode, light is coupled into the waveguide. Molecules infiltrated into the porous silicon waveguide change the effective refractive index of the porous silicon, which changes the horizontal component of the wave vector of the guided mode and therefore also changes the coupling angle [93].

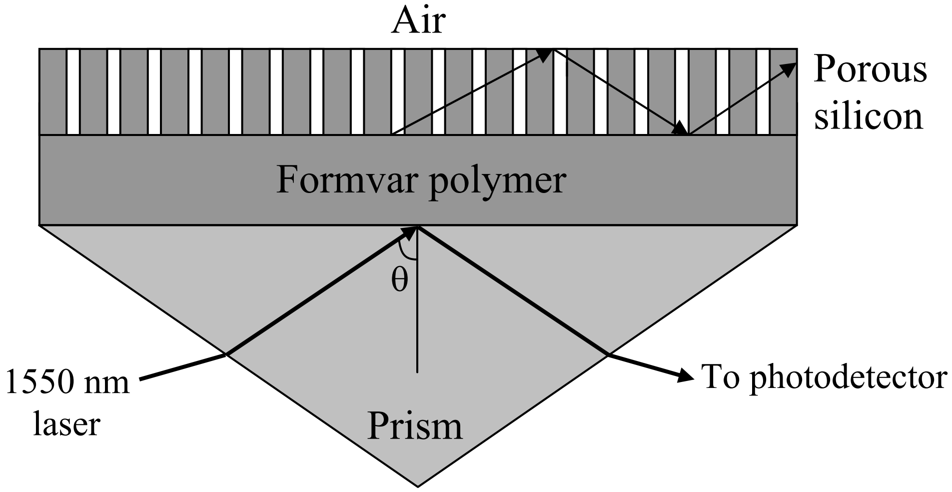

Figure 4.2. Schematic diagram of the n-type porous silicon membrane waveguide biosensor.

4.3 Fabrication

The fabrication of the porous silicon membrane waveguide starts with electrochemical etching of an n-type silicon wafer (<100>, 0.01 Ω·cm) in 5.5 % aqueous hydrofluoric acid. A current density of 40 mA/cm^2 was applied for 35 seconds. The porous silicon film was then removed from the silicon substrate by applying a series of 5 high current pulses (200 mA/cm^2 for 4 seconds with 50% duty cycle). This procedure caused electro-polishing and subsequent detachment of the porous film from the substrate [108]. During the electro-polishing, a slight widening of the pore diameter at the bottom of the porous silicon film occurs. We note that 8-10 porous silicon membranes can be fabricated from the same silicon substrate without significantly degrading the porous silicon film quality. Details of the lift-off procedure are given in Appendix A. The porous silicon membrane was then placed on a BK7 glass slide for ease of handling during oxidation, although the membrane could be held by tweezers. The membrane was oxidized at 500˚C for 5 minutes in an Omegalux LMF-3550 oven, after insertion at 300˚C. To build the waveguide structure, 0.25% formvar polymer in ethylene dichloride (Ernest F. Fullam, Inc.) was dropped onto the surface of a rutile prism (Metricon, n = 2.1252). Ethylene dichloride evaporates quickly to leave behind a thin film of formvar (n ~ 1.5, transparent in infrared region). In order to ensure strong adhesion of the porous silicon membrane to the polymer film, the membrane was placed at the thinner edge of the ethylene dichloride solution drop before the solution completely dried. Using this method, no air gap was formed between the polymer film and the porous silicon membrane, or between the polymer film and the prism. The porous silicon membrane was placed such that the larger pore openings were at the air interface to facilitate molecule infiltration.

4.4 Characterization

A top view SEM of the porous silicon membrane waveguide is shown in Figure 4.3, showing the 100 nm pores and a pore density of approximately 5×10^9 cm^{-2}. In order to determine the thickness of the n-type porous silicon membrane and the approximate thickness of the formvar polymer cladding layer, a porous silicon membrane waveguide with polymer cladding was fabricated on a glass slide. Figure 4.4 shows a cross-sectional SEM image of the n-type porous silicon membrane waveguide. As shown in the figure, the porous silicon membrane is approximately 1 μm thick. Since the polymer layer thickness varies from sample to sample based on the fabrication procedure described in the previous section, the thickness of polymer can only be considered as an approximate thickness for the cladding layer. The actual thickness of the polymer cladding layer of a given waveguide must be determined through measurements on that particular sample.

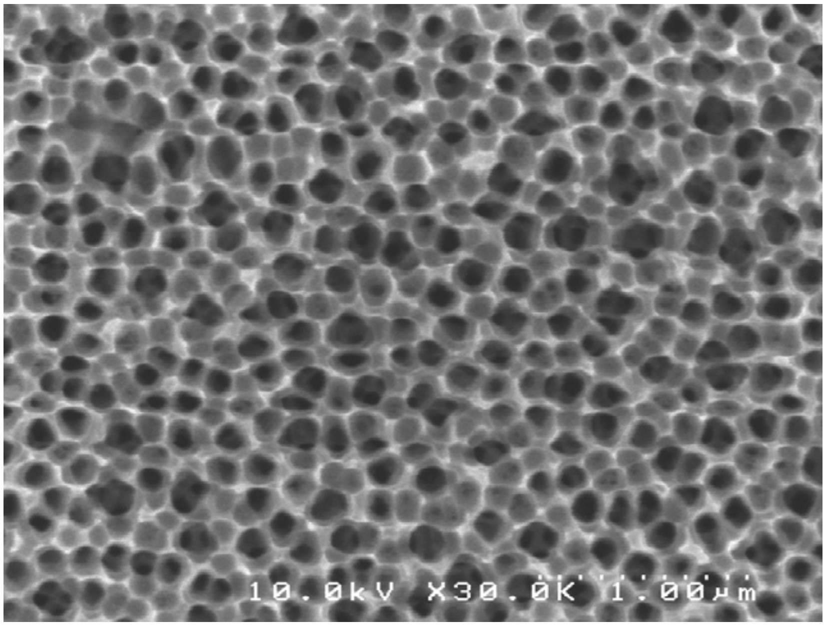

Figure 4.3. Top view SEM of the porous silicon membrane waveguide, showing the slightly widened pores at the bottom of fabricated porous silicon layer after the electropolishing procedure separated the porous silicon layer from the silicon substrate.

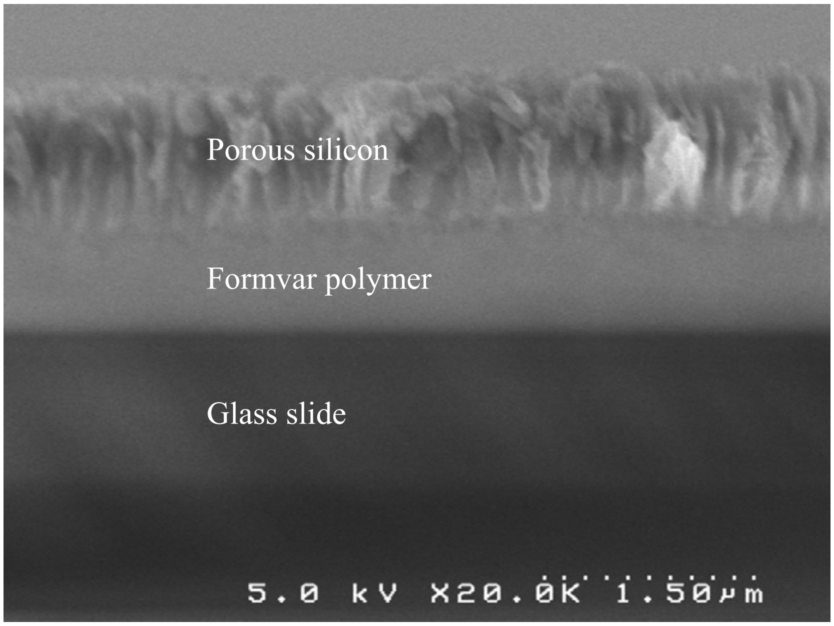

Figure 4.4. Cross-sectional SEM image of the porous silicon membrane waveguide.

The method used to determine the porous silicon membrane refractive index was based on fitting the attenuated total reflectance spectrum of the n-type porous silicon membrane waveguide. This method also enables a determination of the polymer cladding thickness for this membrane waveguide. Using the Metricon 2010 prism coupler, a waveguide mode and a substrate mode have been measured as shown in Figure 4.5. Given the porous silicon membrane thickness of 1 μm and the polymer refractive index of 1.5, the porous silicon refractive index was calculated to be 1.99 and the polymer thickness was determined to be 892 nm by fitting the waveguide mode and substrate mode angles [114]. Figure 4.5 shows good agreement between calculation and experiment. The larger width of the experimental resonance is attributed to scattering losses, which were not taken into account in the calculation. We note that the thickness of the porous silicon membrane and polymer cladding layers has not been optimized, and the waveguide mode measured is the 1st order TE mode. Reducing the thickness of the porous silicon membrane or using a higher index prism would be necessary to measure the 0th order mode.

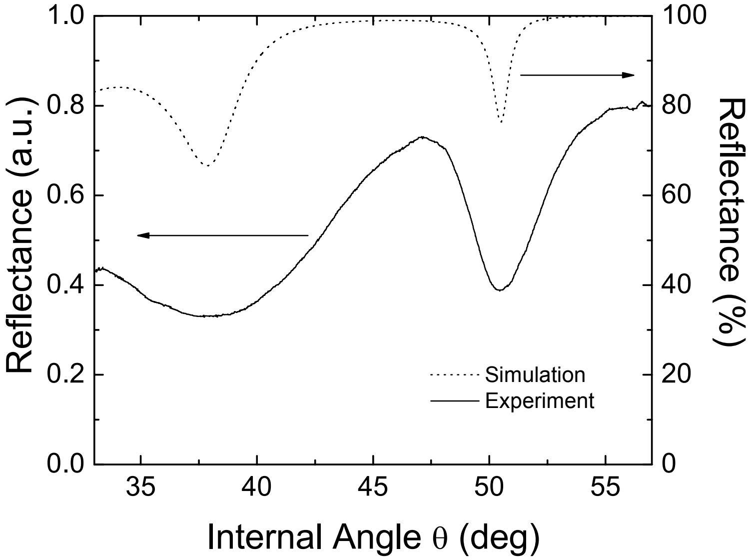

Figure 4.5. Experimental (solid line) and theoretical (dotted line) angle-resolved attenuated total reflectance spectrum of porous silicon membrane waveguide showing the guided mode (50.5°) and substrate mode (37.9°).

4.5 DNA sensing

To demonstrate the biosensing capabilities of the larger pores of the n-type porous silicon membrane waveguide, we detect 24-base and 40-base DNA molecules and compare the results with p-type porous silicon waveguide detection.

4.5.1 Functionalization

A similar procedure as described in section 3.4 using 3-APTES and sulfo-SMCC was carried out to functionalize the n-type porous silicon membrane waveguide for DNA sensing. The oxidized porous silicon film on the prism was first silanized by 3-APTES using similar procedure as described previously in section 3.4.1. Figure 4.6 shows the resonance shift of 0.71˚ following 3-APTES attachment. After silanization, 20 μL of 2mg/mL sulfo-SMCC in 1:1 by volume of water and ethanol was dropped onto the sample surface, and the sample was incubated in solution for 2 hours in a humid environment. Afterwards, in order to remove unbounded species, the samples were soaked in 1:1 by volume of water and ethanol for 1 hour, rinsed by ethanol water mixture and dried in ambient air. The resonance shift after sulfo-SMCC attachment is also shown in Figure 4.6, which is 0.84˚. Compared with the p-type porous silicon waveguide, for which the 3-APTES shifts are 1.55˚ (methods 1, Figure 3.7) and 1.1˚ (method 2, Figure 3.14), and the sulfo-SMCC shift is 1.5˚ (method 2, Figure 3.15), the n-type porous silicon membrane waveguide gives relatively smaller shifts due to its larger pores and thus smaller surface area.

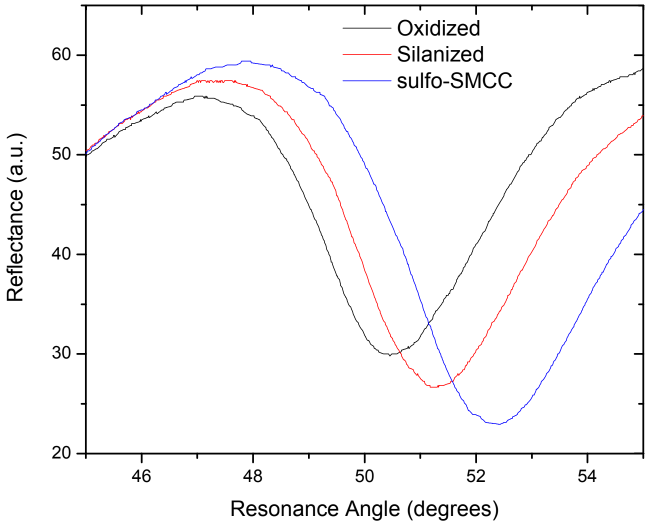

Figure 4.6. Attenuated total reflectance spectra of n-type porous silicon membrane waveguide upon oxidation (black line), silanization (red line), and sulfo-SMCC derivatization (blue line).

4.5.2 24-base DNA detection

Here we demonstrate the detection of 24-base DNA. First, 24-base probe DNA oligos were attached to the porous silicon waveguide in a similar manner as discussed in section 3.4.2, except that 3M of NaCl was added into the resulting 100 μM probe DNA solution after thiol modifier reduction to screen the negative charges [103] on DNA molecules and facilitate molecular infiltration into the porous silicon pores [115]. Afterwards, the 100 μM DNA solution with reduced modifiers was dropped onto the porous silicon waveguide surface. The sample was incubated in the DNA solution for 1 hour in a humid environment. The sample was then rinsed with 1:1 water and ethanol, incubated in 1:1 water and ethanol, rinsed again with 1:1 water and ethanol, and then dried in ambient air. The resonance after 24-base probe DNA attachment is shown in Figure 4.7, with a resonance shift of about 1˚. Control experiments were carried out where a solution of 3M NaCl, HEPES buffer and 100 μM TCEP was added onto sulfo-SMCC functionalized porous silicon waveguide sample and incubated by the same procedure, and no resonance shift was observed, as shown in Figure 4.8.

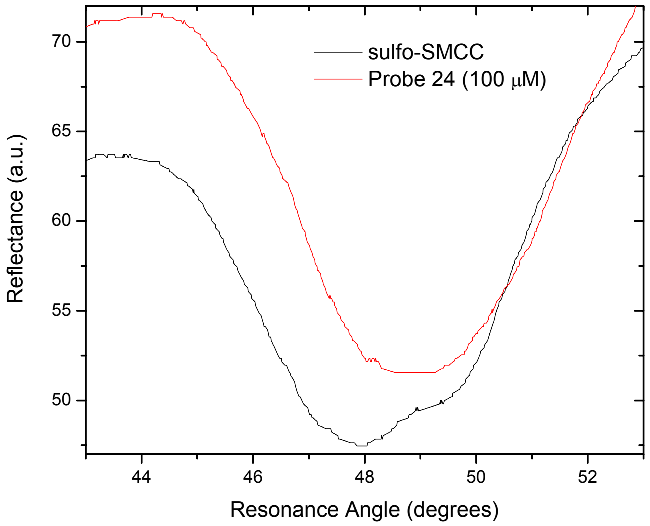

Figure 4.7. Resonance shift of 1° for the n-type porous silicon membrane waveguide upon attachment of 100 μM 24-base probe DNA.

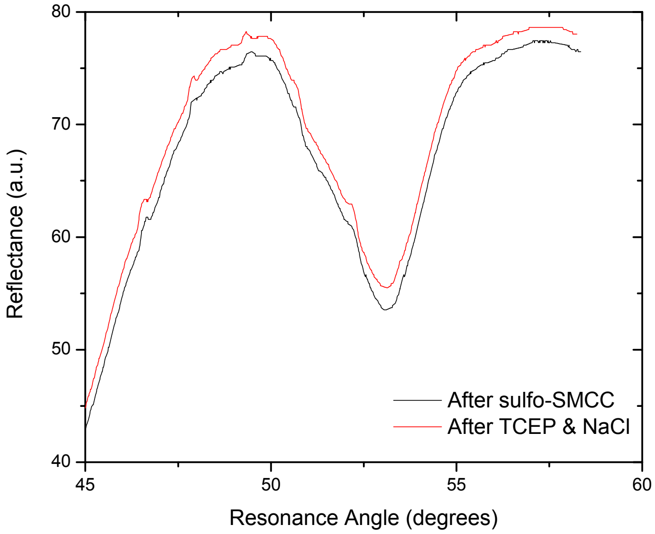

Figure 4.8 Control experiments where exposure to 3 M NaCl and 100 μM TCEP gives no shift for the sulfo-SMCC functionalized porous silicon waveguide.

After probe DNA attachment, DNA hybridization experiments were carried out. Different concentrations of 24-base target (complementary) DNA and mismatch (non-complementary) DNA in 1:1 water and ethanol were added onto porous silicon waveguide samples separately and the samples were incubated for 1 hour in a humid environment. Again, 3M of NaCl was added to the DNA solutions. The sample was then rinsed with 1:1 water and ethanol, incubated in 1:1 water and ethanol, rinsed again with 1:1 water and ethanol, and then dried in ambient air for the purpose of removing unbounded species. Figure 4.9 shows the results for detection of different concentrations of target DNA. The error bars are given for three measurements. The average resonance shifts are linearly fitted, giving a sensitivity of 0.048˚/μM. Since the prism coupler has an angular resolution of 0.002˚, the ultimate detection limit of the n-type porous silicon membrane waveguide biosensor is 42 nM. Control experiments were done where 1 μM of mismatch DNA was added onto the porous silicon waveguide sample and the sample was incubated through the same procedure. As shown in Figure 4.10, no observable resonance shift was detected, confirming the selectivity of the n-type porous silicon waveguide biosensor.

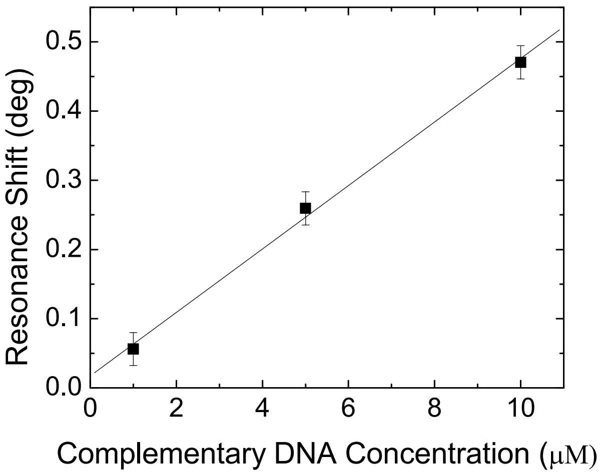

Figure 4.9. Measured angular shift of guided mode after exposure to various concentrations of 24-base pair DNA oligonucleotides. A linear fit of the data points suggests a sensitivity of 0.048°/μM and a detection limit of 42 nM.

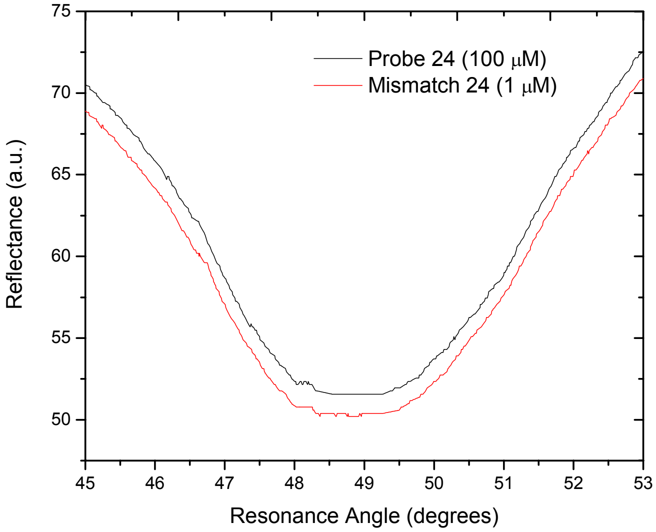

Figure 4.10. Control experiments showing no resonance shift for the mismatch (non-complementary) DNA.

4.5.3 40-base DNA detection

40-base DNA detection has also recently been carried out with the n-type porous silicon membrane waveguide. The procedure is the same as for 24-base DNA detection. No resonance shift has been observed for 100 μM of 40-base probe DNA attachment, which suggests that the 40-base DNA molecules may be too large to efficiently infiltrate into the 100 nm pores using the current conditions. The nominal length of the 40-base probe DNA is 8.8 nm. The total length of the molecular layers including the chemical linkers is about 11 nm. Further optimization of the reaction conditions for probe DNA attachment are needed to facilitate 40-base DNA infiltration and immobilization. Due to more negative charges on the 40-base DNA molecules, the intermolecular interactions are stronger, which makes infiltration into the nanoscale pores more difficult. In addition, the longer DNA strands are more likely to bend and fold [116], which may complicate the molecule infiltration and binding [99]. Possible ways to solve the problem include heating while incubating to give DNA molecules more energy in diffusive movement, and using higher ionic strength to screen the negative charges in order to weaken the intermolecular interactions. For example, Mg^{2+} ions are more efficient than Na^{+} ions in screening negative charges since they have double positive charges.

CHAPTER V

BIOMOLECULAR SIZE DEPENDENT SENSITIVITY

5.1 Introduction to size dependent sensitivity

In order to improve the experimental sensitivity of the porous silicon waveguide biosensor, it is necessary to study the effect of biomolecule size on the porous silicon waveguide detection sensitivity. Porous silicon biosensors, as well as other biosensors based on porous materials, are limited to the detection of molecules smaller than the pore diameter. However, at nanoscale dimensions, it is not obvious what minimum pore-size-to-biomolecule-size ratio is necessary to allow for efficient infiltration of the molecules into the nanoscale pores. Furthermore, when evaluating the utility of porous materials for sensing applications, one must consider not only the size-dependent infiltration efficiency of biomolecules, but also the magnitude of the sensor response as a function of biomolecule size. As illustrated in Figure 5.1, molecules much smaller than the pore diameter will be easily infiltrated, but these molecules will occupy only a small percentage of the pore volume and hence will only have a small impact on, for example, the optical properties of the porous material. On the other hand, molecules whose size approaches the pore diameter will have a strong effect on the optical properties of the porous sensor but will have great difficulty infiltrating into the pores. Molecules of the appropriate size that can infiltrate into the pores and can change the optical properties of the porous sensor substantially will be detected most sensitively.

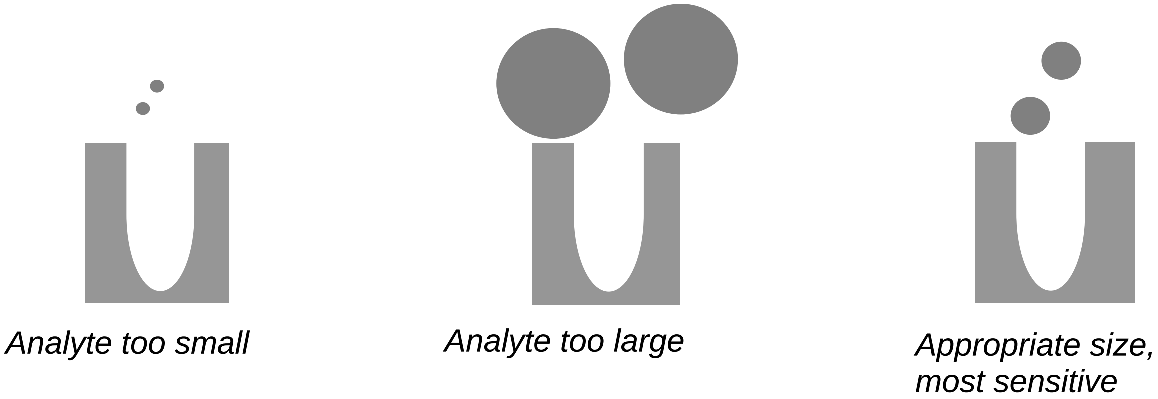

Figure 5.1. Different biomolecular sizes relative to the same pore size, resulting in different sensitivity of detection for the porous materials based biosensors.

Ouyang and co-workers previously examined the sensitivity of porous silicon microcavity biosensors as a function of pore size and effective monolayer coating thickness using a simplified effective medium approximation [37]. Calculations suggested that the sensor response increases for thicker coatings of material on the pore walls, and it was experimentally shown that molecules of size less than one-tenth of the pore diameter were detected more sensitively as a function of decreasing pore size. For larger molecules, this size-dependent sensitivity scaling trend does not necessarily hold true due to the added challenges associated with molecular infiltration that prevent the formation of uniform monolayers of biomolecules.

In this chapter, we investigate the biomolecule size-dependent sensitivity of porous sensors for which the biomolecule size approaches the pore radius. Revised resonant porous silicon waveguides (method 2) with pore diameters of 30 nm as described in section 2.3 were used as the model nanoporous biosensors due to their high detection sensitivity and because their active sensing region is easily accessible as the top porous layer, minimizing the necessary biomolecule infiltration distance [93]. DNA molecules of length between 1.76 and 5.28 nm are chosen as the model size-variable biomolecules, which are attached to the porous silicon with cross-linking chemicals 3-APTES and sulfo-SMCC. As measured by ellipsometry and reported in the literature, one monolayer of 3-APTES is approximately 0.8 nm [37] and one monolayer of sulfo-SMCC is 1.9 nm. DNA is a convenient molecule choice for these experiments since its length is easily manipulated by changing the number of bases in the DNA sequence.

5.2 Simulation of resonance shifts for variable length of probe DNA

Calculations of the expected resonance shift for different lengths of DNA at different pore wall coverage densities have been performed. The calculations, which were based on the Bruggeman effective refractive index of porous silicon and the waveguide mode equation (2.5), ignored the length of thiol modifiers (approximately 5-6Å including a bridge of three carbon atoms), which is small compared to the length of the DNA strands used in the experiments. First, the calculation assumes that DNA molecules can infiltrate into the pores without difficulty and can be densely packed on the pore walls to form a monolayer. Second, for simplicity, it is assumed that the thickness of one monolayer of DNA is equal to the DNA length given in Table 5.1, using a base-to-base distance of 2.2 Å [107]. With these assumptions, the only limitation on DNA length for infiltration into the pores is the pore diameter. Figure 5.2 shows the results of the simulation, giving the relationship between resonance shift and probe DNA coverage for different lengths of DNA. Increased DNA coverage on the pore walls corresponds to higher DNA concentrations exposed to the waveguide. The calculations suggest that the porous silicon waveguide sensitivity is highest for 24-base DNA detection. The 24-base molecule is the longest one considered and occupies the largest fraction of the pore volume, thus causing the largest refractive index change.

Table 5.1. Fully extended DNA length for different numbers of bases [107].

Number of bases	8	16	20	24
DNA length (nm)	1.76	3.52	4.4	5.28

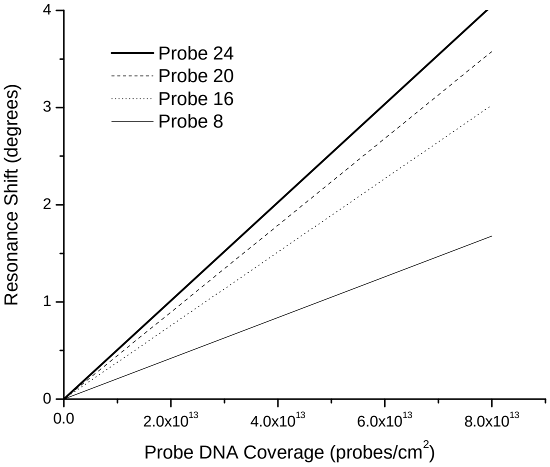

Figure 5.2. Simulated resonance shift for different lengths of DNA at different pore wall coverages, where 8×10^{13} probes/cm^2 corresponds to 100% coverage. The slope of the linear curve is the sensitivity of detection. The 24-base DNA molecules can be detected most sensitively because their infiltration into the porous silicon waveguide causes the largest refractive index change. The simulation ignores practical infiltration challenges and assumes that the DNA molecules can infiltrate into all pores with diameters larger than the DNA length.

5.3 Experimental resonance shifts for variable length of probe DNA

In experiments, the nanoscale pore size has an effect on the infiltration efficiency, and DNA may not necessarily form a monolayer inside the pores. To study this effect, we carried out attachment of probe DNA of variable length onto p-type porous silicon waveguides (method 2) and measured the resonance shift to quantify the amount of DNA immobilized inside the pores. Fabrication of the revised porous silicon waveguide (method 2) was described in section 2.3. Figure 5.3 shows a plan-view scanning electron microscopy image of the porous silicon waveguide, with average pore diameters of about 30 nm. The functionalization procedure for attaching probe DNA was based on 3-APTES and sulfo-SMCC chemical linkers as described in section 3.4.2.

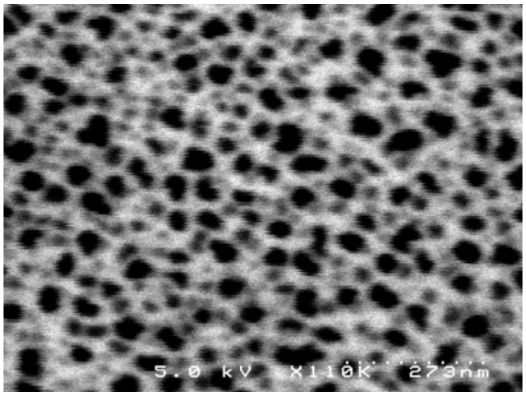

Figure 5.3. Plan-view SEM image of a mesoporous silicon waveguide after 30 minutes of KOH soaking to open up the pores. The average pore diameter is approximately 30 nm.

One of four different DNA molecules (thiol modifiers reduced by TCEP) was immobilized in the maleimide-derivatized porous silicon waveguides:

Probe 24: 5’-TAGC TATG GAAT TCCT CGTA GGCC-3’
Probe 20: 5’-TATG GAAT TCCT CGTA GGCC-3’
Probe 16: 5’-TAGC TATG GTCC TCGT-3’
Probe 8: 5’-GGGG GGGG-3’.

DNA solutions of volume 100 μL and concentrations of 100 μM, 50 μM and 25 μM were infiltrated into porous silicon waveguide samples and incubated for 1 hour, followed by a 20 minute soak in buffer, rinsing with DI water, and drying with nitrogen. The waveguide resonance angle was measured after each functionalization step using the prism coupler to confirm the attachment of the chemical linkers and quantify the attachment of DNA in the waveguide.

Figure 5.4 summarizes the results of the experimental measurements for which DNA molecules of different lengths and different concentrations were infiltrated into porous silicon waveguides. The magnitude of the resonance shift directly relates to the quantity of DNA immobilized in the pores, with larger shifts indicating more DNA was attached. The slope of each linearly fitted curve is the sensitivity (degree shift of waveguide resonance per micromolar concentration of DNA infiltrated into the waveguide) of detecting DNA molecules consisting of a particular number of bases. Each data point represents an average of multiple measurements and has an associated error bar. In contrast to the calculations that ignore infiltration challenges, the experiments show that 8-base DNA is most sensitively detected by the porous silicon waveguide. For a given concentration of DNA, the 8-base and 16-base DNA sequences yield the largest waveguide resonance shifts, which infer that these strands infiltrate into the pores and cause a substantial refractive index change. The 8-base DNA likely has better infiltration efficiency since the refractive index change due to the attachment of a single 8-base strand is less than that due to a single 16-base attachment. Thiol-modified DNA sequences shorter than 8-bases were not available due to synthesis challenges with such short strands. The sensitivity of detection was nearly zero for 24-base DNA. It is believed that the 24-base DNA was too large to efficiently infiltrate into the pores with the sulfo-SMCC cross-linker. We note that it was possible to detect 24-base DNA using the smaller cross-linker glutaraldehyde. We further note that some of the curves in Figure 5.4 do not extrapolate to the (0,0) point for two primary reasons: first, the negatively charged DNA molecules can corrode the porous silicon as mentioned in section 3.3.3 [103], and second, not all the DNA molecules in solution will bind to the pore walls, as was assumed in the simulation.

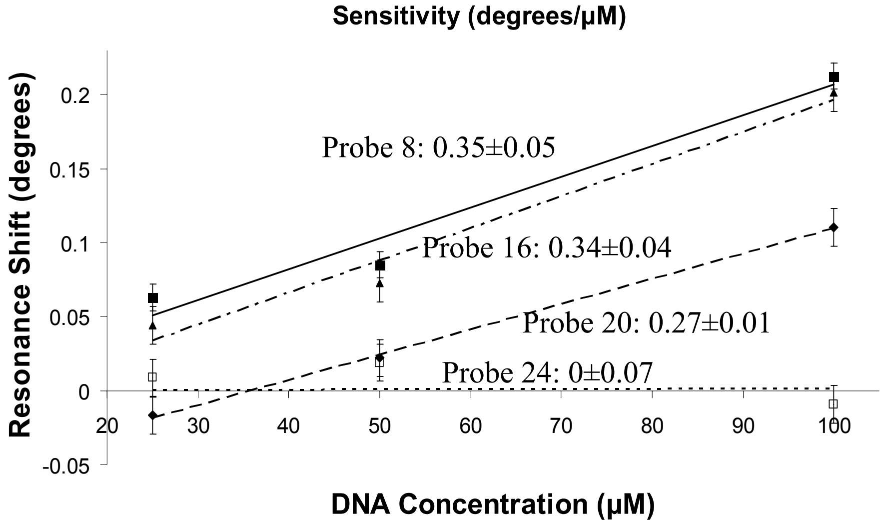

Figure 5.4. Experimental results showing the resonance shift of porous silicon waveguides at different concentrations (25-100 µM) and different lengths (8-24 bases) of DNA. The slopes of the linearly fitted curves are the sensitivities of detection. Each data point includes an error bar, and the detection sensitivity with associated error range for each DNA length is also shown.

5.4 Discussion

Comparing Figures 5.2 and 5.4, it is clear that the effects of infiltrating DNA into confined regions cannot be ignored. At confined, nanoscale dimensions, molecule-surface interactions, such as Van der Waals forces, play a significant role. Thus, while 24-base DNA is unable to efficiently infiltrate into a pore with an opening approximately 4.5 times larger than the DNA length, the same molecule would experience no substantial inhibiting forces when it infiltrates a hole much larger than its size. Accordingly, experiments in which molecules are infiltrated into the larger, 100 nm pores of the n-type porous silicon waveguide (described in Chapter 4) were performed. For the n-type porous silicon waveguide, the shift for attachment of 24-base probe DNA of 100 μM concentration is 1°. Figure 5.5 presents a summary of the resonance shifts for the p-type and n-type porous silicon waveguides for different lengths of DNA at 100 μM. While the size analysis for the n-type is not complete and final trends cannot yet be determined, it is clear from Figure 5.5 that larger pores enable the detection of larger molecules and molecules must be significantly smaller than the pore radius to be efficiently detected.

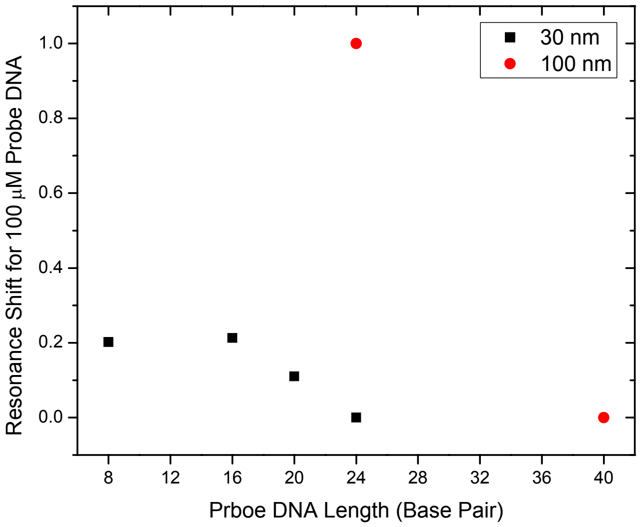

Figure 5.5. Resonance shifts for the p-type and n-type porous silicon waveguide for different length of DNA at the same 100 μM concentration.

CHAPTER VI

CONCLUSION AND FUTURE RESEARCH

6.1 Conclusion and research contribution

A sensitive label-free optical biosensor based on a resonant porous silicon waveguide has been demonstrated. Two waveguide structures were presented. The first one was a p-type porous silicon waveguide with 20-30 nm pores in the Otto configuration, and the second one was an n-type porous silicon membrane waveguide of 100 nm pores in the Kretschmann configuration. DNA hybridization was detected in both types of waveguides by measuring an angular resonance shift. Negligible shift was measured for exposure to non-complementary DNA. The large surface area available for biomolecular attachment and strong field confinement in the region where biomolecules are immobilized make it possible for the porous silicon waveguide to detect DNA hybridization with high sensitivity. For the p-type porous silicon waveguide, theoretical calculations suggest that the sensor has a detection limit of 5pg/mm^2, or 50 nM of analyte. For the n-type porous silicon membrane waveguide, experimental detection with sensitivity of 0.048°/μM and detection limit of 42 nM were demonstrated. The effect of biomolecular size on the sensitivity of detection with the porous silicon waveguide has also been studied using DNA molecules of different lengths (different number of bases). For the p-type porous silicon waveguide, it was found that 8-base DNA has the highest sensitivity of detection. Corresponding simulations illustrated that size-dependent molecule infiltration efficiencies cannot be neglected. DNA molecules had to be approximately 5 times smaller than the pore radius to infiltrate into the p-type porous silicon waveguide. Large molecules, such as 24-base DNA were efficiently infiltrated and detected in the larger pores of the n-type porous silicon waveguide.

6.2 Future research opportunities

6.2.1 New designs for porous silicon waveguide sensor

6.2.1.1 Porous silicon membrane sensor chip

The n-type porous silicon membrane waveguide described in Chapter 4 can also be designed in a sensor chip configuration as shown in Figure 6.1. The waveguide, including the formvar polymer and porous silicon free-standing membrane, can be deposited on a glass slide that has the same refractive index as the prism. Index matching oil that has the same refractive index as the prism can be used to fill the air gap between the glass slide and prism. Then the prism, oil, and glass slide form a homogeneous medium, making the structure the same as presented in Figure 4.2. The sensor chip, including the glass slide, polymer, and porous silicon membrane, is an independent module that can be removed from the prism for ease of functionalization and sensing. The sensor chip can also be designed such that it is compatible with the commercial SPR instruments.

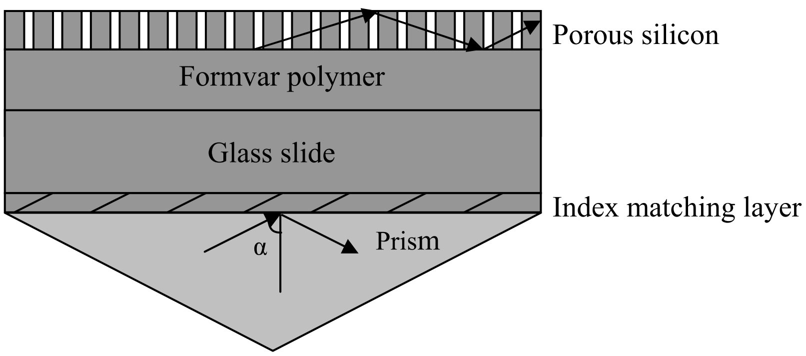

Figure 6.1. Sensor chip setup of the porous silicon membrane waveguide biosensor.

6.2.1.2 Metal-cladded porous silicon waveguide

The real part of the refractive index of metal is very small (n<1). Thus metal can be used as a waveguide cladding layer. The low refractive index improves the guided mode confinement but the metal is also a source of losses due to a large absorption coefficient. For the n-type porous silicon membrane waveguide, instead of using the formvar polymer, a metal layer such as gold, silver, copper or aluminum can be used. The structure is the same as shown in Figure 1.6. Waveguide mode, instead of SPR mode, is interrogated for sensing. As discussed in section 1.4, there are reports of sensing using waveguide structures consisting of porous-material based core and metal cladding [32, 33]. A further possibility exists to use the metal layer as an electrode. A counter electrode, inserted into the solution during incubation of biomolecules, could then be used to establish an electric field across the porous silicon, with the idea of using the electric field to more efficiently drive the molecules into the pores. The biomolecules would only feel the electric field if they carried a net charge; the conditions under which appropriate charge states could be realized would need to be carefully studied.

6.2.1.3 Porous silicon waveguide with grating coupler

For more compact sensors, a grating coupler can be used to couple light into a waveguide instead of a prism. Figure 6.2 shows a grating coupled porous silicon waveguide structure. The periodic grating diffracts the incident light and can provide the necessary momentum to couple light into a guided mode if the following condition is met:

$$\frac{2\pi}{\lambda}\sin\theta \pm m\frac{2\pi}{\Lambda} = k_{WG} \qquad (5.1)$$

where Λ is the grating period, m is the diffraction order, λ is the wavelength of the incident light, θ is the angle of incidence and k_{WG} is the wavevector of the waveguide mode for the given waveguide structure.

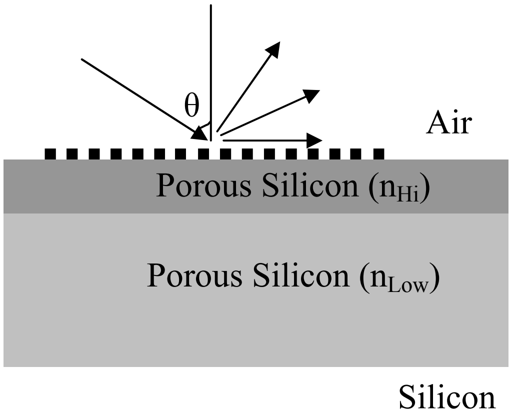

Figure 6.2. Grating coupled porous silicon waveguide.

The grating coupled waveguide also has the potential to be integrated with microfluidics. However, there are two issues of concern. First, the grating covers part of the porous silicon, effectively making those areas non-sensitive regions of the sensor where molecules cannot infiltrate. Second, the grating fabrication requires specialized lithographic tools since the grating spacing is typically submicron. Each porous silicon waveguide requires a grating to be fabricated on it and each sample is used for only one experiment. To overcome these challenges, Figure 6.3 proposes a new design. A microfluidic cell is placed on top of a porous silicon waveguide. The grating is fabricated on the microfluidic cell cover. The microfluidic cell can be nanoscale thick [117] so that the evanescent wave generated by grating diffraction can tunnel through it and couple into the porous silicon waveguide. Biomolecular solution in buffer or water can flow through the nanofluidic cell and the full porous silicon waveguide area is available for sensing. Also, the grating can be re-used for many times since replacing the sensor chip simply involves replacing the porous silicon waveguide below the flow cell. A major challenge of this design is the stabilization of the fluidic system after the injection of liquids such that coupling of light by the grating and real time measurements are not inhibited. Typically, the flow is stopped for some wait time to allow equilibration in the fluidic system before measurements are taken.

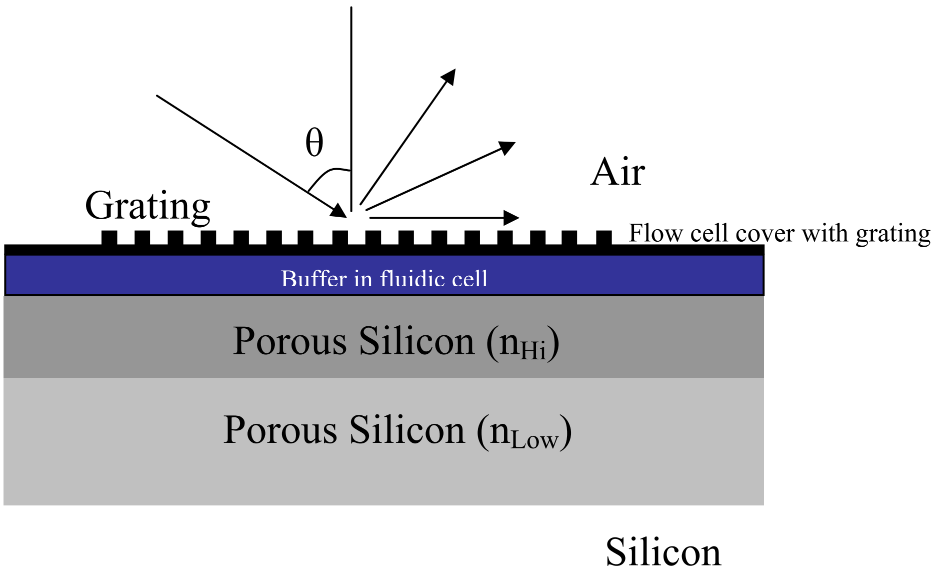

Figure 6.3. A grating coupled porous silicon waveguide incorporating microfluidic flow cells. The grating is fabricated on flow cell cover and can be re-used. The entire area of the porous silicon waveguide is available for sensing.

6.2.1.4 Porous silicon slot waveguide

A vertical slot waveguide for which the optical field is confined in a very thin, low refractive index region can be fabricated in porous silicon [118]. In this case, the field is concentrated in the high porosity porous silicon layer that has more surface area than a low porosity layer. Very large field confinements have been demonstrated in silicon horizontal slot waveguides [119], which suggests that high sensitivity can be achieved in the slot waveguide configuration [120-122]. Figure 6.4 shows an SEM image of a fabricated p-type porous silicon slot waveguide. The main disadvantage of the porous silicon vertical slot waveguide is that the molecules to be detected must diffuse through the upper low porosity layer before reaching the high porosity active sensing region.

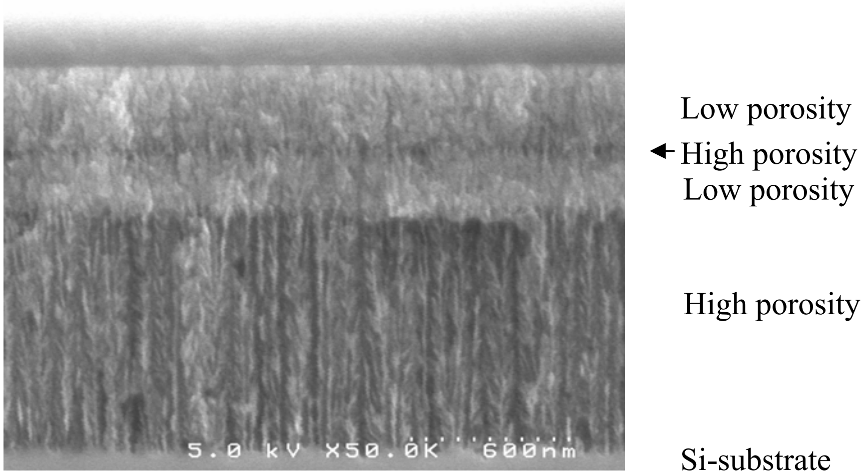

Figure 6.4. The SEM of a fabricated p-type porous silicon slot waveguide.

6.2.1.5 Porous silicon waveguide interferometer sensor

The porous silicon waveguide can be set in an interferometer scenario to detect the phase change of propagating waves due to interaction with biomolecules. As shown in Figure 6.5, two grating coupled waveguides can be used as two arms of an interferometer. The beam from a light source is collimated into a parallel beam of large enough spot size, which is then incident upon two grating coupled porous silicon waveguides. The light waves are coupled into the waveguides at θ and propagate through the waveguides. On exiting the waveguides, they can be coupled into two single mode optical fibers by an efficient three dimensional taper [123]. The two waves can then be combined and they interfere in the same way as described for single porous silicon interferometer sensor (section 2.1.4) to form fringe patterns detectable by a spectrophotometer. One waveguide is the reference arm with no biosensing function and the other one is the active sensing arm. If biomolecular binding occurs in the sensing porous silicon waveguide, the light wave propagating in it experiences a phase shift relative to the light propagating in the reference arm. The phase change is proportional to the amount of molecules bound in the sensing porous silicon waveguide. The sensor can have high sensitivity of detection due to the longer field-molecule interaction distance [25]. One concern of this design is that the dynamic range of the sensor is not very large, since the maximum amount of phase shift is 2π in order to avoid aliasing problems.

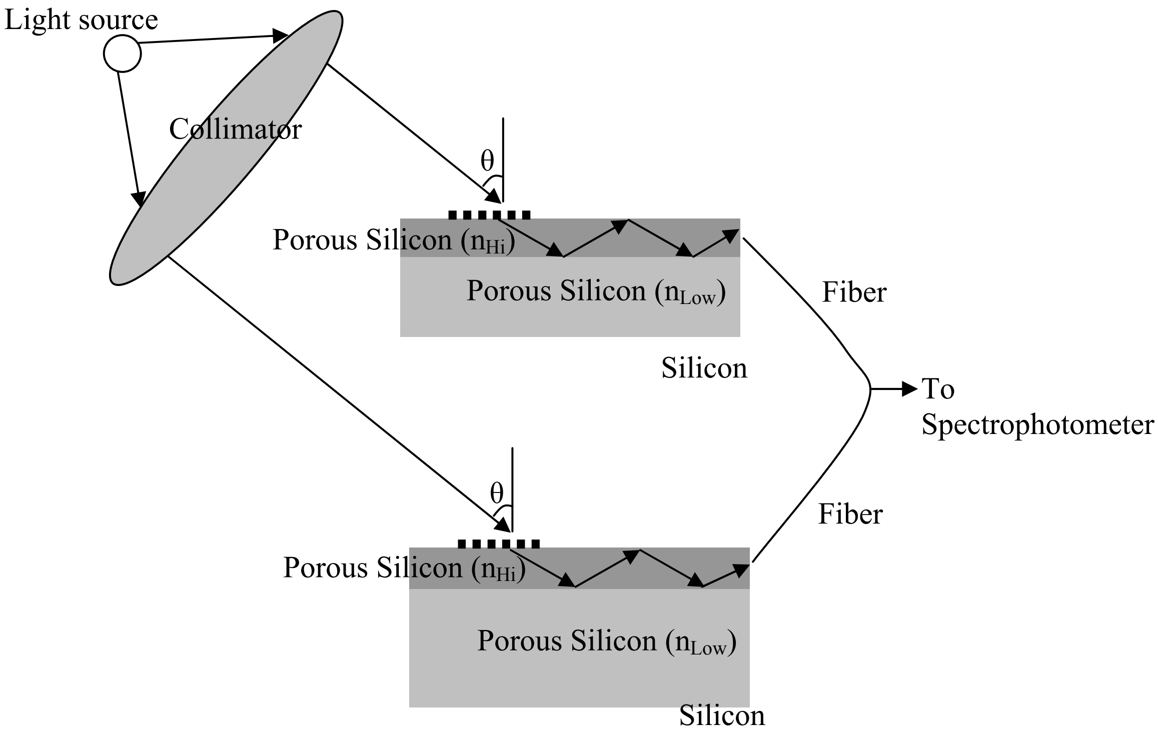

Figure 6.5. Porous silicon waveguide interferometer sensor.

6.2.2 Detection of a variety of biological molecules

In addition to DNA, many other biological species can potentially be detected using a porous silicon waveguide biosensor. The porous silicon waveguide biosensor is especially sensitive toward small molecule detection. Toxins of a few nanometers should be detected very sensitively with the p-type mesoporous silicon with 20-50 nm pores [124]. Enzymes can also be detected with p-type mesoporous silicon [124]. Larger species such as proteins, e.g., antibody-antigen interactions [125], can be detected with an n-type porous silicon membrane waveguide with 100 nm pores. The key to the detection of these various molecules is choosing the appropriate pore size and the proper biochemistry for linking the molecules to porous silicon.

6.2.3 Sensor array

To enable higher throughput sensing, a sensor array is highly desirable. Many simple new techniques can be adapted in standard lithography to pattern porous silicon [126-131]. Distinct and isolated porous silicon waveguides sensors can be formed on a silicon wafer (as shown in Figure 6.6), with each functionalized to detect a different target molecule. Careful consideration would have to be given to determine the most effective means of individually addressing each sensor in the array.

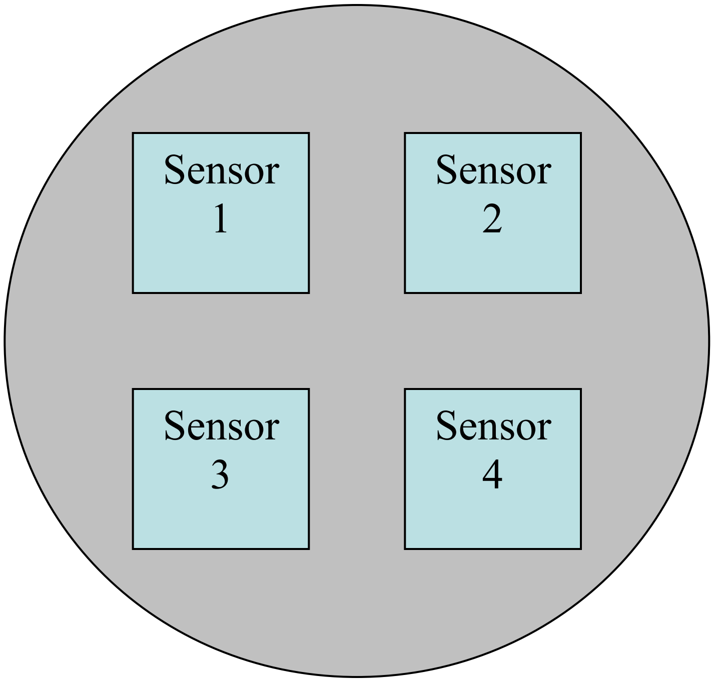

Figure 6.6. Sensor array for high throughput sensing. The actual density of sensing elements will be higher.

6.3 Prospect of biosensor research

As discussed in Chapter 1, an ideal biosensor should have very high sensitivity and specificity, low cost, high throughput, ease of use, and stability. As research is advancing, future biosensor should possess all these desirable properties. Development in photonics makes it possible to fabricate nanoscale devices with three-dimensional sub-wavelength field confinement. Combined with nanotechnology, it is possible to make ultra-sensitive, even single molecule, nanosensors. The continued development of biomaterials will help researchers find the best biomolecular probes for various target species. High affinity and low false positive can be achieved at the same time. Advancements in biochemistry and biophysics will help researchers better understand the behaviors of biomolecules and accordingly design biosensors to more efficiently sense biomolecular interactions.

Biosensor research will continue to be highly interdisciplinary. With the integration of the above mentioned and many other related research areas, the prospect for biosensors research is highly optimistic. Tremendous opportunities exist and the advancement should have much to contribute to the human quality of life.

APPENDIX A

POROUS SILICON FABRICATION PROCEDURE

Porous Silicon Fabrication Procedure

1. Cut the silicon wafer into pieces of 2.5 cm × 2.5 cm.
2. Before etching, rinse the silicon wafer piece with water and ethanol. Dry it with nitrogen gas using the pipette-tip-connected tube inside the chemical hood.
3. Place the silicon wafer piece in the etching cell, and assemble the cell as shown in Figure A.1. Check to make sure that there is no contact between the metal foil (e.g. silver or platinum) below the silicon wafer and the four bars that support the Teflon etching cell. One corner of the metal foil should stick outside of the Teflon cell to enable electrical contact to be made. Also, make sure the screws on the four bars are tight enough to prevent any leakage. Finger tight is sufficient. Over-tightening may cause uneven pressure on the silicon, which may reduce the porous silicon uniformity.
4. For safety, the etching should take place in a chemical hood. Put the etching assembly inside the chemical hood at least 10 cm away from the hood outer edge.
5. Use a plastic pipette to take out HF solution from a plastic bottle and squeeze it into the etching cell. The level of HF solution should be somewhat more than just covering the platinum wire.
6. Try to get rid of any bubbles in the solution to improve etching uniformity.
7. Fill in the correct current density and etching time values into the LabView program that controls the current source (Keithley 2425 SourceMeter).
8. Try running the program without any electrical wire connection yet, just to make sure that the program runs as expected.
9. Connect the black wire of the current source to the platinum wire and the red wire of the current source to the metal foil below the silicon wafer.
10. Run the etching program to carry out the actual porous silicon etching (Note: if fabricating porous silicon free-standing membrane, see next page for steps).
11. After finishing etching, use a pipette to take out the HF waste and place in a plastic container in the hood. Then rinse the etching cell and the platinum wire three times with ethanol. Make sure the cell wall gets rinsed as well.
12. Dissemble the etching cell. Rinse the porous silicon sample with ethanol. Do not squirt ethanol directly on porous silicon, but squirt on the outer silicon region and allow ethanol to flow over the porous silicon area. Also, remember to rinse the back side of the porous silicon sample and the tweezer. Then dry the porous silicon sample with nitrogen gas blow.
13. Before etching another sample, rinse the inner part of the Teflon etch cell and dry it with nitrogen. This procedure helps prevent the residual HF solution, water or ethanol from affecting the HF concentration of the new etching solution.
14. After all samples have been etched, rinse every piece of the etching assembly with ethanol. Collect the waste solution in the same plastic waste container.
15. Wash every piece of the etching assembly by DI water and dry them in air.
16. Inside the chemical hood, put the HF waste in a large plastic waste bottle (e.g. 1 gallon) and keep the bottle in the cabinet under sink in a secondary containment tub until chemical waste pick-up. Make sure that the waste bottle is properly labeled with the Vanderbilt Environmental Health and Safety waste tag.

Optional Steps for Porous Silicon Lift-off

Steps 1-10 are the same as described on previous page. Then follow the steps given below:

A. Apply the current density pulses to remove porous silicon film from substrate by changing the current density and etching time values in the LabView program and run the program (For example, see procedure described in Section 4.3.).
B. After finishing etching, use a pipette to take out the HF waste and place in a plastic container in the hood. Ensure that the free-standing porous silicon film does not dry out (i.e., leave a small amount of residual liquid on the film). Then rinse the etching cell three times with ethanol. Do not squirt ethanol directly on the fragile porous silicon film. Make sure the cell wall gets rinsed as well. Again, never allow the porous silicon film to become dry during this procedure.
C. Take the cover of a plastic Petri dish. Flip it over and put ethanol solution in it up to about 0.5 cm high.
D. Dissemble the etching cell. Take the O-ring off the silicon piece. Use a tweezer to hold the silicon piece while squirting ethanol gently around the porous silicon so that the porous silicon film can be carefully moved into the ethanol solution in the Petri dish cover.
E. The porous silicon film can be broken into pieces of desirable sizes by a tweezer. Typically, a piece of 0.2 cm^2 is sufficient for building a waveguide measurable with the prism coupler.
F. Holding the two sides of a Kimwipe paper, use the central part of the paper to take out a porous silicon piece and dry it in air. Many pieces can be obtained from a single etch.
G. The front side of the n-type porous silicon film where pore openings are smaller is typically shinier, and the back side where pore openings are larger is typically duller. The difference is more obvious under good lighting conditions.
H. Rinse the silicon substrate with ethanol, both front and back sides. It can be used again for etching porous silicon films.

Then follow steps 13-16 as previously described.

Figure A.1. Etching cell assembly, its electrodes connection with current source, and the resulting porous silicon samples after etching (Figure courtesy of Ph.D. dissertation of Sharon M. Weiss, University of Rochester, 2005).

APPENDIX B

OPTIMAL CLADDING THICKNESS CALUCULATION CODE

```
lambda=1550e-9;
k=2*pi/lambda;
km=1.5245*k;
ks=0.3465*k;
n1=1;
n2=2.1725;
n3=1.2801;
n4=3.4784;
loss=10;    % in dB/cm
gamma=5*loss/log10(exp(1));  % gamma value corresponding to loss
phi=2*atan(sqrt((km^2-k^2*n3^2)/(k^2*n4^2-km^2)));
pm=-i*sqrt(k^2*n3^2-km^2);
Dopt=-log(gamma/(ks*sin(phi)))/(2*pm)
```

APPENDIX C

PRISM COUPLER MEASUREMENT PROCEDURE

Metricon 2010 Prism Coupler Measurement Procedure

1. Open the Metricon prism coupler control software, MetriconMCU.exe.
2. Cancel the request for referencing the table.
3. Check the "Parameters" form. Select "dual film" for measurement type. Enter other parameters as described in the manual.
4. Reference the Metricon prism coupler according to the procedure given in the manual.
5. Use a tweezer to hold the porous silicon waveguide sample and put the sample in the metal sample holder. The porous silicon waveguide should be facing towards the prism. Hold the sample steady without touching the prism to avoid scratching the sample and damaging the prism. Align the sample such that its bottom edge rests on the two pins of the sample holder at the bottom and its left edge touches the left pin of the sample holder. The three pins of the sample holder are for repeatable re-positioning of the porous silicon waveguide sample. Stabilize the sample in the sample holder such that the sample is tilted backward toward the coupling head as shown in Figure C.1. The bottom side of the sample should rest on the outer several millimeters of the bottom two pins.
6. Adjust the coupling pressure to appropriate value by turning the coupling pressure knob. Adjust the coupling head moving speed so that the sample will not be damaged by coupling. On the other hand, if coupling speed is too low, then the coupling head will not push the sample toward the prism.
7. Apply the coupling pressure and the coupling head will push the porous silicon waveguide up against the prism.
8. Adjust the beam position according the manual.
9. Carry out the scanning of reflectance vs. angle spectrum as described in the manual.
10. Sometimes the waveguide resonance is not found. Adjusting the beam position and the coupling pressure should help find the resonance. Also, cleaning the porous silicon waveguide sample surface, e.g., by blowing with nitrogen gas, to remove any dust should help coupling and find the resonance. The prism should also be cleaned periodically with Opto-Wipes lens cleaning paper to remove any particles on the prism surface that can affect coupling.
11. Optimize the resonance so that it is deeper and sharper according to the manual.
12. Uncouple the sample by deactivating the coupling pressure, and take it out using a tweezer. Hold the sample steady without touching the prism to avoid scratching the sample and damaging the prism.
13. After finishing all measurements, to avoid referencing the table next time, click the "Parameters" form and let it remain on the screen before turning off the control box. Next time, turn on the control box and click "Ok" on the parameters form, and the prism coupler is ready for use without referencing again.
14. The lasers should be kept on if experiments are expected for the same day. After finishing all experiments and before leaving the lab for the day, the lasers and the control box should be turned off. In this way, the lasers can have extended life time.

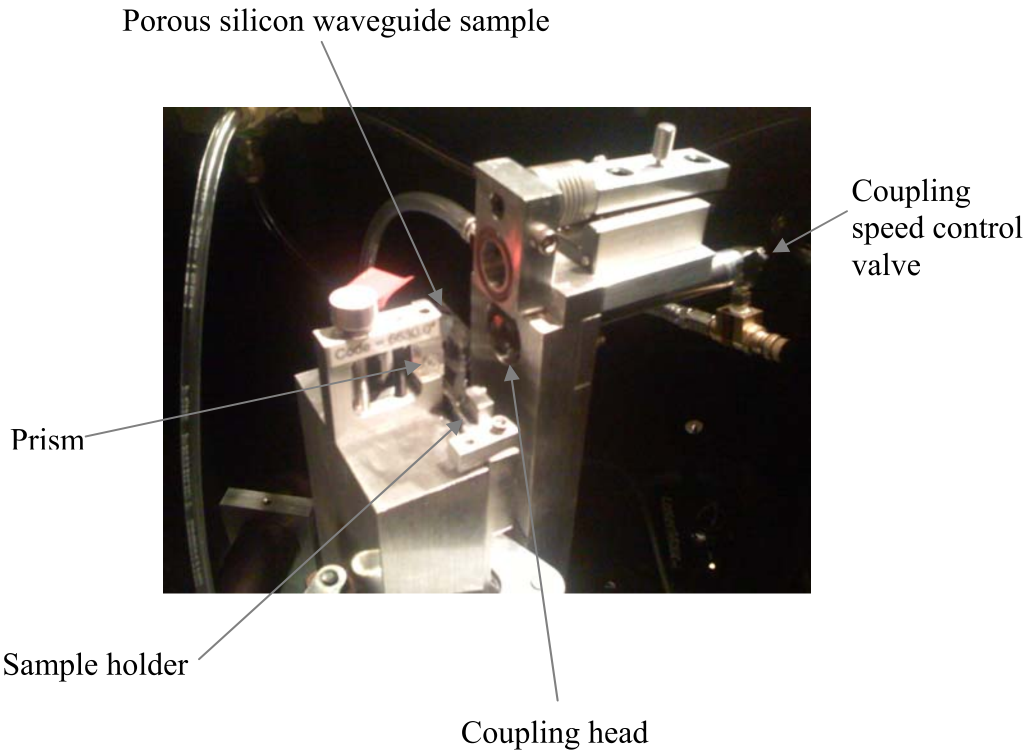

Figure C.1. Setup inside the prism coupler.

APPENDIX D

WAVEGUIDE REFLECTANCE VS. ANGLE CALCULATION CODE

```
close all;
clear all;
load lambdas.m      % loading necessary wavelength and corresponding
index of refraction
load indicies.m     % data of silicon for use later in spline
interpolation in find_neff function
% load N-PSi-Formvar-WG-Exp-Refl
LP=.4;                    % porosity of waveguide layer
HP=.76;                    % porosity of coupling layer
fill=0;                     % liquid crystal fill factor, should be
fixed at 0, this factor exists to be compatible with find_neff()
pore_index=1;               % XXXXXXXXXrefractive index of air pore,
should be 1
delta_Si_index=0*-1.77;        % Si index decrease due to oxidation
adjust=0*1.5;  % adjustment of index change for low porosity layer
because of less oxidation
delta_pore_index=0*0.01;       % refractive index of air pore change
due to DNA infiltration, 10uM -> 0.01, 1000uM ->0.1
lambda=1550;                 % beam wavelength in nm
k0=2*pi/lambda;
c=3e17;                      % speed of light in nm/sec
eps0=8.854e-21;              % epsilon0 in term of F/nm
mu0=1/(eps0*c^2);
n_prism=2.1252;
n_air=1;                          %XXXXXXXXXXX refractive index of air,
which is above the waveguide layer
n_film=find_neff(lambda/1000,LP,lambdas,indicies+delta_Si_index,fill,po
re_index);%2.167533;
%effective refractive index of upper layer
n_film=2.0+0.002*i;%n_film(1)
n_clad=find_neff(lambda/1000,HP,lambdas,indicies+delta_Si_index,fill,po
re_index);%1.618755,1.524149,1.402795,75%,80%,85%,;%effective
refractive index of lower layer
n_clad=1.5;%n_clad(1)
n_sub=3.4784;%+0.00001234*i;
%n0=n2;
theta_d=32:0.01:65;         %internal (inside prism) angle range( in
degree)
theta=theta_d/180*pi;      %convert angle to radians

%Effective index and wave-vector that is parallel to the interfaces
n_eff=n_prism*sin(theta);
beta=n_eff*k0;

%Wave-vectors in the medium that are perpendicular to the interfaces
gamma_p=sqrt(n_prism^2-n_eff.^2);   % in prism
gamma_a=sqrt(n_air^2-n_eff.^2);     % in air
gamma_f=sqrt(n_film^2-n_eff.^2);    % in film, or waveguiding layer
gamma_c=sqrt(n_clad^2-n_eff.^2);    % in cladding layer, or buffer
layer
gamma_s=sqrt(n_sub^2-n_eff.^2);     % in substrate layer, which is Si

%Transmission coefficients through air/prism and prism/air interfaces.
t_ap=2*gamma_a./(gamma_a+gamma_p);
t_pa=2*gamma_p./(gamma_a+gamma_p);
```

```
T_ap=sqrt(n_prism^2-
(n_air*sin(theta)).^2)./(n_air*cos(theta)).*abs(t_ap).^2;
T_pa=n_air*cos(theta)./sqrt(n_prism^2-
(n_air*sin(theta)).^2).*abs(t_pa).^2;

%Thickness of medium and phase changes
d_air=750;
d_film=1000;
d_clad=1500;
phi_a=d_air*k0*gamma_a;
phi_f=d_film*k0*gamma_f;
phi_c=d_clad*k0*gamma_c;

%Transfer matrix for each layer of medium and the total transfer matrix,
%from which the reflection can be calculated.
for j=1:size(theta,2)
    Ma=[cos(phi_a(j)) -i*sin(phi_a(j))/gamma_a(j);-
i*gamma_a(j)*sin(phi_a(j)) cos(phi_a(j))];
    Mf=[cos(phi_f(j)) -i*sin(phi_f(j))/gamma_f(j);-
i*gamma_f(j)*sin(phi_f(j)) cos(phi_f(j))];
    Mc=[cos(phi_c(j)) -i*sin(phi_c(j))/gamma_c(j);-
i*gamma_c(j)*sin(phi_c(j)) cos(phi_c(j))];
    M=Ma*Mf*Mc;
    R(j)=abs(((M(1)+M(2)*gamma_s(j))*gamma_p(j)-M(3)-
M(4)*gamma_s(j))/((M(1)+M(2)*gamma_s(j))*gamma_p(j)+M(3)+M(4)*gamma_s(j
)))^2;
end

%Plot reflection vs. angle
figure;
plot(theta_d,R);
xlabel('Incidence Angle at Prism Base (degrees)');
ylabel('Reflection');
title('Reflection of Waveguide Structure');

%Include transmission through air/prism and prism/air interfaces, and
plot
R_total=T_ap.*R.*T_pa;
figure;
plot(theta_d,R_total);
%xlabel('Incidence Angle at Prism Base (degrees)');
%ylabel('Reflection');
%title('Reflection including prism effect');



% The following calculates the total number of modes for the give
indices
% and thicknesses. The angles and effective indices of each mode are
also
% given.

% Phase shifts at the two interfaces
theta_f=asin(n_prism*sin(theta)/n_film); % convert angle to inside
waveguiding layer
```

```
PHI12=atan((sqrt((n_film*sin(theta_f)).^2-
n_clad^2)./(n_film*cos(theta_f))));  %phase change at interface between
medium 1 and 2
PHI10=atan((sqrt((n_film*sin(theta_f)).^2-
n_air^2)./(n_film*cos(theta_f))));  %phase change at interface between
medium 1 and 0
i=0;
thick=0;
res_ang=0;
while ((thick<=d_film)&isreal(thick))
    w=(PHI10+PHI12+i*pi)./(k0*n_film*cos(theta));
    position=find(abs(d_film-w)==min(abs(d_film-w)));
    if w(position)>d_film,
        position=position-1;
    else
    end
    thick=w(position); %#ok<AGROW>
    if ((thick<=d_film)&isreal(thick)),
        res_ang(i+1)=theta_d(position);
    else
    end
    i=i+1;
end
res_ang   %This gives the number of modes and the angles that
correspond to each mode, starting from the 0th mode.
effective_index=n_prism*sin(res_ang/180*pi)           %This gives the
effective indicies of the modes, starting from the 0th mode.
```

APPENDIX E

WAVEGUIDE MODE FIELD CALUCULATION CODE

```
clear all;
close all;
load lambdas.m      % loading necessary wavelength and corresponding
index of refraction
load indicies.m     % data of silicon for use later in spline
interpolation in find_neff function
LP=0.547;                    % porosity of waveguide layer
HP=0.723;                    % porosity of coupling layer
fill=0;                     % liquid crystal fill factor, should be
fixed at 0, this factor exists to be compatible with find_neff()
%pore_index=1;               % XXXXXXXXXrefractive index of air pore,
should be 1
delta_Si_index=0*-1.77;        % Si index decrease due to oxidation
adjust=0*1.5;  % adjustment of index change for low porosity layer
because of less oxidation
delta_pore_index=0*0.01;       % refractive index of air pore change
due to DNA infiltration, 10uM -> 0.01, 1000uM ->0.1
lambda=1550;                 % beam wavelength
c=3e17;                      % speed of light in nm/sec
eps0=8.854e-21;              % epsilon0 in term of F/nm
mu0=1/(eps0*c^2);
prism_index=2.1252;
n0=1.0;                         %XXXXXXXXXXXX refractive index of air,
which is above the waveguide layer
pore_index=1.0;
n1=find_neff(lambda/1000,LP,lambdas,indicies+delta_Si_index,fill,pore_i
ndex);%2.167533;
%effective refractive index of upper layer
n1=n1(1)
n2=find_neff(lambda/1000,HP,lambdas,indicies+delta_Si_index,fill,pore_i
ndex);%1.618755,1.524149,1.402795,75%,80%,85%,;%effective refractive
index of lower layer
n2=n2(1)
%n0=n2;
theta_d=0.01:0.01:89.99;         %internal (inside prism) angle
range( in degree)
theta=theta_d/180*pi;      %convert angle to radians
theta1=asin(prism_index*sin(theta)/n1); %convert to angle in the
waveguding layer by Snell's law
PHI12=atan((sqrt((n1*sin(theta1)).^2-n2^2)./(n1*cos(theta1))));  %phase
change at interface between medium 1 and 2
PHI10=atan((sqrt((n1*sin(theta1)).^2-n0^2)./(n1*cos(theta1))));  %phase
change at interface between medium 1 and 0
k=2*pi/lambda;             %wave vector in vacuum
w=(PHI10+PHI12+1*pi)./(k*n1*cos(theta1));  %calcuate upper layer
thicknesses corresponding to different mode angles (first mode m=0)
%time=w/5;                  %etching time, given etching rate of
5nm/sec at 5mA/cm2
%theta_prism=asin(n1*sin(theta)/prism_index);
%res_ang=theta_prism/pi*180;
%figure;
%plot(w,res_ang);    %plot etching time versus mode angle

thick=1000;          % thickness of waveguiding layer
position=find(abs(w-thick)==min(abs(w-thick)));
thick_correct_TE=w(position)
if abs(w(position)-thick)>10
```

```
    warning('Calculated effective index of the TE mode may not the true
value, check the prism index');
end

res_ang_original=theta_d(position)
n_eff_wg=prism_index*sin(res_ang_original/180*pi)

h=k*sqrt(n1^2-n_eff_wg^2);  %            Z axis
q=k*sqrt(n_eff_wg^2-n0^2);  %           /|\
p=k*sqrt(n_eff_wg^2-n2^2);  %            |
xmin=0;                     %            |
xmax=4000;                  %            |air
del_x=10;                   %      z=0   |------------------>X axis
x=xmin:del_x:xmax;          %            |waveguiding layer
zmin=-2000;                 %  z=-thick  |-------------------
zmax=2000;                  %            |cladding layer
del_z=0.01*100;              %            |
z1=0:del_z:zmax;            %            |
z2=-(thick):del_z:-del_z;   %            |
z3=zmin:del_z:-(thick+del_z);
z=cat(2,z3,z2,z1);
E1=exp(-z1*q);
E2=cos(h*z2)-(q/h)*sin(h*z2);
E3=(cos(h*abs(min(z2)))+(q/h)*sin(h*abs(min(z2))))*exp(p*(z3-min(z2)));
E=cat(2,E3,E2,E1);

%Normalized the field by a constant C so that total power is 1 watt
%C=1/max(E); %normalized so that the peak filed amplitude is 1
%C=1/sqrt(sum(E.^2*del_z)) %normalize so that the denominator of equ(10)
is 1 (in Biosens. Bioelectron.6(1991)215-225, W. Lukosz).
C=2*h*sqrt(k*c*mu0/(n_eff_wg*k*(thick+1/q+1/p)*(h^2+q^2))) %normalize
so
%that 1 watt flow in waveguide progagation direction per unit width in
y
%direction
E_normalized=E*C;
%sum_TE=k*n_eff_wg/(2*k*c*mu0)*sum(E_normalized.^2)*del_z %check if
normalized
%sum_TE=sum(E_normalized.^2*del_z)   %check if normalized
figure;
plot(z,E_normalized)
xlabel('Vertical Direction');
ylabel('Normalized Field Amplitude');
title('Total Electric Field for TE Mode');
%----------------------------------------------------------------------
----
%The following section is TM waveguide mode
%----------------------------------------------------------------------
----
%n0=1.32;
%n1=3.474;
%n2=1.444;
PHI12_TM=atan((n1^2*sqrt((n1*sin(theta1)).^2-
n2^2)./(n2^2*n1*cos(theta1))));  %phase change for TM modes at
interface between medium 1 and 2
```

```
PHI10_TM=atan((n1^2*sqrt((n1*sin(theta1)).^2-
n0^2)./(n0^2*n1*cos(theta1))));  %phase change for TM modes at
interface between medium 1 and 0
w=(PHI10_TM+PHI12_TM)./(k*n1*cos(theta1));  %calcuate upper layer
thicknesses corresponding to different mode angles (first mode m=0)
%thick=260;
position_TM=find(abs(w-thick)==min(abs(w-thick)));
thick_correct_TM=w(position_TM)
if abs(w(position_TM)-thick)>10
    warning('Calculated effective index of the TM mode may not the true
value, check the prism index');
end
res_ang_original_TM=theta_d(position_TM)
n_eff_wg_TM=prism_index*sin(res_ang_original_TM/180*pi)

h=k*sqrt(n1^2-n_eff_wg_TM^2);
q=k*sqrt(n_eff_wg_TM^2-n0^2);
p=k*sqrt(n_eff_wg_TM^2-n2^2);
q1=n1^2/n0^2*q;
p1=n1^2/n2^2*p;
%xmin=0;
%xmax=4000;
%del_x=10;
%x=xmin:del_x:xmax;
%zmin=-2000;
%zmax=2000;
%del_z=0.01*100;
%z1=0:del_z:zmax;
%z2=-(thick):del_z:-del_z;
%z3=zmin:del_z:-(thick+del_z);
%z=cat(2,z3,z2,z1);
H1_TM=-h/q1*exp(-z1*q);
H2_TM=-h/q1*cos(h*z2)+sin(h*z2);
H3_TM=-(h/q1*cos(h*abs(min(z2)))+sin(h*thick))*exp(p*(z3-min(z2)));
H_TM=cat(2,H3_TM,H2_TM,H1_TM);

epsilon1=eps0*n0^2*ones(1,length(z1));
epsilon2=eps0*n1^2*ones(1,length(z2));
epsilon3=eps0*n2^2*ones(1,length(z3));
epsilon=cat(2,epsilon3,epsilon2,epsilon1);
Ez_TM=n_eff_wg_TM./(k*c*epsilon).*H_TM;
dHdz_origin=diff(H_TM)/del_z;
dHdz=[dHdz_origin,dHdz_origin(size(dHdz_origin,2))];
Ex_TM=-sqrt(-1)./(k*c*epsilon).*dHdz;

%normalize field amplitude by a constant C so that total power is 1
watt
teff=(q1^2+h^2)/q1^2*(thick/n1^2+(q^2+h^2)/(q1*2+h^2)/(n0^2*q)+(p^2+h^2
)/(p1^2+h^2)/(n2^2*p));
C_TM=1/sqrt(sum(H_TM.^2*eps0./epsilon*del_z)) %normalize so that the
denominator of equ(11) is 1 (in Biosens. Bioelectron.6(1991)215-225, W.
Lukosz).
%C_TM=2*sqrt(k*c*eps0/(n_eff_wg_TM*k*teff)) %normalize so that 1 watt
flow in waveguide progagation direction per unit width in y direction
H_TM_normalized=H_TM*C_TM;
Ez_TM_normalized=Ez_TM*C_TM;
```

```
Ex_TM_normalized=Ex_TM*C_TM;
Etotal_TM_normalized=sqrt(abs(Ez_TM_normalized).^2+abs(Ex_TM_normalized
).^2);
Etotal_TM_normalized=Etotal_TM_normalized/max(Etotal_TM_normalized);
figure;
plot(z,Ez_TM_normalized);
xlabel('Vertical Direction');
ylabel('Normalized Field Amplitude');
title('Perpendicular Component of Electric Field for TM Mode');
figure;
plot(z,Etotal_TM_normalized);
xlabel('Vertical Direction');
ylabel('Normalized Field Amplitude');
title('Total Electric Field for TM Mode');
%n_eff_wg_TM*k/(2*k*c)*sum((H_TM_normalized).^2./epsilon*del_z)
%sum_TM=k*n_eff_wg_TM/(2*k*c*mu0)*sum(Etotal_TM_normalized.^2)*del_z
%check if
%normailzed
sum_TM=sum(H_TM_normalized.^2*eps0./epsilon*del_z) %check if normalized

%the following calcualtes shift of Neff for the TM waveguide mode due
to addlayer of 4 nm and n=1.5
%on the waveguide cover
DNA_size=4;
DNA_index=1.5;
epsilon_r=epsilon/eps0;
del_epsilon_r=zeros(1,length(z));
del_epsilon_r(find((z>=0)&(z<=DNA_size)))=DNA_index^2-n0^2;
del_inv_epsilon_r=del_epsilon_r./epsilon_r.^2;
del_N2=(1/k^2*sum(del_epsilon_r./epsilon_r.^2.*dHdz.^2*del_z)+n_eff_wg_
TM^2*sum(del_inv_epsilon_r.*H_TM.^2*del_z))/sum(H_TM.^2./epsilon_r*del_
z);
del_N=del_N2/(2*n_eff_wg_TM)
```

APPENDIX F

SPR MODE FIELD CALUCULATION CODE

```
close all;
clear all;
%The following calculates the H-field distribution for SPR sensor
%n_metal=0.462+9.2*i;
i=sqrt(-1);
n0=1;                 % for SPR, buffer solution is on top
lambda=633;
k=2*pi/lambda;
if lambda==633,
eps_metal=-11.8+1.2*i;%(0.56+11.21*i)^2; % Here we use epsilon of gold
at 632.8nm. n_metal^2;
elseif lambda==1550,
  eps_metal=(0.56+11.21*i)^2;   %epsilon of gold at 1610nm
end
n_eff_spr=1/sqrt(1/n0^2+1/real(eps_metal));
c=3e17;                      % speed of light in nm/sec
eps0=8.854e-21;              % epsilon0 in term of F/nm
%res_ang_spr=asin(n_eff_spr/prism_index)/pi*180;
depth_diel=lambda/((2*pi)*sqrt(n_eff_spr^2-n0^2));
depth_metal=depth_diel*n0^2/(-real(eps_metal));
thick_metal=40;       % metal film, either gold or silver, is only 40
nm
zzmin=-thick_metal;
zzmax=4000;
del_zz=0.01*100;
zz1=del_zz:del_zz:zzmax;
zz2=-(thick_metal):del_zz:0;
zz=cat(2,zz2,zz1);
AA1=exp(-zz1/depth_diel); %AA1 is the H field of the SPR TM mode in
dielectricl region
EEx1=n_eff_spr*AA1/(c*eps0*n0^2);
dH1dz_origin=diff(AA1)/del_zz;
dH1dz=[dH1dz_origin,dH1dz_origin(size(dH1dz_origin,2))];
EEz1=dH1dz/(eps0*n0^2*c*k);
%EE1=EEx1/sin(
AA2=exp(zz2/depth_metal);%AA2 is the H field of the SPR TM mode in
metal region
AA=cat(2,AA2,AA1); %AA is the H field of the SPR TM mode
EEx2=n_eff_spr*AA2/(c*eps0*real(eps_metal));
dH2dz_origin=diff(AA2)/del_zz;
dH2dz=[dH2dz_origin,dH2dz_origin(size(dH2dz_origin,2))];
EEz2=dH2dz/(real(eps_metal)*eps0*c*k);
EEx=cat(2,EEx2,EEx1);
EEz=cat(2,EEz2,EEz1);
E_spr=(EEx.^2+EEz.^2).^0.5;
p=sqrt(-real(eps_metal)^2/(n0^2+real(eps_metal)))*k;  % p is alo
1/depth_methal;
q=sqrt(-n0^4/(n0^2+real(eps_metal)))*k; %q is also 1/depth_diel
C_SPR=sqrt(4*k*c*eps0/(k*n_eff_spr)/(1/(q*n0^2)+1/(p*real(eps_metal))));
%normalization constant for SPR field so that 1 watt per y unit width
of power propagating in z direction
E_spr_normalized=E_spr*C_SPR;%E_spr/sqrt(sum(E_spr.^2)*del_zz);%normali
ze in terms of power
figure;
plot(zz,E_spr_normalized);
H_spr_normalized=AA*C_SPR;
epsilon1=eps0*n0^2*ones(1,length(zz1));
```

```
epsilon2=eps0*real(eps_metal)*ones(1,length(zz2));
epsilon=cat(2,epsilon1,epsilon2);
n_eff_spr*k/(2*k*c)*sum((H_spr_normalized).^2./epsilon*del_zz)
%E_spr_normal=E_spr/max(E_spr);  % normalize in terms of peak field
Ex_spr=EEx/sqrt(sum(E_spr.^2)*del_zz);
Ez_spr=EEz/sqrt(sum(E_spr.^2)*del_zz);
```

APPENDIX G

INCUBATION PROCEDURE

Incubation Procedure

1. Take a large plastic Petri dish as the incubation container. Spread 10-15 mL DI water around in it to create a humid environment. Kimwipes can also be used to hold the water in the container (Figure G.1). In some circumstances, ethanol is used in the solution for incubation. In such cases, it is better to spread ethanol in the Petri dish as well.
2. Put the large Petri dish in the chemical hood. All incubation, rinsing and drying procedures described below should be carried out inside the chemical hood.
3. Use the cover of a smaller plastic Petri dish to act as the platform for holding samples. Using a tweezer, put porous silicon waveguide samples on the flat surface of the platform. They should not be tilted such that solutions of buffer, DI water and ethanol do not flow to one side after being dropped onto the sample surface. Also, the spacing between samples should be large enough to allow easy grabbing of the samples by a tweezer.
4. Drop the biomolecular solution onto the porous silicon waveguide sample surface. The volume of solution should be enough to cover the porous silicon waveguide active area. For the p-type porous silicon waveguide of 2 cm^2, 100 μL is sufficient. For the n-type porous silicon membrane waveguide, 20 μL is sufficient.
5. Put the cover back on top of the large Petri dish. Incubate for time duration as specified by the protocol. Use a timer for keeping track of the incubation timing.
6. After the specified incubation duration, open the large Petri dish and take out the porous silicon waveguide samples one at a time. Rinse the samples with the appropriate solvent (buffer, DI water, ethanol, etc), and dry with nitrogen gas.
7. Clean the large and small Petri dishes by DI water and dry them in air.

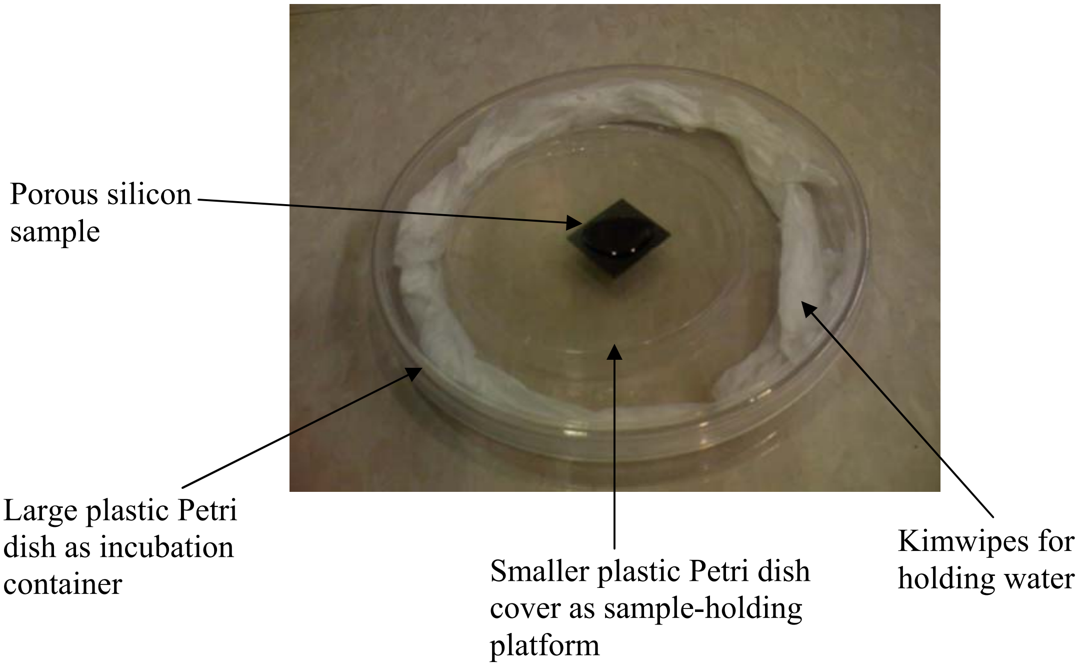

Figure G.1. Setup for incubation of porous silicon sample in biomolecular solution.

REFERENCES

1. Cooper, M.A., *Label-free screening of bio-molecular interactions.* Analytical and Bioanalytical Chemistry, 2003. **377**(5): p. 834-842.

2. Aebersold, R. and M. Mann, *Mass spectrometry-based proteomics.* Nature, 2003. **422**(6928): p. 198-207.

3. Ivnitski, D., I. Abdel-Hamid, P. Atanasov, and E. Wilkins, *Biosensors for detection of pathogenic bacteria.* Biosensors & Bioelectronics, 1999. **14**(7): p. 599-624.

4. Berney, H., J. West, E. Haefele, J. Alderman, W. Lane, and J.K. Collins, *A DNA diagnostic biosensor: development, characterisation and performance.* Sensors and Actuators B-Chemical, 2000. **68**(1-3): p. 100-108.

5. Kindschy, L.M. and E.C. Alocilja, *A review of molecularly imprinted polymers for biosensor development for food and agricultural applications.* Transactions of the Asae, 2004. **47**(4): p. 1375-1382.

6. Ince, R. and R. Narayanaswamy, *Analysis of the performance of interferometry, surface plasmon resonance and luminescence as biosensors and chemosensors.* Analytica Chimica Acta, 2006. **569**(1-2): p. 1-20.

7. Chen, J.R., Y.Q. Miao, N.Y. He, X.H. Wu, and S.J. Li, *Nanotechnology and biosensors.* Biotechnology Advances, 2004. **22**(7): p. 505-518.

8. Grodzinski, P., M. Silver, and L.K. Molnar, *Nanotechnology for cancer diagnostics: promises and challenges.* Expert Review of Molecular Diagnostics, 2006. **6**(3): p. 307-318.

9. Wee, K.W., G.Y. Kang, J. Park, J.Y. Kang, D.S. Yoon, J.H. Park, and T.S. Kim, *Novel electrical detection of label-free disease marker proteins using piezoresistive self-sensing micro-cantilevers.* Biosensors & Bioelectronics, 2005. **20**(10): p. 1932-1938.

10. Gao, Z.Q., A. Agarwal, A.D. Trigg, N. Singh, C. Fang, C.H. Tung, Y. Fan, K.D. Buddharaju, and J.M. Kong, *Silicon nanowire arrays for label-free detection of DNA.* Analytical Chemistry, 2007. **79**(9): p. 3291-3297.

11. Yun, Y.H., A. Bange, V.N. Shanov, W.R. Heineman, H.B. Halsall, Z.Y. Dong, A. Jazieh, Y. Tu, D. Wong, S. Pixley, M. Behbehani, and M.J. Schulz, *A carbon nanotube needle biosensor.* Journal of Nanoscience and Nanotechnology, 2007. **7**(7): p. 2293-2300.

12. Nath, N. and A. Chilkoti, *Label free colorimetric biosensing using nanoparticles.* Journal of Fluorescence, 2004. **14**(4): p. 377-389.

13. Sapsford, K.E., T. Pons, I.L. Medintz, and H. Mattoussi, *Biosensing with luminescent semiconductor quantum dots.* Sensors, 2006. **6**(8): p. 925-953.

14. Chen, Z.Z., N. Zhang, W.S. Zhang, and B. Tang, *Progresses and applications of protein fluorescent probes.* Chinese Journal of Analytical Chemistry, 2006. **34**(9): p. 1341-1347.

15. Tahtouh, M., J.R. Kalman, C. Roux, C.I. Lennard, and B.J. Reedy, *The detection and enhancement of latent fingermarks using infrared chemical imaging.* Journal of Forensic Sciences, 2005. **50**(1): p. 64-72.

16. Fischer, B.M., H. Helm, and P.U. Jepsen, *Chemical recognition with broadband THz spectroscopy.* Proceedings of the IEEE, 2007. **95**(8): p. 1592-1604.

17. Homola, J., *Present and future of surface plasmon resonance biosensors.* Analytical and Bioanalytical Chemistry, 2003. **377**(3): p. 528-539.

18. Phillips, K.S. and Q. Cheng, *Recent advances in surface plasmon resonance based techniques for bioanalysis.* Analytical and Bioanalytical Chemistry, 2007. **387**(5): p. 1831-1840.

19. Homola, J., S.S. Yee, and G. Gauglitz, *Surface plasmon resonance sensors: review.* Sensors and Actuators B-Chemical, 1999. **54**(1-2): p. 3-15.

20. Ferguson, J.A., T.C. Boles, C.P. Adams, and D.R. Walt, *A fiber-optic DNA biosensor microarray for the analysis of gene expression.* Nature Biotechnology, 1996. **14**(13): p. 1681-1684.

21. Bosch, M.E., A.J.R. Sanchez, F.S. Rojas, and C.B. Ojeda, *Recent development in optical fiber biosensors.* Sensors, 2007. **7**(6): p. 797-859.

22. Potyrailo, R.A., S.E. Hobbs, and G.M. Hieftje, *Optical waveguide sensors in analytical chemistry: today's instrumentation, applications and trends for future development.* Fresenius Journal of Analytical Chemistry, 1998. **362**(4): p. 349-373.

23. Blair, S., Chen, Y., *Resonant-enhanced evanescent-wave fluorescence biosensing with cylindrical optical cavities.* Applied Optics, 2001 **40**(4): p. 570-582.

24. Boyd, R. W., Heebner, J. E., *Sensitive Disk Resonator Photonic Biosensor.* Applied Optics, 2001 **40**(31): p. 5742-5747.

25. Densmore, A., D.X. Xu, P. Waldron, S. Janz, P. Cheben, J. Lapointe, A. Delage, B. Lamontagne, J.H. Schmid, and E. Post, *A silicon-on-insulator photonic wire*

based evanescent field sensor. IEEE Photonics Technology Letters, 2006. **18**(21-24): p. 2520-2522.

26. Taylor, H.F. and A. Yariv, *Guided Wave Optics*. Proceedings of the IEEE, 1974. **62**(8): p. 1044-1060.

27. Maccraith, B.D., *Enhanced Evanescent Wave Sensors Based on Sol Gel-Derived Porous-Glass Coatings*. Sensors and Actuators B-Chemical, 1993. **11**(1-3): p. 29-34.

28. Maccraith, B.D., C.M. Mcdonagh, G. Okeeffe, A.K. Mcevoy, T. Butler, and F.R. Sheridan, *Sol-Gel Coatings for Optical Chemical Sensors and Biosensors*. Sensors and Actuators B-Chemical, 1995. **29**(1-3): p. 51-57.

29. Oh, S., J. Moon, T. Kang, S. Hong, and J. Yi, *Enhancement of surface plasmon resonance (SPR) signals using organic functionalized mesoporous silica on a gold film*. Sensors and Actuators B-Chemical, 2006. **114**(2): p. 1096-1099.

30. Koutsioubas, A.G., N. Spiliopoulos, D. Anastassopoulos, A.A. Vradis, and G.D. Priftis, *Nanoporous alumina enhanced surface plasmon resonance sensors*. Journal of Applied Physics, 2008. **103**(9): p. 094521-1-6.

31. Cloutier, S.G., A.D. Lazareck, and J. Xu, *Detection of nano-confined DNA using surface-plasmon enhanced fluorescence*. Applied Physics Letters, 2006. **88**(1): p. 013904-1-3.

32. Qi, Z.M., I. Honma, and H.S. Zhou, *Nanoporous leaky waveguide based chemical and biological sensors with broadband spectroscopy*. Applied Physics Letters, 2007. **90**(1): p. 011102 1-2.

33. Awazu, K., C. Rockstuhl, M. Fujimaki, N. Fukuda, J. Tominaga, T. Komatsubara, T. Ikeda, and Y. Ohki, *High sensitivity sensors made of perforated waveguides*. Optics Express, 2007. **15**(5): p. 2592-2597.

34. Chan, S., P.M. Fauchet, Y. Li, L.J. Rothberg, and B.L. Miller, *Porous silicon microcavities for biosensing applications*. Physica Status Solidi a-Applied Research, 2000. **182**(1): p. 541-546.

35. Chan, S., S.R. Horner, P.M. Fauchet, and B.L. Miller, *Identification of gram negative bacteria using nanoscale silicon microcavities*. Journal of the American Chemical Society, 2001. **123**(47): p. 11797-11798.

36. Ouyang, H., M. Christophersen, R. Viard, B.L. Miller, and P.M. Fauchet, *Macroporous silicon microcavities for macromolecule detection*. Advanced Functional Materials, 2005. **15**(11): p. 1851-1859.

37. Ouyang, H., C.C. Striemer, and P.M. Fauchet, *Quantitative analysis of the sensitivity of porous silicon optical biosensors.* Applied Physics Letters, 2006. **88**(16): p. 163108-1-3.

38. Stewart, M.P. and J.M. Buriak, *Chemical and biological applications of porous silicon technology.* Advanced Materials, 2000. **12**(12): p. 859-869.

39. Stewart, M.P., E.G. Robins, T.W. Geders, M.J. Allen, H.C. Choi, and J.M. Buriak, *Three methods for stabilization and functionalization of porous silicon surfaces via hydrosilylation and electrografting reactions.* Physica Status Solidi a-Applied Research, 2000. **182**(1): p. 109-115.

40. Lin, V.S.-Y., K. Motesharei, K.P.S. Dancil, M.J. Sailor, and M.R. Ghadiri, *A porous silicon-based optical interferometric biosensor.* Science, 1997. **278**(5339): p. 840-843.

41. Narayan, R.J., C.M. Jin, N. Menegazzo, B. Mizaikoff, R.A. Gerhardt, M. Andara, A. Agarwal, C.C. Shih, C.M. Shih, S.J. Lin, and Y.Y. Su, *Nanoporous hard carbon membranes for medical applications.* Journal of Nanoscience and Nanotechnology, 2007. **7**(4-5): p. 1486-1493.

42. Caro, J., *Zeolites and mesoporous materials as advanced functional material.* Recent Advances in the Science and Technology of Zeolites and Related Materials, Pts a - C, 2004. **154**: p. 80-93.

43. Xavier, M.P., B. Vallejo, M.D. Marazuela, M.C. Moreno-Bondi, F. Baldini, and A. Falai, *Fiber optic monitoring of carbamate pesticides using porous glass with covalently bound chlorophenol red.* Biosensors & Bioelectronics, 2000. **14**(12): p. 895-905.

44. Canham, L., *Properties of Porous Silicon* ed. L. Canham. 1997, DERA, Malvern, UK: Institution of Engineering and Technology.

45. Lehmann, V., *Electrochemistry of silicon: instrumentation, science, materials and applications*. 2002, Weinheim, Germany: Wiley-VCH.

46. Pacholski, C., M. Sartor, M.J. Sailor, F. Cunin, and G.M. Miskelly, *Biosensing using porous silicon double-layer interferometers: Reflective interferometric Fourier transform spectroscopy.* Journal of the American Chemical Society, 2005. **127**(33): p. 11636-11645.

47. Vazsonyi, E., E. Szilagyi, P. Petrik, Z.E. Horvath, T. Lohner, M. Fried, and G. Jalsovszky, *Porous silicon formation by stain etching.* Thin Solid Films, 2001. **388**(1-2): p. 295-302.

48. Laiho, R. and A. Pavlov, *Preparation of Porous Silicon Films by Laser-Ablation.* Thin Solid Films, 1995. **255**(1-2): p. 9-11.

49. Beale, M.I.J., N.G. Chew, M.J. Uren, A.G. Cullis, and J.D. Benjamin, *Microstructure and Formation Mechanism of Porous Silicon.* Applied Physics Letters, 1985. **46**(1): p. 86-88.

50. Lehmann, V. and U. Gosele, *Porous Silicon Formation - a Quantum Wire Effect.* Applied Physics Letters, 1991. **58**(8): p. 856-858.

51. Smith, R.L. and S.D. Collins, *Porous Silicon Formation Mechanisms.* Journal of Applied Physics, 1992. **71**(8): p. R1-R22.

52. Bruggeman, D.A.G., *Berechnung Verschiedener Physikalischer Konstanten von Heterogenen Substanzen.* Annalen der Physik (Leipzig), 1935. **24**: p. 636-679.

53. Garnett, J.C.M., *Colours in metal glasses and in metallic films.* Philosophical Transactions of the Royal Society of London, 1904. **203**: p. 385-402.

54. Looyenga, H., *Dielectric constants of heterogeneous mixtures.* Physica, 1965. **31**: p. 401-406.

55. Lugo, J.E., H.A. Lopez, S. Chan, and P.M. Fauchet, *Porous silicon multilayer structures: A photonic band gap analysis.* Journal of Applied Physics, 2002. **91**(8): p. 4966-4972.

56. J. J. Saarinen, S.M.W., P. M. Fauchet, and J. E. Sipe, *Reflectance analysis of a multilayer 1-D porous silicon structure: theory and experiment.* Journal of Applied Physics, 2008. **104**: p. 013103-1-7.

57. Lazarouk, S., P. Jaguiro, and V. Borisenko, *Integrated optoelectronic unit based on porous silicon.* Physica Status Solidi a-Applied Research, 1998. **165**(1): p. 87-90.

58. Vincent, G., *Optical-Properties of Porous Silicon Superlattices.* Applied Physics Letters, 1994. **64**(18): p. 2367-2369.

59. Araki, M., H. Koyama, and N. Koshida, *Optical cavity based on porous silicon superlattice technology.* Japanese Journal of Applied Physics Part 1-Regular Papers Short Notes & Review Papers, 1996. **35**(2B): p. 1041-1044.

60. Thonissen, M., M.G. Berger, W. Theiss, S. Hilbrich, M. Kruger, and H. Luth, *The colourful world of porous silicon: From interference filters to applications.* Solid State Phenomena, 1997. **54**: p. 65-72.

61. Kordas, K., S. Beke, A.E. Pap, A. Uusimaki, and S. Leppavuori, *Optical properties of porous silicon. Part II: Fabrication and investigation of multilayer structures.* Optical Materials, 2004. **25**(3): p. 257-260.

62. Pirasteh, P., J. Charrier, A. Soltani, S. Haesaert, L. Haji, C. Godon, and N. Errien, *The effect of oxidation on physical properties of porous silicon layers for optical applications.* Applied Surface Science, 2006. **253**(4): p. 1999-2002.

63. Salonen, J. and V.P. Lehto, *Fabrication and chemical surface modification of mesoporous silicon for biomedical applications.* Chemical Engineering Journal, 2008. **137**(1): p. 162-172.

64. Jelinek, I., T. Chvojka, V. Vrkoslav, J. Jindrich, M. Lorenc, D. Niznansky, I. Nemec, V. Kral, and J. Dian, *Nanostructured porous silicon - Optical properties, surface modification and sensor applications.* Chimia, 2005. **59**(5): p. 222-225.

65. Zhu, Z.Q., J. Zhang, and J.Z. Zhu, *An overview of Si-based biosensors.* Sensor Letters, 2005. **3**(2): p. 71-88.

66. Schwartz, M.P., C. Yu, S.D. Alvarez, B. Migliori, D. Godin, L. Chao, and M.J. Sailor, *Using an oxidized porous silicon interferometer for determination of relative protein binding affinity through non-covalent capture probe immobilization.* Physica Status Solidi a-Applications and Materials Science, 2007. **204**(5): p. 1444-1448.

67. Dancil, K.P.S., D.P. Greiner, and M.J. Sailor, *A porous silicon optical biosensor: Detection of reversible binding of IgG to a protein A-modified surface.* Journal of the American Chemical Society, 1999. **121**(34): p. 7925-7930.

68. Janshoff, A., K.P.S. Dancil, C. Steinem, D.P. Greiner, V.S.Y. Lin, C. Gurtner, K. Motesharei, M.J. Sailor, and M.R. Ghadiri, *Macroporous p-type silicon Fabry-Perot layers. Fabrication, characterization, and applications in biosensing.* Journal of the American Chemical Society, 1998. **120**(46): p. 12108-12116.

69. Ryu, C.S., S.M. Cho, and B.W. Kim, *Interferometeric sensing of beta-galactosidase released by recombinant E-coli responding to an endocrine disruptor, tributyltin.* Biotechnology Letters, 2001. **23**(9): p. 653-659.

70. Park, J.S., S.H. Lim, S.J. Sim, H. Chae, H.C. Yoon, S.S. Yang, and B.W. Kim, *Enhancement of sensitivity in interferometric biosensing by using a new biolinker and prebinding antibody.* Journal of Microbiology and Biotechnology, 2006. **16**(12): p. 1968-1976.

71. Lim, S.H. and B.W. Kim, *Application of an interferometric biosensor chip to biomonitoring an endocrine disruptor.* Biotechnology and Bioprocess Engineering, 2004. **9**(2): p. 118-126.

72. Lin, H.H., T. Gao, J. Fantini, and M.J. Sailor, *A porous silicon-palladium composite film for optical interferometric sensing of hydrogen.* Langmuir, 2004. **20**(12): p. 5104-5108.

73. Gao, J., T. Gao, Y.Y. Li, and M.J. Sailor, *Vapor sensors based on optical interferometry from oxidized microporous silicon films.* Langmuir, 2002. **18**(6): p. 2229-2233.

74. Gao, J., T. Gao, and M.J. Sailor, *Porous-silicon vapor sensor based on laser interferometry.* Applied Physics Letters, 2000. **77**(6): p. 901-903.

75. Sohn, H., S. Letant, M.J. Sailor, and W.C. Trogler, *Detection of fluorophosphonate chemical warfare agents by catalytic hydrolysis with a porous silicon interferometer.* Journal of the American Chemical Society, 2000. **122**(22): p. 5399-5400.

76. Lee, B.J., S.G. Kim, and H. Sohn, *Optically encoded smart dust from DBR porous silicon.* Advanced Nondestructive Evaluation I, Pts 1 and 2, Proceedings, 2006. **321-323**: p. 53-56.

77. Kim, S.G., S. Kim, Y.C. Ko, S. Cho, and H. Sohn, *DBR-structured smart particles for sensing applications.* Colloids and Surfaces a-Physicochemical and Engineering Aspects, 2008. **313**: p. 398-401.

78. Kilian, K.A., T. Bocking, L.M.H. Lai, S. Ilyas, K. Gaus, M. Gal, and J.J. Gooding, *Organic modification of mesoporous silicon rugate filters: the influence of nanoarchitecture on optical behaviour.* International Journal of Nanotechnology, 2008. **5**(2-3): p. 170-178.

79. Koh, Y., S.J. Kim, J. Park, C. Park, S. Cho, H.G. Woo, Y.C. Ko, and H. Sohn, *Detection of avidin based on rugate-structured porous silicon interferometer.* Bulletin of the Korean Chemical Society, 2007. **28**(11): p. 2083-2088.

80. Kilian, K.A., T. Boecking, K. Gaus, M. Gal, and J.J. Gooding, *Peptide-modified optical filters for detecting protease activity.* ACS Nano, 2007. **1**(4): p. 355-361.

81. Schmedake, T.A., F. Cunin, J.R. Link, and M.J. Sailor, *Standoff detection of chemicals using porous silicon "smart dust" particles.* Advanced Materials, 2002. **14**(18): p. 1270-1272.

82. Link, J.R. and M.J. Sailor, *Smart dust: Self-assembling, self-orienting photonic crystals of porous Si.* Proceedings of the National Academy of Sciences of the United States of America, 2003. **100**(19): p. 10607-10610.

83. Huanca, D.R., F.J. Ramirez-Fernandez, and W.J. Salcedo, *Porous silicon optical cavity structure applied to high sensitivity organic solvent sensor.* Microelectronics Journal, 2008. **39**(3-4): p. 499-506.

84. Levitsky, I.A., W.B. Euler, N. Tokranova, and A. Rose, *Fluorescent polymer-porous silicon microcavity devices for explosive detection.* Applied Physics Letters, 2007. **90**(4): p. 041904-1-3.

85. Oton, C.J., L. Pancheri, Z. Gaburro, L. Pavesi, C. Baratto, G. Faglia, and G. Sberveglieri, *Multiparametric porous silicon gas sensors with improved quality and sensitivity.* Physica Status Solidi a-Applied Research, 2003. **197**(2): p. 523-527.

86. Chan, S., Y. Li, L.J. Rothberg, B.L. Miller, and P.M. Fauchet, *Nanoscale silicon microcavities for biosensing.* Materials Science & Engineering C-Biomimetic and Supramolecular Systems, 2001. **15**(1-2): p. 277-282.

87. DeLouise, L.A. and B.L. Miller, *Optimization of Mesoporous Silicon Microcavities for Proteomic Sensing.* Materials Research Society Symposium Proceedings, 2004. **782**: A5.3.1-A5.3.7.

88. DeLouise, L.A., P.M. Kou, and B.L. Miller, *Cross-correlation of optical microcavity biosensor response with immobilized enzyme activity. Insights into biosensor sensitivity.* Analytical Chemistry, 2005. **77**(10): p. 3222-3230.

89. Furbert, P., C.Y. Lu, N. Winograd, and L. DeLouise, *Label-free optical detection of peptide synthesis on a porous silicon scaffold/Sensor.* Langmuir, 2008. **24**(6): p. 2908-2915.

90. Rocchia, M., A.M. Rossi, and G. Zeppa, *Determination of ethanol content in wine through a porous silicon oxide microcavity.* Sensors and Actuators B-Chemical, 2007. **123**(1): p. 89-93.

91. Anderson, M.A., A. Tinsley-Bown, P. Allcock, E.A. Perkins, P. Snow, M. Hollings, R.G. Smith, C. Reeves, D.J. Squirrell, S. Nicklin, and T.I. Cox, *Sensitivity of the optical properties of porous silicon layers to the refractive index of liquid in the pores.* Physica Status Solidi a-Applied Research, 2003. **197**(2): p. 528-533.

92. Saarinen, J.J., S.M. Weiss, P.M. Fauchet, and J.E. Sipe, *Optical sensor based on resonant porous silicon structures.* Optics Express, 2005. **13**(10): p. 3754-3764.

93. Rong, G., A. Najmaie, J.E. Sipe, and S.M. Weiss, *Nanoscale porous silicon waveguide for label-free DNA sensing.* Biosensors & Bioelectronics, 2008. **23**(10): p. 1572-1576.

94. Arrand, H.F., T.M. Benson, A. Loni, R. Arens-Fischer, M. Kruger, M. Thonissen, H. Luth, and S. Kershaw, *Novel liquid sensor based on porous silicon optical waveguides.* IEEE Photonics Technology Letters, 1998. **10**(10): p. 1467-1469.

95. Boyd, J.T. and D.B. Anderson, *Radiation-Pattern of an End-Fire Optical-Waveguide Coupler.* Optics Communications, 1975. **13**(3): p. 353-358.

96. Palik, E., *Handbook of Optical Constants of Solids*. Handbook of Optical Constants of Solids, ed. E. Palik. 1998, College Park, Maryland: Academic Press.

97. S. Billat, M.T., R. Arens-Fischer, M. G. Berger, M. Krüger, H. Lüth, *Influence of etch stops on the microstructure of porous silicon layers.* Thin Solid Films, 1997. **297**(1-2): p. 22-25.

98. Yeh, P., *Optical waves in layered media*. 1988, New York: Wiley.

99. Steel, A.B., R.L. Levicky, T.M. Herne, and M.J. Tarlov, *Immobilization of nucleic acids at solid surfaces: Effect of oligonucleotide length on layer assembly.* Biophysical Journal, 2000. **79**(2): p. 975-981.

100. Hagan, M.F., A. Majumdar, and A.K. Chakraborty, *Nanomechanical forces generated by surface grafted DNA.* Journal of Physical Chemistry B, 2002. **106**(39): p. 10163-10173.

101. Lukosz, W., *Principles and Sensitivities of Integrated Optical and Surface-Plasmon Sensors for Direct Affinity Sensing and Immunosensing.* Biosensors & Bioelectronics, 1991. **6**(3): p. 215-225.

102. Donald Voet, J.G.V., *Biochemistry*. 2nd ed. 2004, New York: John Wiley & Sons.

103. Steinem, C., A. Janshoff, V.S.Y. Lin, N.H. Volcker, and M.R. Ghadiri, *DNA hybridization-enhanced porous silicon corrosion: mechanistic investigators and prospect for optical interferometric biosensing.* Tetrahedron, 2004. **60**(49): p. 11259-11267.

104. Hermanson, G., *Bioconjugate Techniques*. 1996, New York: Academic Press.

105. Amato, G., L. Boarino, S. Borini, and A.M. Rossi, *Hybrid approach to porous silicon integrated waveguides.* Physica Status Solidi a-Applied Research, 2000. **182**(1): p. 425-430.

106. Samoc, A., A. Miniewicz, M. Samoc, and J.G. Grote, *Refractive-index anisotropy and optical dispersion in films of deoxyribonucleic acid.* Journal of Applied Polymer Science, 2007. **105**(1): p. 236-245.

107. Rekesh, D., Y. Lyubchenko, L.S. Shlyakhtenko, and S.M. Lindsay, *Scanning tunneling microscopy of mercapto-hexyl-oligonucleotides attached to gold.* Biophysical Journal, 1996. **71**(2): p. 1079-1086.

108. Solanki, C.S., R.R. Bilyalov, J. Poortmans, J.P. Celis, J. Nijs, and R. Mertens, *Self-standing porous silicon films by one-step anodizing.* Journal of the Electrochemical Society, 2004. **151**(5): p. C307-C314.

109. Di Francia, G., M. Della Noce, V. La Ferrara, L. Lancellotti, P. Morvillo, and L. Quercia, *Nanostructured porous silicon for gas sensor applications.* Materials Science and Technology, 2002. **18**(7): p. 767-771.

110. Garel, O., C. Breluzeau, E. Dufour-Gergam, A. Bosseboeuf, B. Belier, V. Mathet, and F. Verjus, *Fabrication of free-standing porous silicon microstructures.* Journal of Micromechanics and Microengineering, 2007. **17**(7): p. S164-S167.

111. Solanki, C.S., R.R. Bilyalov, J. Poortmans, G. Beaucarne, K. Van Nieuwenhuysen, J. Nijs, and R. Mertens, *Characterization of free-standing thin crystalline films on porous silicon for solar cells.* Thin Solid Films, 2004. **451-52**: p. 649-654.

112. Ghulinyan, M., C.J. Oton, G. Bonetti, Z. Gaburro, and L. Pavesi, *Free-standing porous silicon single and multiple optical cavities.* Journal of Applied Physics, 2003. **93**(12): p. 9724-9729.

113. Tjerkstra, R.W., J.G.E. Gardeniers, J.J. Kelly, and A. van den Berg, *Multi-walled microchannels: Free-standing porous silicon membranes for use in mu TAS.* Journal of Microelectromechanical Systems, 2000. **9**(4): p. 495-501.

114. Ulrich, R. and R. Torge, *Measurement of Thin-Film Parameters with a Prism Coupler.* Applied Optics, 1973. **12**(12): p. 2901-2908.

115. Vinu, A., M. Miyahara, and K. Ariga, *Assemblies of biomaterials in mesoporous media.* Journal of Nanoscience and Nanotechnology, 2006. **6**(6): p. 1510-1532.

116. Tinland, B., A. Pluen, J. Sturm, and G. Weill, *Persistence length of single-stranded DNA.* Macromolecules, 1997. **30**(19): p. 5763-5765.

117. Tresset, G. and S. Takeuchi, *Utilization of cell-sized lipid containers for nanostructure and macromolecule handling in microfabricated devices.* Analytical Chemistry, 2005. **77**(9): p. 2795-2801.

118. Liscidini, M., D. Gerace, L.C. Andreani, and J.E. Sipe, *Scattering-matrix analysis of periodically patterned multilayers with asymmetric unit cells and birefringent media.* Physical Review B, 2008. **77**(3): p. 035324-1-11.

119. Anderson, P.A., B.S. Schmidt, and M. Lipson, *High confinement in silicon slot waveguides with sharp bends.* Optics Express, 2006. **14**(20): p. 9197-9202.

120. Barrios, C.A., M.J. Banuls, V. Gonzalez-Pedro, K.B. Gylfason, B. Sanchez, A. Griol, A. Maquieira, H. Sohlstrom, M. Holgado, and R. Casquel, *Label-free optical biosensing with slot-waveguides.* Optics Letters, 2008. **33**(7): p. 708-710.

121. Hitz, B., *Slot waveguide is a sensitive biochemical sensor.* Photonics Spectra, 2007. **41**(12): p. 24-26.

122. Barrios, C.A., K.B. Gylfason, B. Sanchez, A. Griol, H. Sohlstrom, M. Holgado, and R. Casquel, *Slot-waveguide biochemical sensor.* Optics Letters, 2007. **32**(21): p. 3080-3082.

123. Vivien, L., X. Le Roux, S. Laval, E. Cassan, and D. Marris-Morini, *Design, realization, and characterization of 3-D taper for fiber/micro-waveguide coupling.* Ieee Journal of Selected Topics in Quantum Electronics, 2006. **12**(6): p. 1354-1358.

124. Kilian, K.A., T. Bocking, K. Gaus, J. King-Lacroix, M. Gal, and J.J. Gooding, *Hybrid lipid bilayers in nanostructured silicon: a biomimetic mesoporous scaffold for optical detection of cholera toxin.* Chemical Communications, 2007(19): p. 1936-1938.

125. Meskini, O., A. Abdelghani, A. Tlili, R. Mgaieth, N. Jaffrezic-Renault, and C. Martelet, *Porous silicon as functionalized material for immunosensor application.* Talanta, 2007. **71**(3): p. 1430-1433.

126. Borini, S., A.M. Rossi, L. Boarino, and G. Amato, *Patterning of porous silicon by electron-beam lithography.* Journal of the Electrochemical Society, 2003. **150**(5): p. G311-G313.

127. Park, H., J.H. Dickerson, and S.M. Weiss, *Spatially localized one-dimensional porous silicon photonic crystals.* Applied Physics Letters, 2008. **92**(1): p. 011113-1-3.

128. Lin, J.C., H.T. Hou, and W.C. Tsai, *A mask-free method of patterned porous silicon formation by a localized electrical field.* Microelectronic Engineering, 2007. **84**(2): p. 336-339.

129. Kapaklis, V., A. Georgiopoulos, P. Poulopoulos, and C. Politis, *Patterning of porous silicon by metal-assisted chemical etching under open circuit potential conditions.* Physica E-Low-Dimensional Systems & Nanostructures, 2007. **38**(1-2): p. 44-49.

130. Gargas, D.J., O. Muresan, D.J. Sirbuly, and S.K. Buratto, *Micropatterned porous-silicon Bragg mirrors by dry-removal soft lithography.* Advanced Materials, 2006. **18**(23): p. 3164-3168.

131. Sirbuly, D.J., G.M. Lowman, B. Scott, G.D. Stucky, and S.K. Buratto, *Patterned microstructures of porous silicon by dry-removal soft lithography.* Advanced Materials, 2003. **15**(2): p. 149-152.